Summer 7-29-2021

Finite Element Modelling and Exergy Analysis of a Solar Thermal Hollow Fiber Vacuum Membrane Distillation System

Benjamin Shuldes
University of Nebraska-Lincoln, benjamin.shuldes@huskers.unl.edu

FINITE ELEMENT MODELLING AND EXERGY ANALYSIS OF A SOLAR THERMAL HOLLOW FIBER VACUUM MEMBRANE DISTILLATION SYSTEM

By

Benjamin N. Shuldes

A THESIS

Presented to the Faculty of

The Graduate College at the University of Nebraska

In Partial Fulfillment of the Requirements

For the Degree of Master of Science

Major: Chemical Engineering

Under the Supervision of Professor Siamak Nejati

Lincoln, Nebraska

July, 2021

FINITE ELEMENT MODELLING AND EXERGY ANALYSIS OF A SOLAR THERMAL HOLLOW FIBER VACUUM MEMBRANE DISTILLATION SYSTEM

Benjamin N. Shuldes, M.S.

University of Nebraska, 2021

Advisor: Siamak Nejati

A finite element model was developed to investigate the performance of a vacuum membrane distillation module under various operating conditions and membrane parameters. Porosity, tortuosity, pore diameter, membrane thickness, and fiber length were varied along with feed temperature, velocity, and flow configuration. In all cases, boundary layer polarization phenomena were seen to inhibit the performance of the module. At certain conditions, for a 7.5 cm fiber, the reduction in permeate flux from 65 LMH (Liter/m^2/h) at the inlet to below 45 LMH at the outlet of the fibers was observed. In most cases, salt concentration polarization was the rate determining phenomenon. The increase in salt concentration from a mass fraction of 0.035 to the saturation value within the boundary layer, led to 12.5% reduction in the driving force of separation. After salt concentration reached saturation within the boundary layer, heat loss continued to reduce the driving force for separation. Changing the feed from the shell to the lumen side of the membrane was seen to result in a significant decrease in permeate flux. Adding a baffling scheme to the surface of a shell side feed was seen to suppress concentration polarization and enhance membrane performance as did an increase in the feed velocities. Exergy efficiency tended to increase with feed temperature but decreased with an increase in average permeate flux. All changes in membrane parameters and design considerations had a minimal effect on overall exergy efficiency. Individual unit operations balances

revealed the solar collector to provide more than 80% of all the exergy losses of the process units. It was found that the exergy loss of the solar collector was significantly dependent on process design. These findings revealed the need for continued optimization of various process designs to improve the exergy efficiency of the processes and improve the usefulness of vacuum membrane distillation for use in a solar desalination scheme.

“Resolved, never to suffer the least motions of anger to irrational beings.”

-Jonathan Edwards

SDG

Table of Contents

Table of Figures

CHAPTER 1

INTRODUCTION AND CONTEXT

1.1. Context

One of the most urgent needs of our rapidly globalizing society is the provision of clean, drinkable water. In many areas of the planet, people do not readily have access to potable water or are restricted by their geography from obtaining it. As populations rise an increased stress is placed on water scarce locations. [1,2] One such location is the city-state of Singapore.[3] Since the island nation separated from the newly independent Malaysia in 1965 it has been largely dependent on the neighboring peninsula to fulfill its demand for clean water.[3–5] A desire for national self-sufficiency has motivated the country to remove this dependency by investing significantly in desalination technology.[3–6] While the city has few natural freshwater resources, the tip of the Malay peninsula is not lacking in a supply of seawater. Despite investment and the availability of resources, desalinated water still only accounts for 10% of Singapore's fresh water use, though the government envisions expanding this share to 30% over the next four decades.[7]

A problem exists for Singapore as it seeks to meet this goal. Desalination is an energy intensive process. It is far more costly than other methods, such as wastewater reclamation and rainwater collection, which are also available to the city.[5,6,8] Increasing the contribution of seawater desalination to wean the country off its neighbor's supply requires a similar investment in energy infrastructure.[5] Providing energy from outside sources, such as importing power from Malaysia, or fuels to operate power plants

on the island, is defeatist to Singapore's goals. The only natural solution comes from domestic renewable energy.[9] The famously smog conscious city lies very near the equator where solar energy is most effective and consistently available. A solar powered desalination scheme could provide for the city's drinking needs while not contributing to air pollution like most modes of power generation. Singapore has then a multiplicity of reasons to pursue renewable energy sources for desalination.

Thus far for Singapore, its location and climate allow rainwater to provide for the majority of its drinking water needs.[6] Because of this, the motivation to invest in desalination does not yet reach the level of a national imperative, but this is not the case for every nation. Many countries on the Persian Gulf have also invested heavily in desalination technology.[10–12] Unlike Singapore, the climate of these nations does not provide a broad range of options for its water sources.[11,13] Neither are their neighbors able, in many cases, to augment domestic production as Malaysia has done for Singapore. For many of these countries, desalination is a necessity, and the same problem remains of how one may provide energy for it. The Persian Gulf is one of the great energy hubs of the world and this makes the need for renewable energy less of a sovereignty issue, however, environmental concerns are still significant.

Rural communities also provide unique challenges for water treatment. Many such communities cannot practically provide the infrastructure of large cities. Many of these have water readily available that only needs to be cleaned, be it saline, brackish, or contaminated in some other way.[2,14] For these areas renewable energy is the only viable option and passive systems that do not rely on extensive electrical and mechanical components are extremely attractive.[2,14,15]

In the world as a whole, the provision of clean water and renewable energy is a growing need. The United Nations estimates that 1.2 billion people throughout the world live in areas where potable water is scarce.[2] A further 1.6 billion do not have access to water because of the technical difficulty of treating it.[2] The treatment of water is a global challenge that affects more than one third of the world's population. Seawater is an abundant resource that, once purified, can easily meet these needs. Despite this the technology used to perform this purification requires improvement in order to make it more practical and to alleviate global water stress.

1.2. Solar Desalination

Desalination then rests at a nexus between two key issues faced by modern society, the provision of resources necessary for its existence and the growing concern of its environmental impact. In recognition of this dynamic, solar methods of desalination have been and are being devised. [9,16–20] These all range in scale and complexity and have their advantages and disadvantages. It is the task of the engineer to analyze these tradeoffs and to improve the technology wherever possible. There are, broadly speaking, two categories of solar desalination schemes. The first is photovoltaic powered reverse osmosis plants (PV-RO) and the second is solar thermal desalination.[9,16–18,20]

1.2.1 PV-RO

Reverse osmosis has revealed itself as the state of the art of desalination technologies.[21–23] In terms of energy cost for a desired water production it is

matchless in its performance.[20–22] The reason for RO's dominance is the nature of the separation. Nearly every other method of desalination relies on some sort of phase change to achieve separation. The thermodynamics of this phase change is the root cause of much of the cost of these technologies.[20–22] The latent heat of vaporization of water is relatively high (about 667 kWh/m^3) and providing the power necessary to vaporize water for an entire city is difficult. RO overcomes this challenge by removing the phase change from the discussion. In RO, a pressure is applied to overcome the osmotic pressure across a semipermeable membrane (work of separation about 1.06 kWh/m^3 for 50% recovery). [20,21] In this way, the natural flow of water as driven by chemical potential is reversed and there is a net generation of fresh water.

The pressure-driven nature of reverse osmosis makes it dependent on electricity.[14,16–18,20,21] The best and most reliable means of providing the needed operating pressure are electrically driven. On this basis, a solar desalination scheme based on reverse osmosis requires the use of photovoltaic (PV) cells. [14,16–18,20] Recent advances in battery technology and solar energy conversion have made PV-RO more practicable in the real world, however, many problems still exist that limit its implementation. [24,25] PV cells are limited in their efficiency, even the best PV cells can only achieve 30% conversion of incident solar radiation to electrical energy. [20,24] Many PV cells can also be expensive to make and utilize rare or scarce materials. [26] These make PV cells problematic from an environmental standpoint in the mining and production of the materials necessary, as well as from an operational standpoint in maintenance and replacement of these cells.

Reverse osmosis is also limited by the achievable water recovery using current membrane technology. As freshwater is produced the concentration of salt in the feed is increased as is the osmotic pressure that must be overcome to achieve separation. Current RO designs are unable to hold up to the supply pressure required by a feed with a mass fraction of salt much higher than 0.08. [21,27,28] This results in a large amount of effluent brine from a reverse osmosis plant and the environmental concerns that come with it. [11,13,15]

Despite the problems of PV-RO on these bases the three order of magnitude difference in the work of separation in RO compared to the work of vaporization in thermal methods provides a significant gap in efficiency of PV-RO and thermal methods of desalination. [16–18,20–22] As photovoltaics continue to improve, this gap in efficiency will only become more apparent.

1.2.2 Solar Thermal Desalination

In contrast to the single-phase reverse osmosis, thermal methods of desalination operate by making use of a phase change. Solar thermal desalination relies on solar energy to heat the saline feed and produce water vapor. That water vapor, when condensed, is the product fresh water. Many ways have been devised to perform this type of separation but nearly all can be described as a variation on a very old piece of technology.

1.2.2.1 The Solar Still

The simplest form of solar thermal desalination is the solar still (shown in figure 1-1).[18] A solar still is simply a box containing water.[16–18,20,29] Sunlight enters the box and heats the water to produce water vapor.[16–18,20,29] That vapor is condensed on the walls and roof of the box and directed away from the feed to be collected as drinking water. [16–18,29,30] Their extremely simple and cheap design makes solar stills very attractive for poor and rural locations that either cannot afford the cost of building and maintaining a PV-RO system or are prohibited from implementing PV-RO by a lack of infrastructure. [14,15,18] Solar stills can be purchased for survival situations and have saved the lives of sailors stranded at sea. [31] The limited recovery of solar stills makes them impractical for more urbanized contexts and locations that require significant water production. [16–18] A cost effective and passive method, such as the solar still, for larger scale water production is still very attractive for contexts with higher demand.

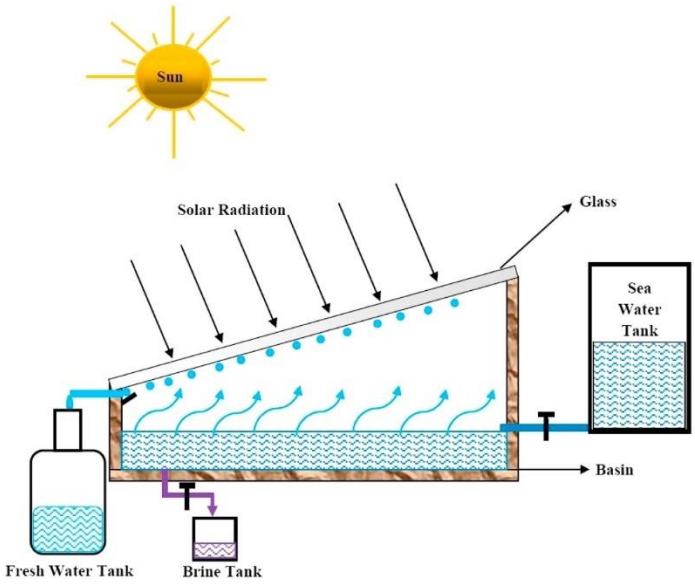

Figure 1-1: A simple schematic of a solar still.[18]

1.2.2.2 Solar Thermal Membrane Distillation

Into this point of the issue enters membrane distillation. Membrane distillation is a thermal method of desalination very similar in practice a solar still. Figure 1-2 provides a visual of the physics behind MD. At the core of the process is a hydrophobic, air filled, membrane. In the most basic MD schemes two streams of water are placed on either side of this membrane, one comprised of saline water, one of fresh water. Unlike reverse osmosis, separation is not achieved by the application of hydraulic pressure. Rather, in MD, separation occurs as a result of a difference in vapor pressure at either side of the membrane.[16,18,32–35] The higher temperature of the feed (saline) side of the membrane results in a higher concentration of water vapor within the membrane and causes the spontaneous diffusion of vapor to the cold freshwater side. This vapor is condensed in the cooler freshwater stream which leads to a net production of fresh water.[16,18,32–35]

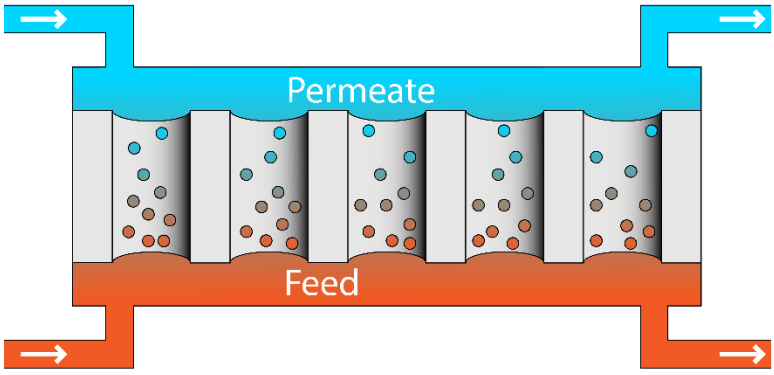

Figure 1-2: Membrane distillation schematic.

Different configurations exist for membrane distillation each with tradeoffs that make them more practical in different contexts. [16,18,32–35] The scheme described above is called direct contact membrane distillation. [16,18,32–36] Sweeping gas

membrane distillation replaces the freshwater stream with a sweeping gas and an external condenser. [18,32–36] Air gap membrane distillation replaces this sweeping gas with a stagnant, gas filled, region against which a condensing surface is placed opposite the membrane. [18,32–35] Vacuum membrane distillation (VMD) is of especial interest and serves as the focus of this work. Figure 1-3 shows the operating principle of VMD. Vacuum membrane distillation replaces the freshwater stream with a vacuum. [18,32–37] This replacement significantly lowers the mass transfer resistance of the membrane by removing air which is the predominant inhibitor to Fickian diffusion. [32] In fact, the pressure can be reduced to the point that chemical potential no longer provides the driving force for separation. [32] A vacuum of sufficiently low pressure can instead see pressure driven flow occur wherein the higher pressure of the feed-generated vapor flows to the low pressure of the vacuum.

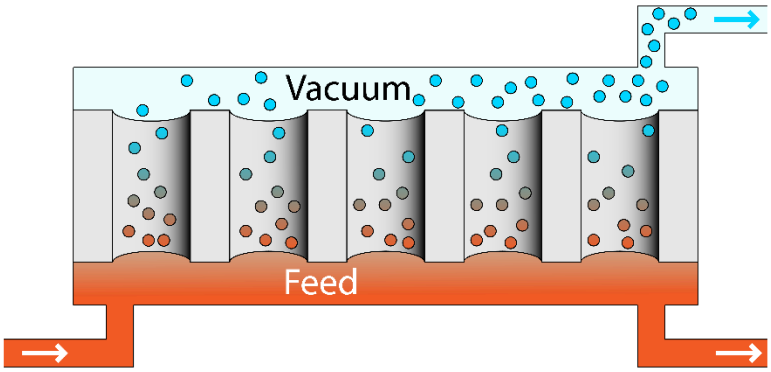

Figure 1-3: Vacuum membrane distillation schematic.

One of the benefits of membrane distillation is the ability to heat the seawater directly by use of a solar collector. [16–18] In contrast to PV cells, solar collectors have been devised that can achieve near perfect conversion of solar radiation to heat.[20,38] These materials also require very little maintenance. Passive solar stills based on

membrane distillation have been designed and shown to achieve reasonable freshwater generation. [39–41] The modular nature of membrane distillation, low hydraulic pressure requirement, and the ability to use surface heating by way of these novel solar collectors means that more active MD designs which can achieve higher water production can also be readily applied to rural and impoverished areas that cannot accommodate PV-RO. VMD is also able to achieve zero liquid discharge which improves its ecological friendliness.[42,43]

This all allows membrane distillation to retain the benefits of a solar still while achieving the high production rate of reverse osmosis. Like a solar still, MD can be run either passively or actively. MD requires far less maintenance than a PV-RO process while still achieving high water production. Unfortunately, MD retains the energetic difficulties brought on by the phase change required at the feed side. [21] This phase change makes it unlikely that MD will ever be more energetically efficient than PV-RO. [21] The nature of MD operation can make it more economically viable, especially if the energetics of the process are well understood. To that end numeric models were developed to investigate the physical performance of a solar thermal VMD system and the thermodynamic inefficiencies inherent to it.

CHAPTER 2

FINITE ELEMENT MODELLING

2.1. Modelling Background

The modelling of vacuum membrane distillation has undergone an evolution over the last thirty years which has gained particular speed over the last twenty. In the early stages of VMD modelling the main concern was in discerning the transport phenomena occurring within the membrane.[32,44–46] Questions existed about the relative effects of Knudsen transport, free diffusion, and viscous flow within the porous media. This concern of the earlier computationalists is understandable. A model that cannot accurately describe the physics of the process is of little use to improving the system.

Once the theory was settled models were developed to investigate the broader performance of VMD and the transport occurring within membrane modules. This development came along with a transition in methods to computational fluid dynamics (CFD) which has dominated VMD modelling over the last ten years.[47] Early CFD models focused on two-dimensional flat sheet or axisymmetric membrane modules.[48,49] These eventually developed to three dimensional models primarily focused on hollow fiber modules.[47,50–52] Most of these focused on heat and momentum transport within the module with a few considering the contribution of concentration in detail. These models were found generally to be very useful for model guided design and have paid off in the development of experimental membrane technologies.

More recently modelling has transitioned to focus on tackling the main issues that remain for VMD. Some have focused on novel module designs and the integration of

modules with other parts of the VMD process.[53,54] Mechanistic studies of membrane wetting and fouling have been performed.[55,56] Others have sought to investigate the affects of anti-fouling coatings on heat and mass transfer within the system.[57,58] More recently applications of artificial neural networks to these problems have been developed.[59]

This work seeks to carry on with the CFD modelling work and apply it to a simple multi-level modelling scheme. It seeks to close some of the gap in consideration of mass transport phenomena within the feed and the effects of these phenomena on a broader process. Multi-level modelling is an important step to take in advancing the VMD process from the laboratory scale to the real world. Thus a CFD model based on finite element analysis was developed.

2.2. Geometry

Finite element analysis is a powerful tool to investigate the performance of designed modules. A geometry may be defined in the finite element modelling package and then the physics defined with relevant differential equations and appropriate boundary conditions. The membrane module herein described was defined and solved using COMSOL Multiphysics®. The geometry of this problem is a hollow fiber membrane module. Figure 2-1 outlines the basic scheme of this geometry. Each hollow fiber is a long hollow cylinder of uniform radius and thickness. Hollow fibers are placed in a “close-packed” formation so as to achieve the maximum density of regularly spaced fibers. The close-packed configuration generates three planes of symmetry which can be used to reduce the overall computational domain to a single unit cell that is descriptive of the whole (highlighted in figure 2-1).[60]

The close packed configuration can be described as a repeated translation and reflection of three fibers with their centers placed at the vertices of an equilateral triangle (fibers labeled 1,2, and 3 in figure 2-1). A line may be drawn that bisects fibers 1 and 2. One can see that in the bulk packing this line forms a line of symmetry for this two-dimensional geometry. A second line may be drawn that connects the center point of fiber 1 with the midpoint between fibers 2 and 3. Finally a third line may be drawn that connects the center point of fiber 3 to the midpoint of fibers 1 and 2.

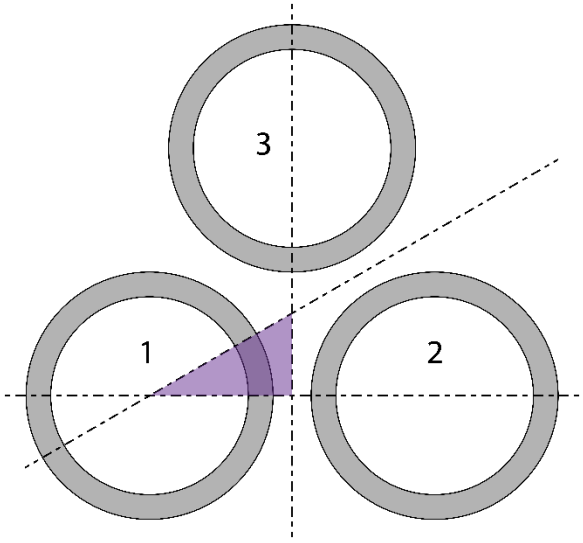

Figure 2-1: Membrane module packing configuration, planes of symmetry, and modelling domain.

Extension of these lines in the axial direction of the fibers generates three planes of symmetry.[60] These planes of symmetry allow the geometry to be reduced to a unit shell.[60] Each unit cell corresponds to $1/12^{th}$ of a full fiber and the portions of the geometry closest to it. Average and spatially dependent behaviors for the membrane and module (e.g. average permeate flux, and concentration and temperature profiles) are the

same for this unit cell. Integrated behaviors for the membrane and module (e.g. total water production) are respectively 12 and $12n$ times the same integred behavior for the unit cell (for n fibers in the module).

Figure 2-2 outlines the definitions that complete the geometry of the unit cell. δ_m is the thickness of the fiber, R_i is the inner radius of the hollowfiber (the radius of the lumen), R_o is the outer radius of the hollowfiber where $R_o = R_i + \delta_m$, and a is the fiber spacing parameter defined by R_o/a = 0.35 (this ratio can be any number between 0 and 0.5).[60] a is the distance between the centerlines of two adjacent fibers.

With the geometry of the unit cell defined, the unit cell itself may be divided into three domains: a lumen, a membrane, and a shell domain depending on the radius "r" from centerline of the membrane (outlined in figure 2-2). The lumen is the "inside" of the hollow fiber defined by the region $r < R_i$. The membrane is the "wall" or the material that comprises the hollow fiber defined by $R_i < r < R_o$. The shell is the portion of the geometry outside the hollow fiber defined by $R_o < r$.

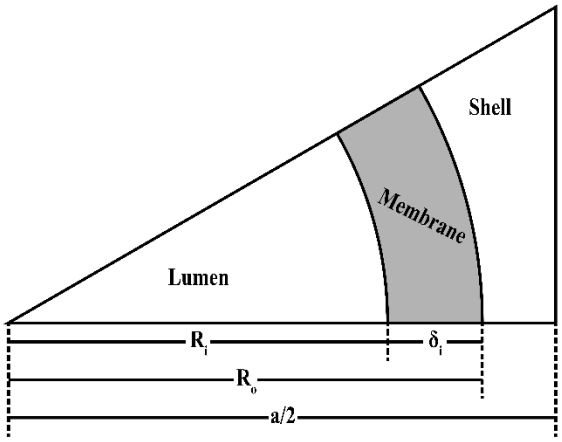

Figure 2-2: Geometric definitions for the hollow fiber module.

These three geometric domains can be grouped into two physical domains based on the phases of the fluids flowing within them. The first of these is the feed domain in which the flowing fluid is a liquid. This domain can be either the lumen or the shell depending on the desired configuration. The second of these physical domains is the permeate in which the fluid is a vapor. The hydrophobic nature of the membrane requires that it always be included in this domain. The vapor also flows outside the membrane in whichever of the lumen or shell domains does not receive the feed. Thus, either of these regions must also be included in the permeate.

Because the lumen and shell can both contain either the feed or a portion of the permeate domain it is useful at this point to change the nomenclature of the problem to describe the fluid rather than the geometry. The portion of the geometry, shell or lumen, that contains the liquid feed domain is called the “feed”. The term “membrane” is retained for the membrane portion of the geometry. The remaining portion of the permeate domain can be called the “vacuum” and, like the feed, can be either the lumen or the shell.

The geometry can be simplified further by making use of several assumptions. Momentum transfer within the vacuum domain may be neglected because the majority of the pressure drop within the permeate domain occurs within the membrane.[51] A continuum of flow is present within the permeate and as such the portion of the permeate that contributes most significantly to pressure drop will be most descriptive of that continuum of flow. For vacuum membrane distillation heat transfer from the membrane to the vacuum will be negligible, especially if the module is considered to be well insulated. Conductive heat transfer through the membrane can then be neglected. [61,62]

If the vacuum pressure is less than the saturation pressure of water for the whole length of fiber then the mass fraction of water in the permeate at the membrane boundary is unity and in time all air that might initially be present in the permeate domain is displaced by the steady flow of water vapor. Mass transfer within the permeate domain can then be neglected (this assumption also requires that there be no volatile components within the feed). The result of these assumptions is that the vacuum domain may be neglected and the permeate domain restricted to the membrane for modelling purposes.

The only remaining transport phenomenon that requires consideration within the permeate is momentum transfer. Momentum transfer can be effectively defined based on Darcy's law.[63] Because we have assumed the majority of the pressure drop in the permeate occurs within the membrane, the pressure of the vacuum domain can be considered to be constant. Darcy's law is a function of the total pressure drop across the membrane.[63] If the pressure on the vacuum side of the membrane is constant, and below the saturation pressure of water at the membrane/feed interface, Darcy's law becomes only a function of pressure at the feed side of the membrane and can then be defined based on the saturation pressure at that interface. The geometry can then be refined further to consist of only the feed side of the membrane, and Darcy's law may be applied as a boundary condition along the feed/membrane interface.

These assumptions in the end allow the whole membrane module to be described by the physics present within the feed domain. The lumen and shell geometries are the only geometries that need to be defined in the model and the physics of the feed are the only physics that needs to be defined within them. The three transport phenomena present within the feed domain are momentum transfer, heat transfer, and mass transfer.

2.3. Momentum Transfer Governing Equations and Boundary Conditions

Momentum transfer of the feed was defined by the Navier-Stokes equations and the continuity equation:[64]

$$\rho\left(\vec{u}_f \cdot \nabla\vec{u}_f\right) = \nabla \cdot \left(-P_f \cdot \vec{\vec{I}} + \mu_f\left(\nabla\vec{u}_f + \left(\nabla\vec{u}_f\right)^T\right)\right) \quad (2\text{-}1)$$

$$\rho\nabla \cdot \vec{u}_f = 0 \quad (2\text{-}2)$$

Where ρ is the density of the fluid (kg/m^3), $\vec{u}_f$ is the velocity vector (m/s), P_f is the pressure of the feed fluid (Pa), μ_f is the dynamic viscosity of the feed fluid ($Pa\ s$), $\vec{\vec{I}}$ is the identity tensor ($dimensionless$). At the fiber inlet a normal velocity ($\vec{u}_{f,in}, m/s$) was provided as the boundary condition:

$$\vec{u}_f = \vec{u}_{f,in} \qquad @ \qquad z = 0\ m \quad (2\text{-}3)$$

A no-slip boundary condition was provided at the membrane/feed interface:

$$\vec{u}_f = \vec{0}\ m/s \qquad @ \qquad r = R_i \qquad \text{for Lumen Side Feed}$$

$$@ \qquad r = R_o \qquad \text{for Shell Side Feed} \quad (2\text{-}4)$$

An outlet pressure was defined at the outlet of the feed channel:

$$P = 1\ atm \qquad @ \qquad z = L_m \quad (2\text{-}5)$$

These complete the model necessary for momentum transfer within the feed which will come to define the boundary conditions at the membrane interface and the convective components of transport for the two remaining physics.

2.4. Darcy's Law and Permeate Definition

Removal of the permeate is the key phenomenon around which all remaining boundary conditions for the model will be based. It is then prudent to describe how Darcy's law will be defined before moving on to heat and mass transfer in the feed. Based on the above assumptions, permeate flux may be defined based on Darcy's law (equation 2-6). [63]

$$\vec{q} = -\frac{\kappa}{\mu}\nabla P \tag{2-6}$$

Where q is the volumetric flowrate of the fluid (m^3/s), κ is the permeability of the membrane (m^2), μ is the dynamic viscosity of the fluid ($Pa\ s$), and ΔP is the pressure drop across the membrane (Pa). Correlations are not readily available to describe the permeability of a membrane based solely on its parameters. It is then necessary to define equation 2-6 in another way that allows the resistance of the membrane to be described.

Zhang et al. (2016) defined the following equation for mass flux across a membrane (equation 2-7. See also Sharon and Reddy, 2015). [18,50,51]

$$N = C_t M_w \Delta P \tag{2-7}$$

Where N is the mass flux across the membrane ($kg/m^2 s$), and M_w is the molar mass of water (kg/mol). This definition has the benefit of being of the same form as Darcy's law, a flow rate (normalized to area) defined by characteristics of the membrane, the fluid, and the pressure drop, while replacing the problematic variable κ with the coefficient C_t ($s\ mol/kg\ m$). C_t is a lumped coefficient that is the sum of the Knudsen diffusion coefficient (C_1, $s\ mol/kg\ m$) and the Poiseuille diffusion coefficient (C_2, $s\ mol/kg\ m$).[50] Both of these coefficients may be determined using the membrane parameters (equations 2-8 to 2-10).[50]

$$C_t = C_1 + C_2 \tag{2-8}$$

$$C_1 = \frac{4d_p}{3\delta_m \tau}\left(\frac{1}{2\pi R M_w T_f}\right)^{1/2} \tag{2-9}$$

$$C_2 = \frac{d_p \epsilon P_m}{32\delta_m \tau \mu R T_f} \tag{2-10}$$

Where d_p is the pore diameter (m), δ_m is the thickness of the membrane (m), τ is the membrane tortuosity ($dimensionless$), R is the ideal gas constant (8.3145 $J/mol\ K$), T_f is the temperature (K), ϵ is the membrane porosity (void fraction, $dimensionless$). P_m is the mean pressure within the membrane (Pa) defined by equation 2-11:[50]

$$P_m = \frac{P_{vac} + P_{sat}}{2} \tag{2-11}$$

P_{vac} is the vacuum pressure (Pa) and P_{sat} is the saturation pressure of water (Pa) at temperature T_f defined by equation 2-12:[50,60]

$$P_{sat} = a_w \exp\left(23.238 - \frac{3841}{T_f - 45}\right) \tag{2-12}$$

One will recognize equation 2-12 as Antoine's equation multiplied by a corrective term that accounts for how dissolved salt reduces the saturation pressure. a_w, the activity coefficient of water ($dimensionless$), is defined based on the mole fraction of salt (x_s, $dimensionless$):[36,60]

$$a_w = 1 - 0.5x_s - 10x_s^2 \tag{2-13}$$

a_w is a polynomial fitting that is accurate up to the saturation concentration of salt in water (about 350 g/L).[65] At this concentration a_w takes on a constant value as salt spontaneously precipitates out of the solution. Finally, ΔP is defined simply as the difference between the saturation pressure and the vacuum pressure.[50]

$$\Delta P = P_{sat} - P_{vac} \tag{2-14}$$

The model from equations 2-7 through 2-14 thus provides the basis of all calculations relating to permeate flux. With this portion of the model defined one can move on to the remaining transport phenomena present in the feed.

2.5. Heat Transfer Governing Equations and Boundary Conditions

The governing equations for heat transfer were defined by the differential heat balance:[64]

$$\rho C_p \vec{u}_f \cdot \nabla T_f + \nabla \cdot \vec{q}_f = 0 \tag{2-15}$$

$$\vec{q}_f = -k_f \nabla T_f \tag{2-16}$$

Where C_p is the heat capacity of the fluid ($J/kg\ K$), $\vec{q}_f$ is the conductive heat flux (W/m^2), and k_f is the thermal conductivity of the feed ($W/m\ K$). A feed temperature ($T_{f,in}, K$) served as the boundary condition at the inlet to the fiber:

$$T_f = T_{f,in} \qquad @ \qquad z = 0\ m \tag{2-17}$$

Heat flux across the membrane/feed interface was defined based on equation (2-7)[60]:

$$q_m = -NH_{vap} - h_m(T_{f,in} - T_m)$$

$$@ \quad r = R_i \quad \text{for Lumen Side Feed}$$

$$@ \quad r = R_o \quad \text{for Shell Side Feed} \tag{2-18}$$

Where q_m is the heat flux across the boundary (W/m^2), H_{vap} is the heat of vaporization of water (J/kg), h_m is the convective heat transfer coefficient (W/m^2K),

and T_m is the temperature at the boundary (K). The convective term in equation 18 was seen to be essentially zero and was neglected.[61,62]

2.6. Mass Transfer Governing Equations and Boundary Conditions

A model for the binary mass transport was defined based on a differential mass balance:[66]

$$\nabla \cdot \vec{j}_i + \rho(\vec{u}_f \cdot \nabla)\omega_i = 0 \tag{2-19}$$

Where $\vec{j}_i$ is the diffusive flux of component "i" (kg/m^2s), and ω_i is the mass fraction of component "i" in the fluid ($dimensionless$).[66]

$$\vec{N}_i = \vec{j}_i + \rho\vec{u}_p\omega_i \tag{2-20}$$

Where $\vec{N}_i$ is the total flux of component "i" (kg/m^2s).[66]

$$\vec{j}_i = -\left(\rho D_i^m \nabla\omega_i + \rho\omega_i D_i^m \frac{\nabla M_n}{M_n} - \vec{j}_{ci}\right) \tag{2-21}$$

Where D_i^m is the mixture averaged diffusion coefficient (m^2/s) defined by equation 2-22: [66]

$$D_i^m = \frac{(1-\omega_i)D_{ik}}{x_k} \tag{2-22}$$

Where D_{ik} is the binary diffusion coefficient for species "i" in species "k" (m^2/s) and x_k is the mole fraction of species k ($dimensionless$). M_n is the mean molar mass of the mixture (kg/mol) defined by equation 2-23:[66]

$$M_n = \left(\frac{\omega_i}{M_i} + \frac{\omega_k}{M_k}\right)^{-1} \tag{2-23}$$

Were M_i is the molar mass of species "i" (kg/mol). $\vec{j}_{ci}$ is the mixture diffusion correction term (kg/m^2s) defined by equation 2-24:[66]

$$\vec{J}_{ci} = \rho\omega_i \left(\frac{M_i}{M_n} D_k^{\mathrm{m}} \nabla x_k\right) \quad (2\text{-}24)$$

The system is a binary mixture of water and salt (subscripts "w" and "s" respectively). The mass fraction of salt was defined at the inlet of the fiber ($\omega_{s,in}, dimensionless$).

$$\omega_s = \omega_{s,in} \quad @ \quad \text{z = 0 m} \quad (2\text{-}25)$$

The mass flux of water across the membrane/feed interface was defined by the model presented in equations 2-7 to 2-14.[50]

$$\vec{N}_w = -N(\vec{n}) \quad @ \quad r = R_i \quad \text{for Lumen Side Feed}$$
$$@ \quad r = R_o \quad \text{for Shell Side Feed} \quad (2\text{-}26)$$

Where $\vec{n}$ is the normal vector pointing away from the feed stream ($dimenionless$). The inlet mass fraction of salt was defined for sea water $\omega_{s,in} = .035$ and the diffusion coefficient for salt in water was estimated as $D_{sw} = 10^{-10} m^2/s$.[67,68] Along the boundaries not described as having boundary conditions, planes of symmetry were defined in accordance with figure 2-1.

2.7. Polarization Phenomena

A vital part of the analysis presented in this work considers the boundary layers formed by temperature and concentration. Equation 2-18 shows that, if N is positive, a negative heat flux should be observed which is indicative of the removal of heat from the process. The removal of heat will lead to a reduction in temperature along the membrane/ feed interface.[69] N, as determined by equation 2-7, is dependent on saturation pressure, and saturation pressure on temperature (as shown in equation 2-12). These equations then

indicate that, as a positive N leads to a decrease in temperature, the resultant decrease in temperature should lead to a reduction in N. This is the effect of temperature polarization. [69]

Another type of polarization occurs as a result of an increase of salt concentration along the membrane/feed interface. A positive value for N leads to a negative flux of water in equation 2-26 which is indicative of the removal of water from the feed stream. The removal of water from the feed stream leads to an increase in the concentration of salt along the membrane/feed interface.[69] As with temperature, saturation pressure is dependent on salt concentration by way of the activity coefficient of saltwater. By equation 2-13 an increase in salt concentration leads to a decrease in the activity coefficient. A decrease in the activity coefficient leads to a decrease in saturation pressure by equation 2-12 and therefore water vapor flux. This is the effect of concentration polarization. [69]

Thus far, these polarization phenomena are considered to occur within the boundary layer along the membrane/feed interface. The removal of water and energy from the feed stream generates a disequilibrium. The bulk feed stream will have a higher concentration of water and a higher temperature than the feed stream at the membrane interface and so heat and mass transfer will occur between the bulk and the interface until equilibrium is reached (as shown by equations 2-16, 19, 21, and 24).[69] These transport phenomena then occur within the feed stream at a rate which is proportional to the gradient of temperature and concentration.[69]

If one considers the case of a stagnant fluid in which no flow occurs this gradient will continually reduce unless the “source,” in this case the bulk fluid, is either brought

into equilibrium with the boundary, or temperature and concentration can be replenished so as to maintain the gradient.[69] If flow is induced that is orthogonal to the direction of the gradient one can see that the bulk feed is continually replenished and so the gradient is constant.[69] In the case of a non-slip condition a velocity profile is generated in which the velocity increases parabolically towards the center of the bulk fluid.[69] As velocity of the bulk fluid increases, velocity of the fluid near the boundary, but not at the no-slip condition, must also increase to maintain this continuum and so the gradient may be increased and maintained by the continual replenishment of these regions.[69] It then would require a fiber of significant length to reach equilibrium in the feed. This region near the no slip condition is called the boundary layer and is characterized by a sharp increase in concentration and reduction in temperature caused by the transport phenomena described above. Changing the velocity allows one to manipulate the thickness of this boundary layer and the significance of polarization.[69]

The membrane module is the key component of the desalination system. It is the point at which saltwater is converted to freshwater. By making use of several key assumptions the overall computational domain for the membrane module can be limited to only the seawater feed to the system.[50,51] A definition based on Darcy's law allows the permeate flux, the key measure of the module's performance, to be determined as a boundary condition.[50] That definition provides the most meaningful boundary condition for heat and mass transfer within the feed stream. Complete definition of the physics present within the membrane module allows the thermodynamics of the overall process to be considered in greater detail.

CHAPTER 3

EXERGY ANALYSIS

Exergy is defined as "the maximum amount of work theoretically available by bringing a resource into equilibrium with its surrounding through a reversible process." [70] More simply put, exergy is the useful energy available in a process. Exergy analysis is a useful tool for evaluating the thermodynamic efficiency of a process. Any real process necessarily involves the generation of entropy.[70,71] The magnitude of entropy generation is reflective of thermodynamic inefficiencies present in the process.[70,71] Where an energy balance can be used to evaluate the energy efficiency of a system, an exergy balance can be used to evaluate the exergy efficiency of the system.[70] Equation 3-1 shows the general energy balance for a system at steady state:[70]

$$\{\dot{H} + \dot{q} + \dot{W}_s\}_{in} = \{\dot{H} + \dot{q} + \dot{W}_s\}_{out} \tag{3-1}$$

Where $\dot{H}$ is the flow rate of enthalpy (associated with material) entering or leaving the system, $\dot{q}$ is the rate of heat generated or consumed by the system, and $\dot{W}_s$ is power generated or consumed by the system (all with units W). Each of these terms is analogous to one in the general exergy balance:[70]

$$\{\dot{Ex} + \dot{q}\left(1 - \frac{T_0}{T_s}\right) + \dot{W}_s\}_{in} = \{\dot{Ex} + \dot{q}\left(1 - \frac{T_0}{T_s}\right) + \dot{W}_s\}_{out} + \dot{Ex}_{irr} \tag{3-2}$$

In this equation $\dot{Ex}$ is the rate of exergy associated with a material entering or leaving the system (retaining the units W). The heat transferred to or from the system is unchanged except for its multiplication by the term $1 - T_0/T_s$ which one should easily recognize as the Carnot efficiency between a source of temperature T_s (K) and a sink of temperature T_0 (K).[70,71] Another difference should be readily apparent between these

two steady state equations. In equation 3-1 input and output are equivalent, this is reflective of the first law of thermodynamics and the conservation of energy.[71] In equation 3-2 the input and output terms are not equivalent but differ by the term $\dot{E}x_{irr}$. $\dot{E}x_{irr}$ is the exergy lost within the system due to thermodynamic irreversibility.[70] The addition of this term to equation 3-2 reflects the second law of thermodynamics, the generation of entropy which is non-negative.[70,71] It is this term $\dot{E}x_{irr}$ which is the focus of exergy analysis. Usefully, all the information necessary to determine $\dot{E}x_{irr}$ by equation 3-2 is known if the mass and energy balances of the system are defined. $\dot{E}x_{irr}$ can be represented in two ways, first by calculating it directly, second by the determination of *exergy efficiency*:[70]

$$\eta_{II} = \frac{\dot{E}x_{out}}{\dot{E}x_{in}} \tag{3-3}$$

The energy balance is normally calculated relative to a reference state. In the exergy balance this reference state is called the "dead state" and is determined by the environmental conditions. Recalling the definition of exergy given above, when a system is in equilibrium with the surroundings no work can be performed and the process is "dead." The dead state can be very useful for simplifying calculations and is an important parameter when defining the system as shall be seen in the next section.

3.1. The Solar Thermal Desalination Process

Each of the above equations assumes a process across which the balance can be calculated. To perform this exergy analysis a solar thermal desalination process must be defined and its boundaries determined. In order to investigate the performance of the

membrane module for use in a solar thermal desalination system, a general solar thermal desalination process was defined (figure 3-1). [72] In this process, seawater at 288 K is fed to the system and passes a heat exchanger where it is heated by an effluent brine. From the heat exchanger the feed enters a mixing/buffer tank where it is mixed with the brine generated by the membrane module. A stream is drawn off from the buffer tank and sent to the solar heater where sufficient heat is added to the stream to raise it to the desired feed temperature of the membrane module. The feed then enters the membrane module where it undergoes separation. The membrane module generates a brine which is returned to the buffer tank. The permeate leaves the membrane module and is condensed using another cool seawater feed and leaves the system as fresh water. The cool seawater used for condensation can be thought of as the feed to an R.O. plant or simply any other utility. An effluent brine is drawn off the buffer tank to maintain steady state within the system.

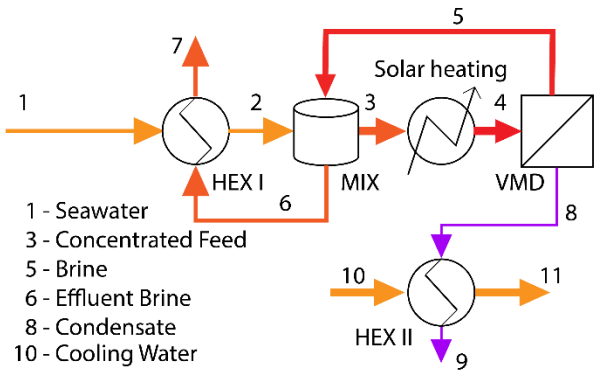

Figure 3-1: Solar thermal desalination process used for exergy analysis.

To define the system, stream 1 is given a basis mass flow rate, salinity, temperature, and pressure, thus defining all mass and energy parameters of that stream.

The temperature of stream 4 (entering the module) is defined in conjunction with the solutions to the membrane module as determined in the previous chapter (see equation 2-17). An overall recovery ratio defines the mass flow rates and salt concentrations of streams 7 and 9 (stream 9 is pure water therefore all salt in stream 1 must leave the system in stream 7). Stream 7 is assumed to leave the process at a temperature that is 10 K higher than the temperature of stream 1 as an assumption of the minimum temperature difference of the heat exchanger.[70,73] Stream 9 leaves the process as a saturated liquid at the vacuum pressure and therefore has a defined temperature. A basis mass flow rate is defined for stream 10 that allows the water vapor to be completely condensed (the chemical and thermodynamic properties of stream 10 are identical to stream 1). Finally, the model presented in chapter 2 allows a single pass recovery ratio to be defined for the membrane module. With these bases established the entire mass and energy balance may be calculated. Thermodynamic properties of the various streams were determined using publicly available steam tables and seawater properties.[74–76]

3.2. Exergy Balance

3.2.1 Overall Balance

Recall that the exergy balance is not identical to the energy balance, but, a fully defined energy balance allows the exergy balance to be defined.[70] Signorato et al. present another definition for the exergy balance presented in equation 3-2, this time for a non-steady state desalination process:[77]

$$Ex_t - W_t = \frac{d}{dt}(A^t)_{cv} + \sum_{i=1}^{N} m_i (b^t)_i + \sum_{i=1}^{N} m_i \xi_0 + Ex_{irr} \qquad (3\text{-}4)$$

On the left hand side of equation 3-4, Ex_t is the net thermal exergy flux (into or out) of the system (W) associated with $\dot{q}$ in equation 3-1, and W_t is the net mechanical power done on or by the system (W) associated with $\dot{W}_s$ in equation 3-1. On the right hand side a transient term is present that considers the Gibbs free energy and kinetic and potential energy changes of the overall control volume.[77]

$$A^t = U + p_0V - T_0S + E_k + E_p \quad (3\text{-}5)$$

Where U , p_0, V , T_0 , and S , are respectively the internal energy (J), dead state pressure (Pa), volume (m^3), dead state temperature (K), and entropy (J/K) for the control volume. E_k and E_p are the kinetic and potential energies of the control volume (J).

The two summation terms on the right hand side of equation 3-4 consider the exergy of the flowing streams within the process. These terms only consider those streams that pass the boundary of the control volume. m_i is the mass flow rate of stream "i" and b_i^t is the specific flow exergy of that stream (assuming kinetic and potential energies are negligible):[77]

$$b_i^t = (h_i - h_i^*) - T_0(s_i - s_i^*) + (g_i^* - g_0) \quad (3\text{-}6)$$

Where h_i, s_i, are the specific enthalpy and entropy of stream "i" (J/kg and $J/kg \cdot K$ respectively). h_i^*, s_i^*, g_i^* are respectively the specific enthalpy, entropy, and Gibbs free energy of stream "i" at the restricted dead state.[77] In the restricted dead state the streams are said to be in thermal and mechanical equilibrium with the dead state but not in chemical equilibrium.[78] These terms are then functions evaluated at the constant dead state temperature and pressure but at the chemical conditions specific to the

individual streams.[78] The specific Gibb's free energy of the dead state is g_0. ξ_0 is the thermal flow exergy of the dead state $\xi_0 = h_0 - T_0 s_0$ and is a constant.[77]

Ex_{irr} is the total exergy destroyed in the process or that exergy lost to the irreversibility of the process. Thermodynamic irreversibility can be brought into the system in many ways and this term will be investigated in more detail in the following sections.

To highlight the role of membrane parameters in the system, the exergy balance in equation 3-4 was simplified to include only those components present in figure 3-1. A control volume was defined for the system so that the only materials crossing the boundary of that volume are the cool seawater feed, the effluent brine, the condensed permeate, and the coolant to the condenser (streams 1, 7, 9, 10, 11). Solar energy also crosses the boundary to be absorbed by the solar collector.

No mechanical components are present and no work is generated therefore W_t may be neglected. Similarly, the process is considered to be at steady state, therefore $\frac{d}{dt}(A^t)_{cv}$ may be neglected and $\sum_{i=1}^{N} m_i \xi_0 = 0$ (the sum of the mass flow rates entering and leaving the system is zero at steady state). The dead state is defined as the conditions at which stream 1 enters the system thus mb_1^t and $m_{10}b_{10}^t$ become 0 as well. Equation 3-1 then becomes:

$$Ex_{irr} = Ex_{solar} - m_7 b_7^t - m_9 b_9^t - m_{11} b_{11}^t \tag{3-7}$$

Where Ex_{solar} is the thermal exergy added to the process defined by:[70,77]

$$Ex_{solar} = Q_{solar}\left(1 - \left(\frac{4}{3}\right)\left(\frac{T_0}{T_{sun}}\right) + \left(\frac{1}{3}\right)\left(\frac{T_0}{T_{sun}}\right)^4\right) \tag{3-8}$$

Q_{solar} is the solar energy required to raise the temperature of stream 3 to the desired feed temperature. $T_{sun} = 6000K$ was used for the temperature of the sun.[70,77] Q_{solar}, as well as the various other parameters needed for the model were determined using the mass and energy balance described in the previous section. With the total process defined the exergy efficiency of the system was defined as:

$$\eta_{II} = \frac{m_7 b_7^t + m_9 b_9^t + m_{11} b_{11}^t}{Ex_{solar}} \quad (3\text{-}9)$$

3.2.2 Unit Operation Balances

One of the most powerful uses of exergy analysis is the understanding it provides regarding the irreversibilities present in the system.[70,79] To better understand how exergy is destroyed within the system, it is beneficial to perform the same overall exergy balance from the previous section over each unit operation present within the system. This leads to five new exergy balances: The heat exchanger, the mixing tank, the solar collector, the membrane module, and the condenser. For all unit operations the steady state assumption may be retained, and mechanical power neglected. The form of each unit operation balance will then be the same as equation 3-7 in which exergy lost to irreversibility is equal to the difference between the exergy entering and leaving the unit operation.

3.2.2.1 Heat Exchanger

If the control volume is limited to the heat exchanger, a new flow diagram is generated wherein only streams 1 and 6 are entering and streams 2 and 7 are leaving. The heat exchanger is used to recover heat from the effluent brine. Stream 6, the brine leaving

the mixing tank passes through a heat exchanger where heat is recovered by stream 1, the fresh feed stream. The cooled brine leaves the system and is discharged to the environment as stream 7 and the heated feed passes to the mixing tank as stream 2. The brine enters the heat exchanger at a temperature significantly above the fresh feed stream. The cooled brine is defined as leaving the heat exchanger at a temperature that is 10 K above that of the fresh feed that enters. Thus exergy is lost in the heat exchanger due to heat transfer between the streams as well as temperature and chemical disequilibrium caused by the discharge of a concentrated stream at high temperature to the environment.[70,79] Equation 3-10 shows the exergy balance over this heat exchanger defined by the flow of these four streams. The exergy lost within the heat exchanger is $Ex_{irr,HX}$. Note b_1^t vanishes due to stream 1 entering the system at the dead state condition.

$$Ex_{irr,HX} = m_1 b_1^t + m_6 b_6^t - m_2 b_2^t - m_7 b_7^t \quad (3\text{-}10)$$

3.2.2.2 Buffer Tank

The buffer tank exists primarily to control the transient behavior of the process. The process can only ever operate at a pseudo-steady state. The rising and setting of the sun over the course of each day leads to a non-constant rate of solar energy absorption. [80] The buffer tank allows energy to be stored in the process so that at times when solar irradiance is unavailable desalination can still be run and the process is less dependent on daily variances in solar irradiance. [81] During startup, the whole system is considered to be in mechanical and thermal equilibrium with the dead state. Solar energy is collected in excess of the steady state value to raise the temperature of the buffer tank to the desired

steady state temperature of the membrane feed. Once that temperature is reached, solar energy is only required to recuperate heat lost via distillation. Thus, at steady state, the buffer tank serves primarily as a mixing point for the recycle and fresh feed streams. Irreversible exergy losses in the buffer tank, $Ex_{irr,Tank}$, are caused by mixing of streams at different temperatures and concentrations.[70,80] The buffer tank receives stream 2, the heated feed leaving the heat exchanger, and stream 5, the concentrated brine leaving the membrane module. A feed is drawn off from the buffer tank as stream 3 which goes to the solar collector, and to maintain steady state stream 6, the effluent brine, is removed from the tank. Equation 3-11 shows the determination of $Ex_{irr,Tank}$ using the balance of these four streams.

$$Ex_{irr,Tank} = m_2 b_2^t + m_5 b_5^t - m_3 b_3^t - m_6 b_6^t \quad (3\text{-}11)$$

3.2.2.3 Solar Collector

The solar collector is used to add energy to the process and to enable the work of separation to be accomplished in the membrane module. Stream 3 enters the solar collector from the buffer tank and is heated by solar energy, Q_{solar}, of sufficient quantity to raise the temperature of that stream to the desired feed temperature. Stream 4 then leaves the solar collector and is sent to the membrane module as the hot feed to be separated. Stream 4 is the highest temperature stream of the process and should contain the greatest quantity of thermal energy. The exergy balance of the solar collector is the only unit operation balance to include an exergy term other than those introduced by the flow of material. Ex_{solar} is the exergy added to the process by the solar collector and has a naturally defined limit, similar to a Carnot efficiency, as defined by equation 3-8.

Exergy is destroyed in the solar collector by the heating of the feed stream and the transfer from the solar collector to the saline feed.[70,80] Equation 3-12 shows the exergy balance over the solar collector and the determination of exergy losses in the solar collector $Ex_{irr,SC}$.

$$Ex_{irr,SC} = Ex_{solar} + m_3 b_3^t - m_4 b_4^t \quad (3\text{-}12)$$

3.2.2.4 Membrane Module

The membrane module is the point at which fresh water is separated from the saline feed. Stream 4, the heated feed, enters the membrane module from the solar collector. A portion of that heated feed is evaporated and drawn off as water vapor (stream 6) and the remainder is recycled to the buffer tank as stream 5. Stream 5 is the most concentrated stream in the process. Exergy destroyed in the membrane module, $Ex_{irr,MM}$, occurs as a result of a number of phenomena. Heat transfer between the streams, evaporation of the water vapor and its expansion from the saturation pressure to the vacuum pressure, and chemical changes all contribute to the destruction of exergy.[70,80] Equation 3-13 shows the calculation for exergy destruction and the exergy balance over the membrane module.

$$Ex_{irr,MM} = m_4 b_4^t - m_5 b_5^t - m_8 b_8^t \quad (3\text{-}13)$$

The pressure drop within the flowing saline streams is most substantial in the membrane module due to the high flow rate through it and the constrictive nature of the module. Pressure drop calculations based on the Hagen-Poiseuille equation and the equivalent for turbulent flow showed that this pressure drop, and the pumping power necessary to overcome it, provided a negligible contribution to exergy losses.[82] On this

basis, pumping and pressure effects within the liquid streams were neglected and all liquid streams were considered to be at the dead state pressure.

3.2.2.5 Condenser

The final unit operation to be considered is the condenser. The vapor leaving the membrane module, stream 8, enters the condenser and is condensed to liquid water, stream 9. The condensation of the permeate water vapor is necessary to generate the final fresh water product and is a useful means of maintaining the vacuum within the membrane module. Depending on the recovery ratio desired in the process, the cooling duty required by the condenser may be too high for the fresh feed stream (stream 1) to accommodate.[71,83] Furthermore, condensation of the permeate at vacuum, rather than compressing it to atmospheric or some other higher pressure, lowers the saturation temperature and provides a limit to how high the temperature of the cooling stream can be raised.[71] To condense the vapor, another stream is required of sufficient flow rate and temperature to accommodate these restrictions. Stream 10 enters the process at the same dead state conditions as the fresh feed (stream 1) and is heated by the condensation of the vapor and leaves the system as stream 11. Exergy is then destroyed in the condenser by condensation of the vapor, heat transfer between the streams, as well as thermal and chemical disequilibrium of the streams leaving the system.[70,80] Equation 3-14 shows the exergy balance for the condenser and the quantity destroyed in the operation, $Ex_{irr,Cond}$. Note again, as with b_1^t in equation 3-10, b_{10}^t vanishes due to its existence at the dead state.

$$Ex_{irr,Cond} = m_8 b_8^t + m_{10} b_{10}^t - m_9 b_9^t - m_{11} b_{11}^t \quad (3\text{-}14)$$

The total exergy destroyed in the system, as found in equation 3-7 should be equal to the sum of the exergy destroyed in each of the unit operations (see equation 3-15).[70,77,80] To compare how significant each unit operation is towards contributing to the overall irreversibility of the process, a relative contribution can be defined as the ratio of the exergy destroyed by that unit operation to the overall exergy destruction of the process (equation 3-16). Here, f_{Unit}, is the relative contribution of whatever unit operation and $Ex_{irr,Unit}$, is the exergy destroyed by that same unit.[77]

$$Ex_{irr} = Ex_{irr,HX} + Ex_{irr,Tank} + Ex_{irr,SC} + Ex_{irr,MM} + Ex_{irr,Cond} \quad (3\text{-}15)$$

$$f_{Unit} = \frac{Ex_{irr,Unit}}{Ex_{irr}} \quad (3\text{-}16)$$

Analysis of each unit's contribution can indicate the areas of the process that present the greatest opportunity for improvement. It should be noted, however, that each of the units presented is near to its ideal state. For instance, the solar collector, membrane module, and buffer tank do not consider heat loss terms which are known to contribute to the inefficiency of the process.[77] Thus for many of these unit operations the exergy destroyed should be considered the minimum of that operation within this process design.

CHAPTER 4

RESULTS AND DISCUSSION

The models described in the above chapters allow for complete description of the process being investigated. COMSOL Multiphysics® was used for the finite element modelling portion described in chapter 2. Mass, energy, and exergy balances were defined in MATLAB® and solved to complete the exergy analysis. These results shed light on the transport phenomena of the membrane module and the thermodynamic performance of the process as a whole.

4.1. Finite Element Modelling

4.1.1 Effect of Membrane Parameters

The model presented in chapter 2 was solved using the parameters detailed in table 4-1. The velocity, temperature, and concentration profiles generated by this solution are shown in figure 4-1. These profiles show the polarization phenomena described in chapter 2. The increase in salt concentration and the reduction of temperature is extremely localized to the membrane boundary. Later discussion will investigate the significance of these boundary layers and the relative effects of them on the performance of the membrane module.

Table 4-1: Operating parameters and constants.[60]

Parameter	Value	Parameter	Value
$T_{f,in}$	$333 - 353$ K	d_p	$200 - 500$ nm
P_{vac}	5 kPa	τ	$2 - 4$
$u_{f,in}$	5 m/s	ϵ	$0.5 - 0.9$
R_i	350 μm	L_m	$2.5 - 7.5$ cm
δ_m	$150 - 400$ μm	$\omega_{s,in}$	0.35

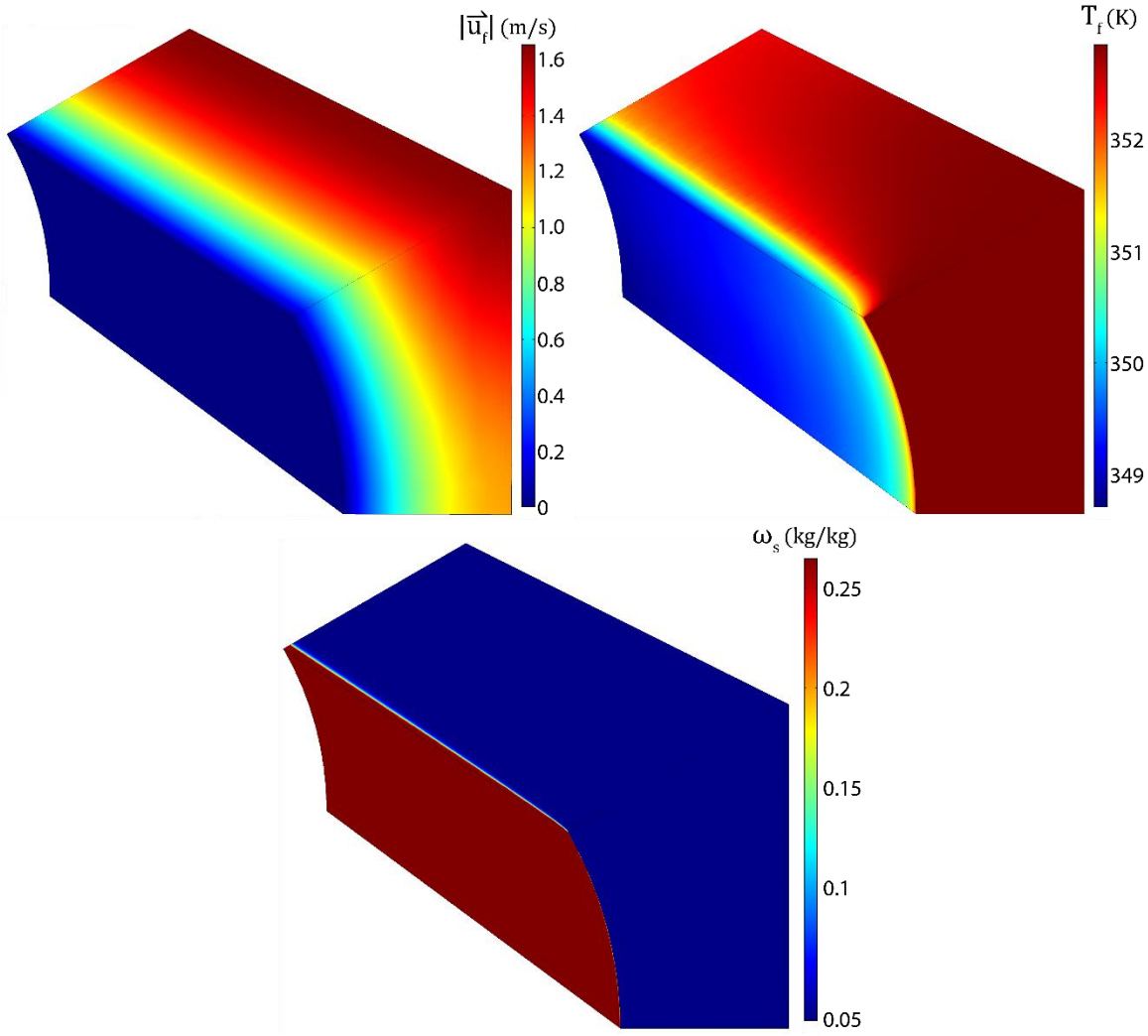

Figure 4-1: Top Left: Velocity profile. Top Right: Temperature profile. Bottom: Concentration profile. Shell side feed. Inner radius 350 µm, thickness 300 µm, R/a 0.35, length 5 cm, feed velocity 1 m/s, vacuum pressure 5 kPa, tortuosity 2, pore diameter 400 nm, porosity 0.5.

4.1.1.1 Effect of Fiber Length

Figure 4-2 shows the profile for permeate flux along the length of the fiber. The black lines indicate the localized value for the permeate flux at a certain axial distance from the fiber inlet. The red lines indicate the average flux along an entire fiber of that length. The decrease in permeate flux that occurs as axial distance from the fiber inlet increases is reflective of the polarization phenomena described in section 2.6. For a feed temperature of 353 K at the given membrane conditions the permeate flux at the inlet to the fiber can be expected to be around 65 LMH but at the outlet of a 7.5 cm fiber the permeate flux is reduced to slightly lower than 45 LMH. As distance from the fiber inlet increases the reduction occurs very quickly initially but then more gradually indicating the formation of a stable boundary layer of increased salt concentration and decreased temperature.[69]

These polarization phenomena are very significant in the membrane distillation process and can greatly limit the effectiveness of it. As figure 4-2 shows, increasing the feed temperature also increases magnitude of this drop in flux. This is for the same reason as discussed in chapter 2.6. The boundary layer formation described in chapter 2.6 is defined by the magnitude of the permeate flux (N). The smaller the permeate flux the less heat is transferred ($\vec{q}_m$). The phenomena that lead to the boundary layer are less significant at lower temperature and so the boundary layer is less pronounced. This becomes significant when one considers the energetic requirements of membrane distillation. MD relies on thermal energy provided to the system to evaporate water.[84] The energy requirement is significant due to both the high heat capacity of water and the

high heat of vaporization.[22] This severely limits the energetic efficiency of the process and makes fiber length an important parameter for design and optimization.

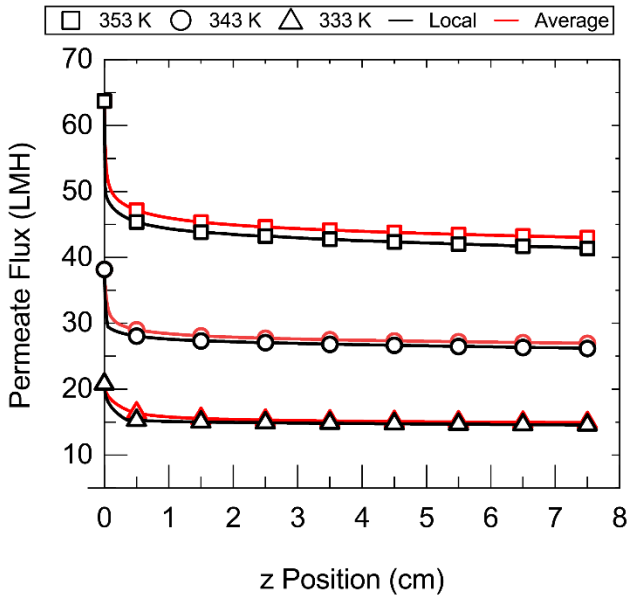

Figure 4-2: Localized permeate flux and average flux as fiber length increases. Shell side feed. Inner radius 350 µm, thickness 300 µm, R/a 0.35, feed velocity 1 m/s, vacuum pressure 5 kPa, tortuosity 2, pore diameter 400 nm, porosity 0.5.

The other significant problem with polarization is the increased propensity for scaling (which was not accounted for in this model).[56,85,86] A decrease in temperature lowers the solubility of salt in water and the increased salt concentration drives the solution towards this limit. Scaling on the surface of the membrane reduces the number of open pores and increases the wettability of the fiber.[56,85,86] Reduction of the number of open pores lowers permeate flux.[56,85,86] If water can't access a pore it can't transfer through it. Increased wettability means the process may need to be run at

higher a pressure on the vacuum side or risk contaminating the permeate.[56,84] In any case, fiber length is a key determining factor in the effectiveness of the VMD process.

4.1.1.2 Effect of Porosity

Figure 4-3 shows the effect of membrane porosity on the average permeate flux of a full membrane. Porosity is defined by the void fraction of a membrane, or, the volume of a membrane that is not occupied by the membrane material.[32] The less membrane material is present the less resistance the membrane has towards mass transfer and therefore flux can increase.[32] Equations 2-7 to 2-10 predict a linear relationship between porosity and permeate flux. This predicted relationship is largely maintained in the average flux. Permeate flux increases approximately linearly with porosity. The slope of this linear relationship is determined by feed temperature. Lower feed temperatures observe a smaller slope than higher feed temperatures. This is because ΔP and P_m in equations 2-7 and 2-10 respectively are larger. The same change in porosity leads to a larger change in the overall slope determined by equations 2-7 through 2-10. A slight concavity is present in the data sets due to polarization. Higher values of permeate flux at the inlet lead to more significant polarization and a degradation in average flux. In all, an increase in the permeate flux of about 25 LMH is achieved by increasing the membrane porosity at the highest feed temperature.

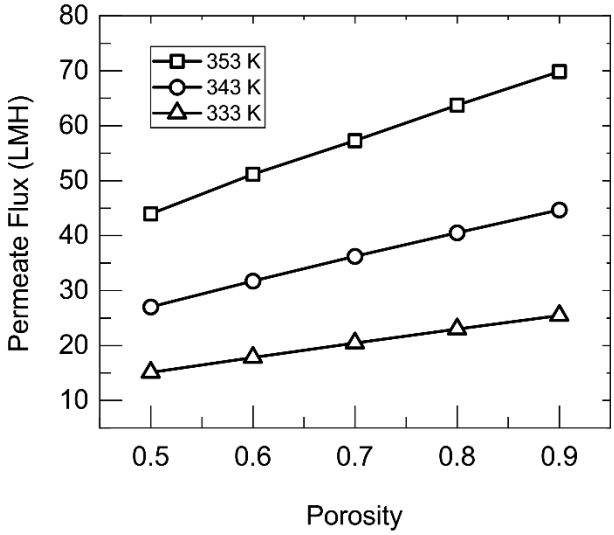

Figure 4-3: Average permeate flux as porosity changes. Shell side feed. Inner radius 350 µm, thickness 300 µm, R/a 0.35, length 5 cm, feed velocity 1 m/s, vacuum pressure 5 kPa, tortuosity 2, pore diameter 400 nm.

4.1.1.3 Effect of Pore Diameter

Pore diameter, like porosity, maintains a linear relationship with average flux due to its presence in the numerator of equations 2-9 and 2-10 (figure 4-4). Like porosity a larger pore diameter provides more space for vapor to transport through the membrane and therefore increases flux. The larger change in pore diameter shows more dramatically the effect of changing temperature on the slope of inlet permeate flux (relative to its effect in porosity). Unlike porosity, pore diameter does not have a natural limit. Porosity can never exceed 1, however pore diameter may increase to any value so long as the liquid entry pressure is not reached.[32,87] Each of these parameters achieved similar increases in flux at the 353 K feed temperature over the range of parameters tested, however, Pore Diameter can continue to increase while porosity is limited by its nature.

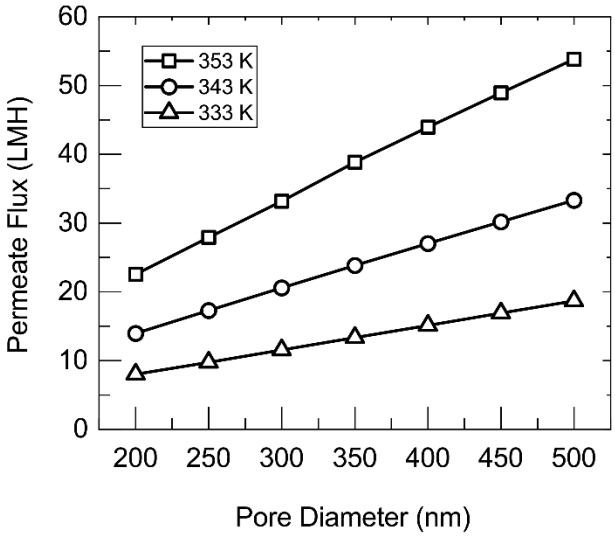

Figure 4-4: Average permeate flux as pore diameter changes. Shell side feed. Inner radius 350 µm, thickness 300 µm, R/a 0.35, length 5 cm, feed velocity 1 m/s, vacuum pressure 5 kPa, tortuosity 2, porosity 0.5.

4.1.1.4 Effect of Thickness

The effect of thickness is again predicted well by equations 2-9 and 2-10. The permeate flux largely follows an inverse proportionality with membrane thickness. Membrane thickness is integral to the determination of driving force. The pressure difference across the membrane is the driving force in equation 2-6. As the length across which the gradient is determined decreases, flux increases. The limit to membrane thickness, as in reverse osmosis, is the mechanical strength of the membrane.[88] It has become common practice to construct membranes using a support layer of high void fraction that can add strength to a very thin membrane or hydrophobic coating which provides the driving force.[88] An increase of almost 45 LMH is achieved by reducing

the membrane thickness. As thickness continues to decrease the permeate flux can be expected to continue to increase until mechanical limits are reached.

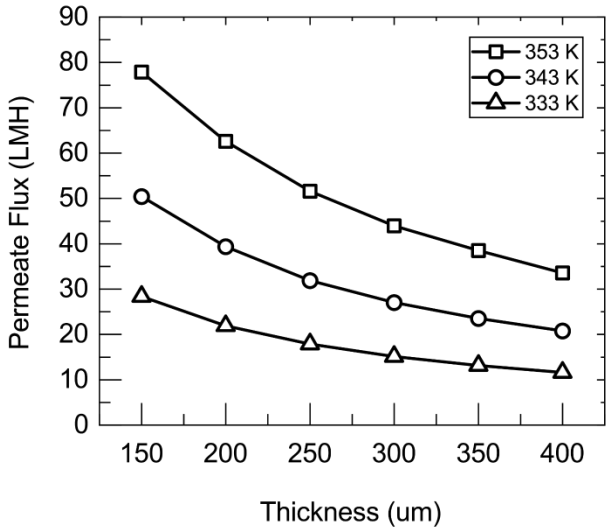

Figure 4-5: Average permeate flux as membrane thickness changes. Shell side feed. Inner radius 350 μm, R/a 0.35, length 5 cm, feed velocity 1 m/s, vacuum pressure 5 kPa, tortuosity 2, pore diameter 400 nm, porosity 0.5.

4.1.1.5 Effect of Tortuosity

Figure 4-6 shows the effect of tortuosity on membrane performance. Tortuosity occurs in the denominator of both equations 2-9 and 2-10 and this inversely proportional relationship is reflected in figure 4-6. Permeate flux decreases with an increase in tortuosity. Tortuosity is a measure of how far a water molecule must stray in from a linear path order to travel through the membrane.[32] If, on average, a water molecule can travel through the membrane while never deviating from the shortest route the tortuosity is 1. Higher tortuosities are indicative of more “winding” paths. As above, the effect of this change in tortuosity is more dramatic for higher feed temperatures due to

the larger ΔP and P_m terms. An increase of about 20 LMH is achieved by increasing the tortuosity within the range described.

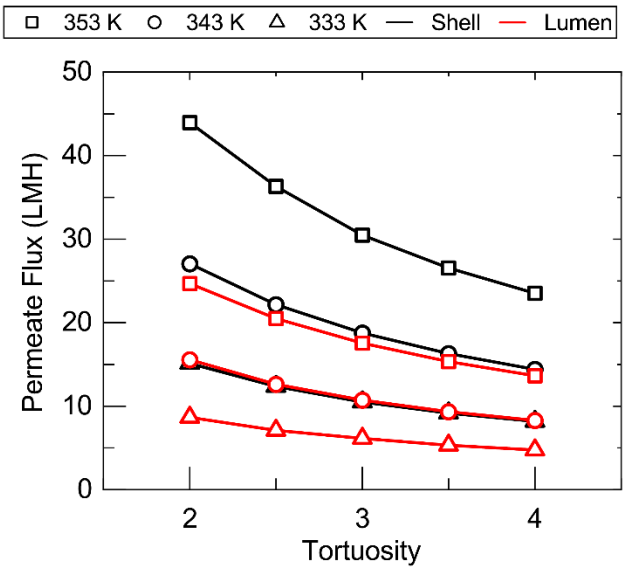

Figure 4-6: Average permeate flux as tortuosity changes. Inner radius 350 µm, thickness 300 µm, R/a 0.35, length 5 cm, feed velocity 1 m/s, vacuum pressure 5 kPa, pore diameter 400 nm, porosity 0.5.

Figure 4-6 also shows a comparison between a lumen and a shell side feed. The lumen side feed sees significantly lower average permeate flux compared to a shell side feed. This is primarily caused by the way in which the average is calculated. The average is taken as the average permeate flux at the outer radius of the membrane. For the lumen side feed the permeate flux is divided by a relatively larger area which leads to a decrease in flux proportional to the difference in the area at the outer and inner sides of the membrane. This reduction is also caused by the buildup of salt along the membrane surface. In a cylindrical geometry mass transfer occurs more quickly in the direction of increasing radius than it does the direction of decreasing radius.[69] This is because as

radius increases the surface area for mass transfer increases and a reduction in the radius leads to a reduction of surface area. As such, when salt concentration builds up on the membrane surface it can more readily diffuse away from the membrane in a shell side feed than a lumen side feed.

4.1.2 Determination of Limiting Phenomenon

As noted, polarization occurs as a result of a reduction in temperature and an increase in salt concentration.[85] A comparison must be made between the two phenomena to find the limiting factor. Figure 4-7 shows the saturation pressure of water at the surface of the membrane under two conditions. The black lines indicate the actual saturation pressure calculated by equation 2-12. The red lines indicate the saturation pressure based solely on Antoine's equation (defined as P_{sat}/a_w). The red lines are only a function of temperature while the black lines are a function of both temperature and salt concentration. The difference in the two functions is the effect of salt concentration.

While both phenomena contribute to the reduction in saturation pressure, the increase in salt concentration along the membrane surface is most significant. This can be most readily observed at the 333 K feed temperature. The reduction of Antoine's equation is almost negligible while there is still a notable reduction in saturation pressure overall. At each of the three feed temperatures the saturation pressure decreases most significantly towards the inlet of the fiber as salt concentration increases. At a certain point, the salt concentration reaches saturation and cannot increase. At this point only does the contribution of temperature become visible. From that point on the saturation pressure behaves as a translation of Antoine's equation. At 353 K this saturation point is

reached almost immediately. At 343 K the saturation concentration is reached after less than 1 mm and at 333 K the phenomenon occurs more gradually, and saturation is reached at 5 mm. These effects can also be observed in the local permeate and average permeate flux values in figure 4-2. The majority of the loss of average and local permeate flux occurs towards the inlet of the fiber until saturation is reached and degradation of flux is more gradual for the remainder of the fiber's length.

To quantify this significance of salt polarization relative to mass one must observe the respective diffusivities. The mass diffusivity of salt in water is known to be on the order of $10^{-10} m^2/s$ [68], while the thermal diffusivity of water is on the order of $10^{-7}\ m^2/s$.[89] The three order of magnitude difference between these numbers is reflected in the results shown in figure 4-7 and confirms that salt concentration must be the limiting factor. Salt concentration is significant in another way. Scaling is known to be a problem in desalination systems.[85] As concentration in the boundary layer increases so does scaling. [61,62,90] As crystalline salt forms on the surface of the membrane it can block pores and inhibit flux. The model presented here is limited in that it does not present a kinetic model for scaling and cannot take into account how scaling will change membrane performance. Unlike salt, temperature does not have a saturation value that limits its effect on membrane performance. As length increases, temperature polarization becomes more apparent and will eventually become the determining factor in membrane performance.

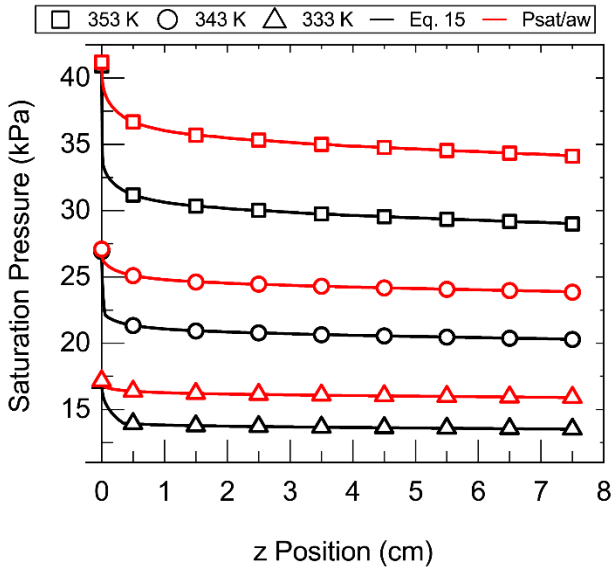

Figure 4-7: Saturation pressure as a function of fiber length. Shell side feed. Inner radius 350 µm, thickness 300 µm, R/a 0.35, length 5 cm, feed velocity 1 m/s, vacuum pressure 5 kPa, tortuosity 2, pore diameter 400 nm, porosity 0.5.

4.1.3 Mitigation of Limiting Phenomena

One possible means of ameliorating the problem of polarization is to add some sort of baffling to the surface of the membrane.[84,91,92] Figure 4-8 shows one such method of baffling. A thin wire can be wrapped around the membrane to induce turbulence and break the boundary layer. The spacing between coils of the wire can be controlled to improve performance.

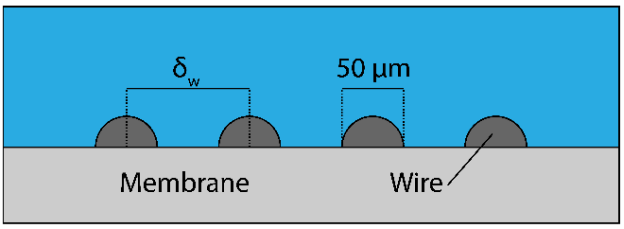

Figure 4-8: Baffling geometry.

The addition of this simple baffling scheme can lead to a noticeable improvement in membrane performance. Figure 4-9 shows a comparison of a baffled and an unbaffled fiber. A comparison is also made between feeds of different velocities. As velocity for a shell side feed increases the flow regime quickly enters the critical range between the laminar and turbulent regimes.[82] At a feed velocity of 5 m/s the flow is entirely within the turbulent regime. To account for this change in the physics of momentum transfer the Reynolds-averaged Navier-Stokes equations and Wilcox's revised $k-\omega$ turbulence model, built into the COMSOL Multiphysics® package, were used in lieu of equations 2-1 and 2-2 while retaining all the original boundary conditions.[93]

The addition of the baffling scheme increased permeate flux, though the magnitude of this increase depended significantly on the velocity and temperature of the feed. The increase was most significant at the higher feed velocity for the shortest baffling spacing. The basis of this increase follows the profiles of figures 4-1 and 4-6. The effect of baffling is in essence to cause a repetition of these profiles at each coil of the wire. Mixing of the fluid at each coil allows the conditions at the membrane interface to return to that of the bulk which does not substantially change from the conditions of the inlet over these lengths. Thus, for the 5 mm spacing, the first 5 mm of each profile is repeated at each coil of the wire and for the 1mm spacing the first 1 mm is repeated at each coil.

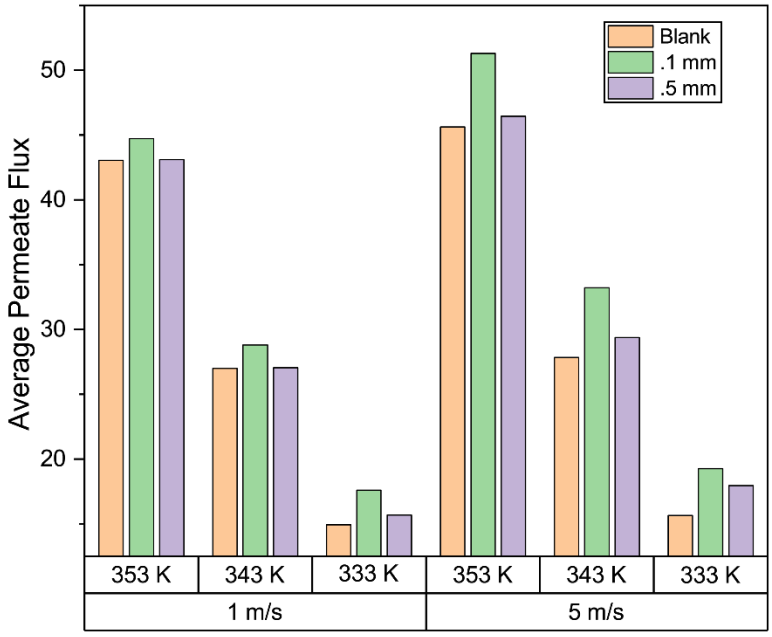

Figure 4-9: Average permeate different baffling spacings and feed velocities. Shell side feed. Inner radius 350 µm, thickness 300 µm, R/a 0.35, length 5 cm, feed velocity 5 m/s, vacuum pressure 5 kPa, tortuosity 2, pore diameter 400 nm, porosity 0.5.

As figure 4-7 shows, for the 333 K feed temperature at a 1 m/s feed velocity, salt concentration reaches saturation at about 5 mm from the inlet. For the higher feed temperatures this saturation is reached almost immediately. Because of this, for the 1 m/s feed velocity very little is to be gained by the addition of baffling except at the lowest feed temperature. Returning the membrane boundary to the conditions of the inlet within the first 5 mm does little to change the permeate flux as the significant majority of the fiber's length is still at the saturation condition (increases of about 0.04 LMH are observed at the higher feed temperatures). This is not true for the 333 K feed temperature and this leads to an appreciable increase in permeate flux (about 0.7 LMH).

When the distance between coils of the wire is reduced to 1 mm, the increase is substantial for all feed temperatures. The increase at the 353 K and 343 K feed temperatures is 1.7 LMH and 1.8 LMH respectively. Because the higher temperatures still reach saturation well before the first coil the increase is still most notable for the lower feed temperature which increases by 2.7 LMH.

When the feed velocity is increased the effect of baffling is more significant. This is caused first by an inherent increase in permeate flux as feed velocity increases. Increasing the feed velocity elongates the profiles observed in figures 4-1 and 4-6 such that saturation is reached further from the fiber inlet and temperature reduction is more gradual along the whole length of the fiber.[69] For the 5 mm spacing the increase in feed velocity leads to an increase of 1.5 LMH at the lower feed temperatures and 0.7 LMH at the 353 K feed temperature. The same trend was observed as in the 1 m/s feed velocity where lower feed temperatures achieved a more significant increase in permeate flux with the addition of the 5 mm baffling. This again was due to saturation being reached before the coils.

When the 1 mm spacing is applied at the higher feed velocity the most significant increases in permeate flux are observed. This spacing is short enough that at the 5 m/s feed velocity the boundary layer does not spend a significant amount of time at the saturation condition at any feed temperature. The result is that each feed temperature can achieve a significant increase in permeate flux. With the addition of baffling, the highest increase in permeate flux – 5.7 LMH – is observed at the 353 K feed temperature. Here, we also observed an increase of 5.4 LMH and 3.6 LMH in permeate flux for the feed temperatures of 343 K and 333 K, respectively. This reverses the trend observed for the

other feed velocities and spacings. Because saturation does not play as significant a role in determining the average flux at these spacings, the effect of baffling is more pronounced.

There is a twofold problem with this baffling scheme. First, the addition of the wire around the membrane covers a portion of the membrane and reduces the surface area of the membrane available for distillation. Decreasing the spacing covers more membrane area and reduces the actual surface area for mass transport. Second, the sharp, local, increase in salt concentration on the upstream side of the wire will result in an increase in scaling at that point. The first problem can be readily optimized to achieve best results. The second problem can be controlled by the addition of hydrophobic or omniphobic coatings to the surface of the membrane and whatever baffling is placed around it.[22] Reducing the distance between baffles to reduce salt concentration will also help to inhibit scaling by reducing the concentration of salt along the boundary.

4.2. Exergy Analysis

As a means of evaluating the thermodynamic performance of the VMD process an exergy analysis was performed as outlined in chapter 3. Table 4-2 shows the mass and energy balance for standard operating conditions of this process (in a shell side feed, 353 K feed temperature). One can see that the streams within the recycle loop contribute to the bulk of the mass flow within the system and are individually eight times larger in mass flow rate than the next most substantial streams which provide the coolant within the condenser. The reason for the significant increase in mass flow rate in these streams is

the extremely low single pass recovery ratio. Of the 433.02 kg/hr entering the membrane module only 0.65 kg/hr leaves as the permeate.

Because of the large flow rates of the recycle streams, the concentration of salt within the recycle loop is mostly constant and almost no change is observed after mixing with the fresh feed. The temperature of these streams is also mostly determined by the temperature of the feed stream.

Table 4-2: Mass and energy balance. Shell side feed. Inner radius 350 μm, thickness 300 μm, R/a 0.35, feed velocity 5 m/s, vacuum pressure 5 kPa, tortuosity 2, pore diameter 400 nm, porosity 0.5.

Stream	$m\ (kg\ hr^{-1})$	$\omega_s\ (kg\ kg^{-1})$	$T\ (K)$
1	1.00	0.035	288.00
2	1.00	0.035	305.71
3	433.02	0.100	351.95
4	433.02	0.100	353.00
5	432.37	0.10015	352.07
6	0.35	0.100	351.95
7	0.35	0.100	298.00
8	0.65	0.000	349.41
9	0.65	0.000	306.03
10	50.00	0.035	288.00
11	50.00	0.035	296.18

4.2.1 Effect of Membrane Parameters

Figure 4-10 shows the exergy efficiency of the process at various membrane porosities and feed temperatures. Exergy efficiency is seen to increase with feed temperature. The system is at a fixed overall recovery ratio, and all of the thermodynamic properties of the inlet and outlet streams are constant except for those of stream 11. Additionally, the mass flow rate of stream 11 is the largest of all those streams included

in equation 3-8. Increasing the temperature of the feed stream results in an increase in the temperature of stream 11 because more heat must be removed from the permeate vapor to lower it to the saturation point before condensation can occur. The increase in temperature of stream 11 leads to an increase in the specific enthalpy of that stream and, by equation 3-6, an increase in the specific flow exergy associated with the stream.[70,77] This leads to the increase in exergy efficiency shown in figure 4-10. The increase in exergy efficiency is about 0.01%.

While exergy efficiency increases with feed temperature generally, at a specific feed temperature, exergy efficiency decreases with single pass recovery ratio. One can see that exergy efficiency at a certain feed temperature decreases linearly with porosity, the reverse of what was observed for permeate flux in figure 4-3. Table 4-2 indicates that there is a reduction in temperature from stream 4 to stream 5. This is caused by heat leaving the feed stream with the permeate. This reduction in turn leads to a lower temperature of stream 3 after the mixing point. In order to raise the temperature of the feed to the desired feed temperature, Q_{solar} must be added to the system. Ex_{solar} increases linearly with the magnitude of Q_{solar} in equation 3-8. As the amount of energy absorbed by the feed stream increases, Ex_{solar} increases and exergy efficiency decreases. A higher recovery ratio results in a lower temperature for stream 3 and an increase in Q_{solar}. A difference of about 0.003 % is observed as a result of the increase in porosity at the 353 K feed temperature.

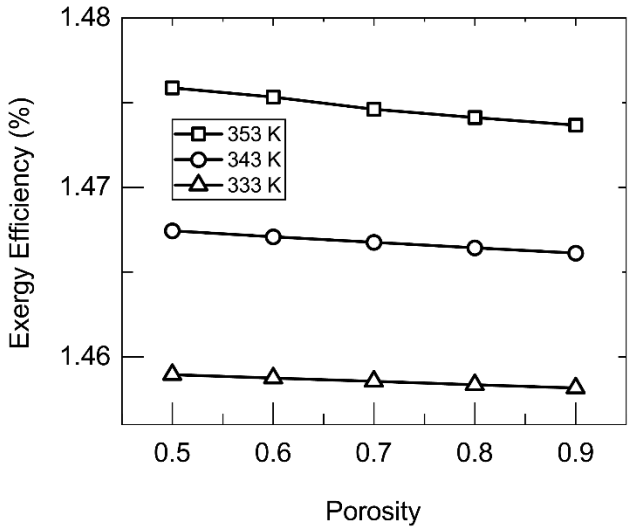

Figure 4-10: Exergy efficiency as porosity changes. Shell side feed. Inner radius 350 µm, thickness 300 µm, R/a 0.35, length 5 cm, feed velocity 5 m/s, vacuum pressure 5 kPa, tortuosity 2, pore diameter 400 nm.

Figure 4-11 shows the effect of pore diameter on exergy efficiency. As with porosity, feed temperature is dominant in the results and a lesser contribution is observed that follows the increase in permeate flux caused by increasing pore diameter. The effect is largely linear as it was with permeate flux. A decrease of approximately 0.0025% is observed for the highest feed temperature while and still smaller decrease of about 0.001% occurs at the lowest feed temperatures.

Figure 4-12 shows the effect of membrane thickness on exergy efficiency. The results again show the dominance of feed temperature in the results and a slight influence of membrane thickness on exergy efficiency. The inversely proportional relationship observed in permeate flux is reversed in exergy efficiency. This is most notably observed

at the highest feed temperature where an increase of 0.002% is observed in exergy efficiency over the range examined.

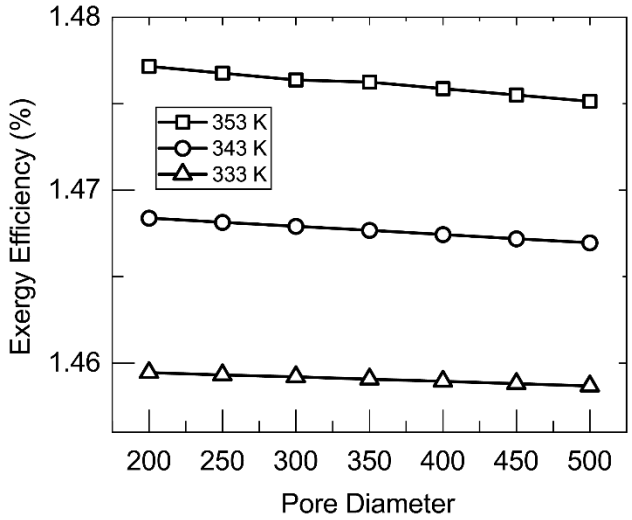

Figure 4-11: Exergy efficiency as pore diameter changes. Shell side feed. Inner radius 350 µm, thickness 300 µm, R/a 0.35, length 5 cm, feed velocity 5 m/s, vacuum pressure 5 kPa, tortuosity 2, porosity 0.5.

Figure 4-13 shows the effect of membrane tortuosity and feed configuration on exergy efficiency. Again, temperature is dominant and exergy efficiency decreases in an inversely proportional relationship to permeate flux. Unlike the case in permeate flux a far less substantial change is observable in exergy efficiency as feed configuration is changed from the shell to the lumen side of the membrane. The exergy efficiency values for the shell and lumen sides are almost equal. One reason for the elimination of the reduction seen in permeate flux is the effect of recovery ratio. Changing to a lumen side feed typically includes changing to a smaller volumetric flowrate of feed solution and an increase in recovery ratio relative to the shell side feed. The higher recovery ratio also

leads to a slightly smaller exergy efficiency observed in the lumen side relative to the shell side feed.

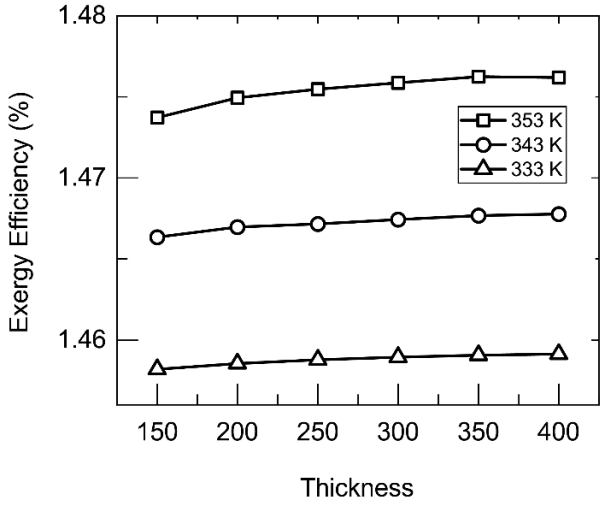

Figure 4-12: Exergy efficiency as membrane thickness changes. Shell side feed. Inner radius 350 µm, R/a 0.35, length 5 cm, feed velocity 5 m/s, vacuum pressure 5 kPa, tortuosity 2, pore diameter 400 nm, porosity 0.5.

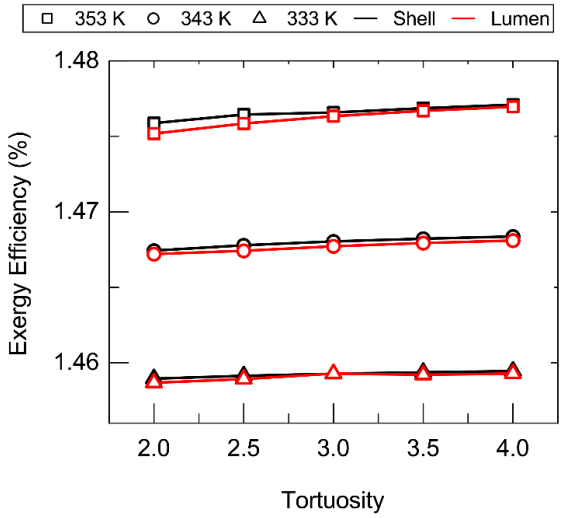

Figure 4-13: Exergy efficiency as tortuosity changes. Inner radius 350 µm, thickness 300 µm, R/a 0.35, length 5 cm, feed velocity 5 m/s, vacuum pressure 5 kPa, pore diameter 400 nm, porosity 0.5.

The addition of a baffling scheme has an almost unobservable effect on exergy efficiency. Figure 4-14 shows the effect of the baffling scheme on exergy efficiency, as well as the change caused by increasing the feed velocity. The very small increase caused by the addition of baffling is due to the increased recovery ratio which is enough to offset the slight increase in heat loss. A small increase in exergy efficiency is observed by increasing the feed velocity due to the reduction of heat loss. In all cases however the change in exergy efficiency is negligible indicating that baffling is ineffective in terms of addressing irreversibility.

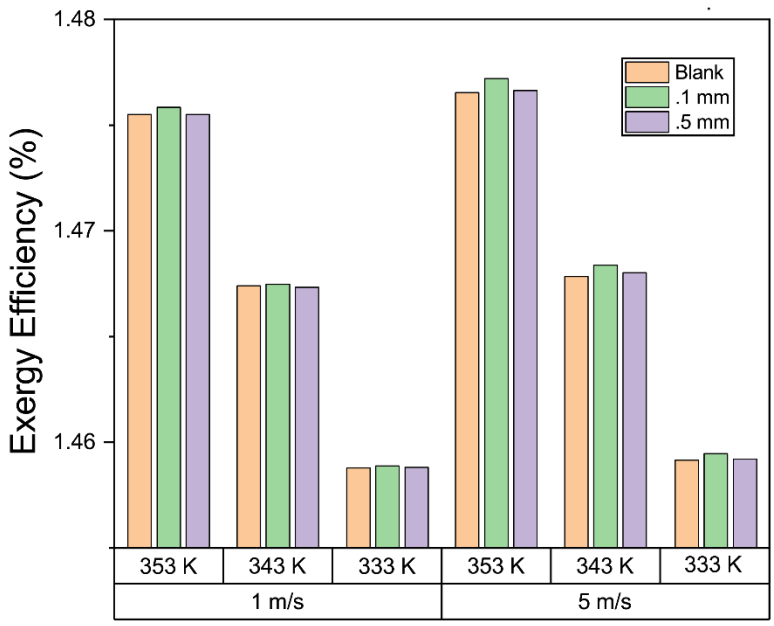

Figure 4-14: Exergy efficiency at various baffling spacings and feed velocities. Shell side feed. Inner radius 350 µm, thickness 300 µm, R/a 0.35, length 5 cm, feed velocity 5 m/s, vacuum pressure 5 kPa, tortuosity 2, pore diameter 400 nm, porosity 0.5.

4.2.2 Relative Contributions of Unit Operations.

As discussed in section 3.2.2 each of the unit operations present in the system contribute differently to the exergy destroyed. Table 4-3 shows the magnitude of the irreversible exergy losses present in each unit operation as well as the total irreversible losses present in the system.

Table 4-3: Exergy destroyed in the various unit operations.

$T_{f,in}$ (K)	Feed Side	$Ex_{irr,HX}$ (kJ/hr)	$Ex_{irr,Tank}$ (kJ/hr)	$Ex_{irr,SC}$ (kJ/hr)	$Ex_{irr,MM}$ (kJ/hr)	$Ex_{irr,Cond}$ (kJ/hr)	Ex_{irr} (kJ/hr)
353	Shell	5.92	13.90	1273.14	185.10	80.16	1558.23
	Lumen	5.71	12.83	1275.32	183.52	80.03	1557.41
343	Shell	4.45	10.24	1304.92	150.00	78.63	1548.24
	Lumen	4.32	11.02	1304.79	149.23	78.59	1547.96
333	Shell	3.11	5.75	1338.80	113.17	77.34	1538.15
	Lumen	3.05	8.45	1336.46	112.59	77.30	1537.84

In all cases the solar collector provides the bulk of the exergy lost to irreversibility. As temperature increases there is a reduction in exergy lost within the solar collector. The largest quantity of exergy lost in the solar collector is 1338.8 kJ/hr and occurs at a feed temperature of 333 K. This value is reduced to a minimum of 1273.14 kJ/hr lost at the 353 K feed temperature. Specific flow exergy and Q_{Solar} both increase as temperature increases. For a shell side feed, the specific flow exergy of stream 3 increases from 19.3 kJ/kg to 30.8 kJ/kg with the increase in temperature from 333 K to 353 K (a similar increase is observed in stream 4). Likewise, Q_{Solar} increases from 1667 kJ/hr to 1689 kJ/hr at the same temperatures. These should both tend towards an increase in exergy loss, however, the increase in temperature also brings with it a decrease in mass flow rate. At 333 K 1258 kg/hr are required to pass through the solar collector and

membrane module to achieve the desired water production, while at 353 K only 433 kg/hr are required to achieve the same production. This threefold decrease in mass flow rate offsets the increase in specific flow exergy which it is multiplied by. The result is a net decrease in exergy which passes through the solar collector and therefore a decrease in exergy which can be destroyed.

When the feed is changed from the shell side to the lumen the exergy lost within the solar collector decreases at lower feed temperatures but increases at the highest feed temperature. At a 353 K feed temperature, a change from a shell to a lumen side feed results in a 2.18 kJ/hr increase in exergy destruction, while the 343 K and 333 K feed temperatures achieved reductions of 0.13 kJ/hr and 2.34 kJ/hr respectively. The difference in behavior at different feed temperatures is the result of a change in the functionality of exergy loss within the solar collector between the different configurations. For both the shell and lumen side feed exergy loss decreases mostly linearly with an increase in temperature. For the lumen side feed the slope of this decrease (about 3 kJ/hr/K) is slightly less than the shell side feed (about 3.2 kJ/hr/K). This change is predominantly caused by the decrease in mass flow rate. The mass flow rate of the lumen side feed is lower due to the increased recovery ratio of the lumen. The lower flow rate means that less change is possible by increasing temperature and so the magnitude of this change is reduced.

Heat loss also plays a role in the change to the lumen side feed. As heat is lost in the membrane module Ex_{Solar} must change to account for it. Heat loss is maximized for a lumen side feed at a 353 K feed temperature. That increase in heat loss means that, as temperature increases, Ex_{Solar} must increase relative to the other exergy terms in equation

3-12. For a lumen side feed at the 333 K feed temperature Ex_{Solar} is about 15 % of the flow exergy contained in stream 4 at the 353 K feed temperature Ex_{Solar} is 27 % of the flow exergy of stream 4. This increase is aided by the decreased mass flow rate of stream 4 as well at higher recovery ratios. Ex_{Solar} itself is reduced by the change from a shell to a lumen side feed because of the reduced flow rate, however its magnitude relative to the other terms in equation 3-12 increases such that it is able to achieve a net increase in exergy lost within the solar collector at the highest feed temperature. For lower feed temperatures the heat loss is not significant enough to overcome the reduction of total exergy due to flow rate and the overall exergy lost by changing the feed to the lumen is reduced.

The membrane module provides the next largest quantity of exergy destroyed. The exergy within the membrane module is dominated by streams 4 and 5 due to their significantly higher flow rates than that of stream 8. As with the solar collector, the decrease in mass flow rate leads to a decrease in flow exergy for each stream. Despite this, at higher feed temperatures, more vapor is generated and so the mass flow rate of stream 5 relative to stream 4 is reduced. Stream 4 always loses 0.65 kg/hr to stream 8 regardless of the conditions of a particular solution. This loss, however, is much more significant at the 353 K feed temperature, where the mass flow rate is 433 kg/hr, than it is at the 333 K feed temperature when the mass flow rate of stream 4 is 1259 kg/hr. The same follows for the temperature of stream 5, though the temperature of stream 5 may rise with feed temperature, the increased recovery ratio results in an increased amount of heat lost. Thus, while the temperature of stream 5 is increased from 332.7 K to 352.1 K as stream 4 changes from 333 K to 353 K, the reduction of temperature changes from 0.3

K to 0.9 K. The result is that the flow exergy of stream 5 relative to stream 4 is reduced at higher temperatures and the exergy destroyed is increased.

The membrane module saw a small change as a result of changing the feed location. In all cases exergy destruction was reduced for a lumen side feed relative to a shell side feed. This is due to the reduced mass flow rate of streams 4 and 5. The lower mass flow rate and total flow exergy of each stream means that, while the phenomena described above (recovery ratio and heat loss) are magnified in a lumen side feed, the actual exergy destroyed is lower even though the exergy destroyed per mass of feed is increased. The mass flow rate of stream 4 is 433.0 kg/hr for a shell side feed and only 193.6 for a lumen side feed. Thus, while the phenomena that lead to an increase in exergy destruction with temperature are also magnified by changing to the lumen side feed, they are insufficient to overcome the change wrought by feed configuration.

The Condenser provided the median exergy destruction of all unit operations. As with the membrane module there was an increase in total exergy destruction at higher temperatures. This increase is due to the higher temperature of stream 8 and the higher enthalpy of that stream. Stream 8 leaves the membrane module at a temperature well above the saturation temperature of the vacuum pressure. That heat must be removed by the condenser in order to condense the vapor. That increase in heat transfer leads to an increase in exergy destruction. A small decrease in exergy destroyed by the condenser was observed by changing the feed from the shell to the lumen because of a small decrease in temperature of stream 8. For a lumen side feed, the reduced mass flow rate means less energy is available to heat stream 8 and the temperature is reduced. This change however was negligible.

The mixing tank and the heat exchanger each represent the smallest losses of exergy. Losses within the mixing tank amount to between 5 kJ/hr and 14 kJ/hr depending mostly on feed temperature. At higher temperatures, increased heat transfer results in a larger loss of exergy to irreversabilities. The heat exchanger accounts for between 3 kJ/hr and 5 kJ/hr of exergy lost. This again increases with the increased heat transfer rate at higher temperatures.

The magnitude of exergy losses in the respective unit operations are presented relative to the total exergy lost in figure 4-15. One can see that the solar collector, which accounts for the most heat exchanged within the process, produces the largest exergy losses and in all cases accounts for more than 80 % of exergy lost. As the quantity of exergy lost in the solar collector decreases, generally speaking, each of the other units increased in the quantity of exergy lost (as shown in table 4-3). This leads to a decrease in relative share of the solar collector in total exergy losses as temperature increases, but this decrease is never able to remove its significant majority.

From a thermodynamic standpoint then the greatest opportunity for improvement is present in the solar collector, however, these calculations represent the minimum exergy lost within the solar collector. Inefficiencies are present in commercial solar collectors due to the loss of heat to the surroundings, the reflection of light, and emissions as black bodies.[20,77] None of these inefficiencies are considered and the terms of equation 3-12 are each determined using an ideal energy and exergy balance. Opportunity for thermodynamic improvement is not available to this process in the design of the solar collector. Design considerations were seen to be able to have an effect on exergy losses within the solar collector. Feed temperature and recovery ratio both contributed to an

increase or decrease in exergy loss in the solar collector and these can be optimized with the other unit operations to achieve greater thermodynamic efficiencies.

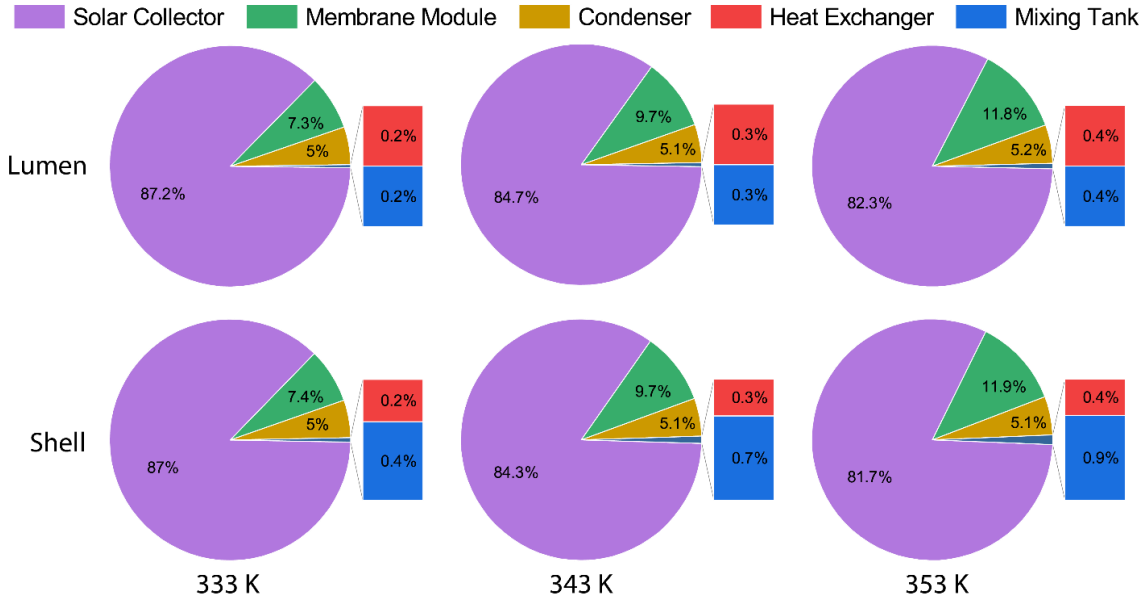

Figure 4-15: Unit operation contributions to exergy destruction. Inner radius 350 µm, thickness 300 µm, R/a 0.35, length 5 cm, feed velocity 1 m/s, vacuum pressure 5 kPa, tortuosity 2, pore diameter 400 nm, porosity 0.5, fiber length 5 cm.

4.2.3 Effect of Multiple Stages and Overall Recovery Ratio

The addition of multiple stages can have a significant effect on the performance of the system. Membrane modules can be placed in series to increase the single pass recovery ratio. Figure 4-16 shows the effect of the number of stages on the exergy efficiency of the process. In these calculations thermodynamic properties based on empirical data were used in lieu of the steam tables above.[94] As with the membrane parameters, the increase in heat loss that occurred as a result of the increase in single pass recovery ratio results in a reduction of exergy efficiency as the number of stages increass.

Again, similar to the effect of membrane parameters, this change is minimal. A more significant effect is observed by changing the overall recovery ratio of the process. Increasing the overall recovery ratio from 0.3 (a salt mass fraction of 0.05 in stream 7) to 0.86 (a salt mass fraction of 0.25 or nearly saturation within stream 7) results in a 0.7% increase in exergy efficiency. Increasing the single pass recovery ratio increases the mass flow rate of stream 9 as well as the temperature of stream 11. Increasing the flow rate of the permeate increases the amount of heat that must be absorbed by stream 11 to condense it. These increases lead to an increase in exergy efficiency by equation 3-9 despite the increase in Ex_{solar} required by the increased flow rate of streams 3 and 4.

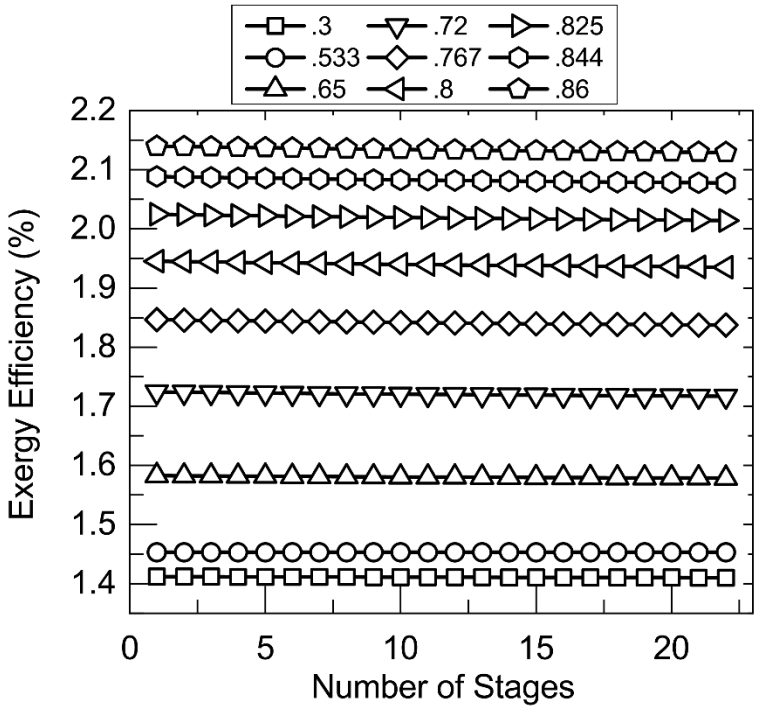

Figure 4-16: Exergy efficiency as a function of the number of stages placed in series. Legend indicates the overall recovery ratio for the process. Shell side feed. Inner radius 350 μm, thickness 300 μm, R/a 0.35, length 5 cm, feed velocity 1 m/s, vacuum pressure 5 kPa, tortuosity 2, pore diameter 400 nm, porosity 0.5, fiber length 5 cm.

4.3. Applied Context

In order to understand the feasibility of the solar-thermal VMD system it is helpful to examine the process for use in some real-world scenarios. One key aspect of consideration for any solar powered process is the size of the solar collector necessary. The size of the collector has a direct correlation to the land area required and can be indicative of capital cost. In a process like this, in which a hot fluid is transported throughout the solar field the area of that field is also important when considering heat loss. The area of solar collector required (relative to the freshwater production rate) can be calculated using equation 4-1.

$$A_{sf} = \frac{Q_{solar}}{Q_{sun} \cdot m_9} \quad (4\text{-}1)$$

Q_{sun} in equation 4-1 is the normal solar irradiance, estimated as 1360 W/m^2.[95] Figure 4-17 shows that the solar energy requirement, and therefore solar field area, are not intrinsically major functions of overall recovery ratio or single pass recovery ratio. Despite this, the small changes in the flow rate normalized solar field area yield significant changes when high values of water production are necessary. The required area increases as overall recovery ratio decreases because the mass flow rate of the recycle loops is reduced at lower overall recovery ratios. Because of this, the temperatures of these loops is reduced as they become more dependent on the temperature of the feed. It therefore requires more energy to raise the feed stream to the higher temperature, especially once values are normalized to mass flow rate of stream 9 which is also lowered by the reduction in recovery ratio. As single pass recovery ratio increases when more stages are added the area required is also decreased.

For specific contexts of application consider first the case of a family of four. An estimate based on the US National Academy of Medicine places the adequate daily fresh water intake of such a family at about 11 kg/day depending on the age and sex of the children.[96] If the process is considered to have an 8 hour operational day the solar collector required by the process would be about 0.75 m^2. Such a solar collector is reasonable in a suburban or rural context. This solar collector could easily fit on the roof of a house or in a back yard and leaves space to be scaled up to increase production. This is especially important for rural communities. A process could be developed to provide water for a group of families that does not require an extravagantly large solar collector.

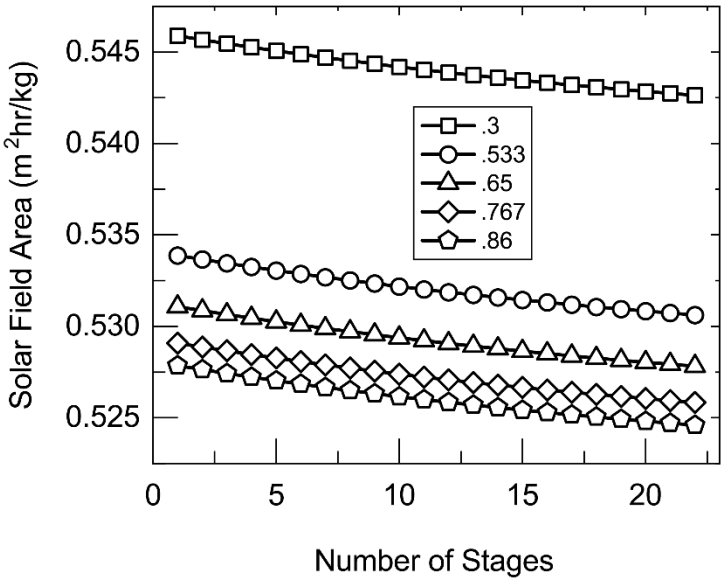

Figure 4-17: Solar field area required by the process per hourly rate of freshwater production. Legend indicates overall recovery ratio of the process. Shell side feed. Inner radius 350 μm, thickness 300 μm, R/a 0.35, length 5 cm, feed velocity 1 m/s, vacuum pressure 5 kPa, tortuosity 2, pore diameter 400 nm, porosity 0.5, fiber length 5 cm.

The city of Lincoln, Nebraska has a population of about 289,000 people.[97] Using the same recommended daily water intakes as above, the quantity of fresh drinking water needed by the city of Lincoln is about 875,000 kg/day. To achieve this daily water production a solar field of just under 15 acres would be required (not accounting for the lower solar irradiance present at this latitude). This area works out to about 82 MW of power (Q_{solar}). For context, a 230 MW solar farm has been proposed east of the city on over 1000 acres of land.[98] Excluding this proposed solar farm, a solar collector capable of producing the 82 MW necessary would be the largest solar power plant in the state of Nebraska.[98] Heat loss from the solar collector also becomes a greater concern at this scale as hot water would need to be pumped through this area to receive the energy required in this scheme. In the state of Nebraska plots with large acreages are not uncommon and so the land requirement would not be a major concern.

Singapore, with a population of 5.7 million people would require a solar collector of around 290 acres.[99] This area would likely be prohibitively large for the city state especially when it is considered that these calculations do not include the effect of heat loss within the process which would increase the needed area dramatically. A solar thermal VMD scheme may be more practicable as a means of augmenting other freshwater production methods, as is Singapore's intention.

The problems with VMD at this scale become more evident when a comparison is made to PV-RO. Because of the lower heat of separation, a PV-RO plant would be able to provide drinking water for Singapore using only 1.4 acres of PV cells (it is important to note that this is only drinking water, not the overall freshwater need of the city).[20,21,24] This is despite the lower energy recovery of these cells. For a city like

Singapore, with adequate infrastructure and the ability to operate and maintain such an array of PV cells, as well as the RO plant itself, the difference in area brought on by the energy requirement makes PV-RO the best option. It is then evident, based on the scale of solar collector necessary, that a solar thermal VMD process is most effective on the scale of a homestead or a village. On this scale it would also be easier to control heat loss from the solar collector and other unit operations.

An opportunity does remain for the solar thermal VMD process to improve via internal heat recovery. For VMD to become effective, and overcome the barrier to its implementation posed by the high latent heat of vaporization, a process must be able to recover that heat and reuse it to vaporize water again. GOR (gain to output ratio) is a descriptive value of the process that indicates how well heat provided for vaporization is being reused within the process.[20] The single pass process described herein has a GOR of about 1, indicating that the heat being absorbed is effectively being used to vaporize water but after vaporization that energy leaves the system and is not reused in any way. A GOR of 2 would indicate that the heat needed to separate 1 kg of water is effectively used to separate 2 kg. For this process to be within an order of magnitude of PV-RO in terms of energy requirement it would need to have a GOR of 29.

The most mature thermal technologies for desalination have achieved GOR values of about 15.[22] MD processes with advanced heat recovery systems achieve GOR values less than 10.[22] One reason for the lower value of GOR for MD is the scale of the process. High GOR values require high production.[22] Most MD processes that have looked into heat recovery have been limited in production to the pilot scale or production capable of supporting a few families.[81,100–103] For MD to become competitive it is

imperative that more work be done to improve the thermodynamic performance of the system.

CHAPTER 5

CONCLUSION AND FUTURE DIRECTIONS

A vacuum membrane distillation system was modelled in COMSOL Multiphysics® and used to perform an exergy analysis of a general solar thermal desalination process. The VMD module was seen to be able to achieve very high values of permeate flux. This performance was limited by the polarization phenomena prevalent in the system. The exergy analysis revealed very little relationship between membrane parameters, module design and overall exergy efficiency. It was seen that in all cases the solar collector provided the bulk of exergy lost due to irreversibility and provided for over 80 % of exergy lost in the process. Little can be done within the solar collector itself to improve its efficiency however process design was seen to have a significant effect on the magnitude of exergy lost within the solar collector.

Future work should focus on the reduction of exergy losses within the solar collector, or more exactly the optimization of exergy losses within the overall process, and the development of processes that can more effectively reuse the latent heat of vaporization at higher production levels. Further modelling and pilot scale plants can be effective in the optimization of solar thermal VMD. Modelling can greatly reduce the time and cost of optimization and consider a broad range of parameters that might affect the process. The above model can be readily optimized to maximize the exergy efficiency of the process across a range of flow rates, recovery ratios, temperatures, and membrane characteristics. Preliminary modelling and optimization in this way can provide direction to the next necessary step in improving the solar thermal VMD process which is the construction of real-world pilot scale processes.

Pilot scale experiments are important to determine the overall real-world behavior of the process. It was shown that the exergy efficiency of the various components within the VMD process were highly dependent on the overall design and performance of the system. While the behavior of the process as it relates to various inefficiencies within certain unit operations (e.g. heat loss in the buffer tank, radiative and convective losses in the solar collector, inefficiency of heat exchangers and condensers) can all be estimated in a numerical model, the complexity of process wide interactions, and the environmental considerations that also affect them, limit the value of these estimations. A pilot scale plant can allow these different environmental and operational effects to be taken into account. When coupled with a quality numeric model the pilot scale plant can be effectively optimized and provide valuable information for improvement of the solar thermal VMD processes as a whole.

Improving the GOR of the process is difficult. The best GOR values have been achieved by processes that are very mature in their technology and large in their scale.[20,22] At present VMD meets neither of these qualifications. The construction of more pilot scale plants can aid in expediting this process as more information is gathered on the tradeoffs of various heat recovery methods.

In addition to the improvements that can be investigated at the pilot scale work ought to focus also on the efficient condensation of water vapor. To this end, work that is being done to increase the performance of the membranes can be useful. Increasing the hydrophobicity of membranes has been one of the chief means of reducing scaling.[22] Increasing the hydrophobicity of condensing surfaces is key to improving the efficiency of condensation. Hydrophobic materials that can prevent the formation of inefficient

condensing films while having little effect on the conductive properties of the surface can greatly improve the recovery of the latent heat of vaporization.[104]

More generally the principles of process intensification provide great opportunity for the improvement of the solar thermal VMD processes. Indeed, many of the directions discussed above fall under this umbrella. Every area of the process includes potential for intensification. Van Gerven and Stankiewicz identify four general principles for (chemical) process intensification [105]:

- Maximize the effectiveness of intra- and intermolecular events
- Give each molecule the same processing experience
- Optimize the driving forces at every scale and maximize the specific surface area to which these forces apply
- Maximize the synergistic effects from partial processes

The first two principles are the most difficult to apply to VMD processes as chemical conversions are neither required nor desired. The second two principles however have very broad applications to VMD and provide many opportunities for engineers to creatively apply their trade. The third principle can be readily applied in the solar collector, membrane module, condenser, and heat transfer units. Efficient and rapid heating and separation at minimum process volume is extremely desirable. As shown above, the scale of the solar collector necessary is significant in this process. This principle provides a valuable guide towards maximizing the efficiency of the heating process.

Application of the fourth principle has been a major focus of research over the past few years. Processes that combine solar collectors, membranes, condensers, and heat

recovery units into a single module have been described.[20,77] These types of processes likely provide the best opportunity to overcome the challenges inherent in the VMD system. Improvement of GOR via internal heat recovery is a great example of this principle in action. While the current practical limit to internal heat recovery in MD is a GOR of less than 10, GOR values as high as 84 have been described theoretically.[22] The greatest limit in achieving such a value is the efficiency of current heat recovery materials and systems.[22] Novel heat transfer units, such as heat pipes, may provide a means of overcoming these challenges.[106] VMD as a process is relatively young and very few technologies have been specifically investigated to improve its performance. Many areas remain to be explored in the intensification of the VMD process and only a few have been touched on here.

Despite the improvements that can be achieved in the process, a thermodynamic limit will exist. Membrane distillation processes are, at their core, heat engines, and as such are limited by Carnot's theorem.[71] No amount of heat recovery will be able to overcome this inefficiency. Other limitations are not so absolute. The high latent heat of vaporization may be recovered and reused effectively, and other energy losses in the process can be controlled. Despite this a wide technological gap must be bridged before Carnot's efficiency can be approached. Current limitations in heat recovery are the most significant and these should remain the primary focus of future research. These improvements will be especially valuable in reducing the scale of the solar collector which was shown to be, thermodynamically, the least efficient operation in the process.

In all of these improvements it is important to keep the context of a particular application in view. The complexity added by an effective heat recovery scheme, or the

added up front cost of reducing heat loss can be detrimental to the value of solar thermal VMD in those applications in which it is currently most effective. As we move towards more sustainable means of water generation it is important to balance the different requirements of a process. VMD is a process that can be readily converted to make use of renewable forms of energy. Despite this the extremely low energy efficiency of the process has made it unattractive compared to other technologies such as reverse osmosis. If VMD is to become competitive as a means of desalination work must be done to optimize process designs and minimize the many inherent inefficiencies present in the process. It also becomes important to measure these inefficiencies against the cost of the process and the unique situations in which it is to be implemented.

REFERENCES

(1) Kummu, M. The World's Road to Water Scarcity: Shortage and Stress in the 20th Century and Pathways towards Sustainability. *Sci. Rep.* 16.

(2) International Decade for Action "Water for Life" 2005-2015. Focus Areas: Water scarcity https://www.un.org/waterforlifedecade/scarcity.shtml (accessed 2021 -06 -15).

(3) Ng, P. J. H.; Teo, C. Singapore's Water Challenges Past to Present. *Int. J. Water Resour. Dev.* **2020**, *36* (2–3), 269–277. https://doi.org/10.1080/07900627.2019.1680350.

(4) Chuah, C. J.; Ho, B. H.; Chow, W. T. L. Trans-Boundary Variations of Urban Drought Vulnerability and Its Impact on Water Resource Management in Singapore and Johor, Malaysia. *Environ. Res. Lett.* **2018**, *13* (7), 074011. https://doi.org/10.1088/1748-9326/aacad8.

(5) Lafforgue, M.; Lenouvel, V. Closing the Urban Water Loop: Lessons from Singapore and Windhoek. *Environ. Sci. Water Res. Technol.* **2015**, *1* (5), 622–631. https://doi.org/10.1039/C5EW00056D.

(6) Hsien, C.; Choong Low, J. S.; Chan Fuchen, S.; Han, T. W. Life Cycle Assessment of Water Supply in Singapore — A Water-Scarce Urban City with Multiple Water Sources. *Resour. Conserv. Recycl.* **2019**, *151*, 104476. https://doi.org/10.1016/j.resconrec.2019.104476.

(7) Abdullah, Z. 4 firms vie to build and operate Singapore's fifth desalination plant https://www.straitstimes.com/singapore/four-firms-vie-to-build-and-operate-singapores-fifth-desalination-plant (accessed 2021 -06 -15).

(8) Tortajada, C.; Nambiar, S. Communications on Technological Innovations: Potable Water Reuse. *Water* **2019**, *11* (2), 251. https://doi.org/10.3390/w11020251.

(9) Ghaffour, N.; Bundschuh, J.; Mahmoudi, H.; Goosen, M. F. A. Renewable Energy-Driven Desalination Technologies: A Comprehensive Review on Challenges and Potential Applications of Integrated Systems. *Desalination* **2015**, *356*, 94–114. https://doi.org/10.1016/j.desal.2014.10.024.

(10) El-Nashar, A. M.; Samad, M. The Solar Desalination Plant in Abu Dhabi: 13 Years of Performance and Operation History. *Renew. Energy* **1998**, *14* (1–4), 263–274. https://doi.org/10.1016/S0960-1481(98)00076-7.

(11) Gorjian, S.; Ghobadian, B. Solar Desalination: A Sustainable Solution to Water Crisis in Iran. *Renew. Sustain. Energy Rev.* **2015**, *48*, 571–584. https://doi.org/10.1016/j.rser.2015.04.009.

(12) Ibrahim, H. D.; Eltahir, E. A. B. Impact of Brine Discharge from Seawater Desalination Plants on Persian/Arabian Gulf Salinity. *J. Environ. Eng.* **2019**, *145* (12), 04019084. https://doi.org/10.1061/(ASCE)EE.1943-7870.0001604.

(13) Campos, E. J. D.; Vieira, F.; Cavalcante, G.; Kjerfve, B.; Abouleish, M.; Shahriar, S.; Mohamed, R.; Gordon, A. L. Impacts of Brine Disposal from Water Desalination Plants on the Physical Environment in the Persian/Arabian Gulf. *Environ. Res. Commun.* **2020**, *2* (12), 125003. https://doi.org/10.1088/2515-7620/abd0ed.

(14) Hillie, T.; Hlophe, M. Nanotechnology and the Challenge of Clean Water. *Nat. Nanotechnol.* **2007**, *2* (11), 663–664. https://doi.org/10.1038/nnano.2007.350.
(15) He, S.; Chen, C.; Kuang, Y.; Mi, R.; Liu, Y.; Pei, Y.; Kong, W.; Gan, W.; Xie, H.; Hitz, E.; Jia, C.; Chen, X.; Gong, A.; Liao, J.; Li, J.; Ren, Z. J.; Yang, B.; Das, S.; Hu, L. Nature-Inspired Salt Resistant Bimodal Porous Solar Evaporator for Efficient and Stable Water Desalination. *Energy Environ. Sci.* **2019**, *12* (5), 1558–1567. https://doi.org/10.1039/C9EE00945K.
(16) Li, C.; Goswami, Y.; Stefanakos, E. Solar Assisted Sea Water Desalination: A Review. *Renew. Sustain. Energy Rev.* **2013**, *19*, 136–163. https://doi.org/10.1016/j.rser.2012.04.059.
(17) Shatat, M.; Worall, M.; Riffat, S. Opportunities for Solar Water Desalination Worldwide: Review. *Sustain. Cities Soc.* **2013**, *9*, 67–80. https://doi.org/10.1016/j.scs.2013.03.004.
(18) Sharon, H.; Reddy, K. S. A Review of Solar Energy Driven Desalination Technologies. *Renew. Sustain. Energy Rev.* **2015**, *41*, 1080–1118. https://doi.org/10.1016/j.rser.2014.09.002.
(19) Aboelmaaref, M. M.; Zayed, M. E.; Zhao, J.; Li, W.; Askalany, A. A.; Ahmed, M. S.; Ehab, S. A. Hybrid Solar Desalination Systems Driven by Parabolic Trough and Parabolic Dish CSP Technologies_ Technology Categorization, Thermodynamic Performance and Economical Assessment. *Energy Convers. Manag.* **2020**, *220*, 33.
(20) Wang, Z.; Horseman, T.; Straub, A. P.; Yip, N. Y.; Li, D.; Elimelech, M.; Lin, S. Pathways and Challenges for Efficient Solar-Thermal Desalination. *Sci. Adv.* **2019**, *5* (7), eaax0763. https://doi.org/10.1126/sciadv.aax0763.
(21) Qasim, M.; Badrelzaman, M.; Darwish, N. N.; Darwish, N. A.; Hilal, N. Reverse Osmosis Desalination: A State-of-the-Art Review. *Desalination* **2019**, *459*, 59–104. https://doi.org/10.1016/j.desal.2019.02.008.
(22) Deshmukh, A.; Boo, C.; Karanikola, V.; Lin, S.; Straub, A. P.; Tong, T.; Warsinger, D. M.; Elimelech, M. Membrane Distillation at the Water-Energy Nexus: Limits, Opportunities, and Challenges. *Energy Environ. Sci.* **2018**, *11* (5), 1177–1196. https://doi.org/10.1039/C8EE00291F.
(23) Peñate, B.; García-Rodríguez, L. Current Trends and Future Prospects in the Design of Seawater Reverse Osmosisdesalination Technology. *Desalination* **2012**, *284*, 1–8. https://doi.org/10.1016/j.desal.2011.09.010.
(24) Nayak, P. K.; Mahesh, S.; Snaith, H. J.; Cahen, D. Photovoltaic Solar Cell Technologies: Analysing the State of the Art. *Nat. Rev. Mater.* **2019**, *4* (4), 269–285. https://doi.org/10.1038/s41578-019-0097-0.
(25) Rezk, H.; Sayed, E. T.; Al-Dhaifallah, M.; Obaid, M.; El-Sayed, A. H. M.; Abdelkareem, M. A.; Olabi, A. G. Fuel Cell as an Effective Energy Storage in Reverse Osmosis Desalination Plant Powered by Photovoltaic System. *Energy* **2019**, *175*, 423–433. https://doi.org/10.1016/j.energy.2019.02.167.
(26) Rabaia, M. K. H.; Abdelkareem, M. A.; Sayed, E. T.; Elsaid, K.; Chae, K.-J.; Wilberforce, T.; Olabi, A. G. Environmental Impacts of Solar Energy Systems: A Review. *Sci. Total Environ.* **2021**, *754*, 141989. https://doi.org/10.1016/j.scitotenv.2020.141989.

(27) Revertera, J. A. Las Palmas III the Success Story of Brine Staging. *Desalination* **2001**, *138* (1–3), 207–217. https://doi.org/10.1016/S0011-9164(01)00266-1.
(28) Magara, Y.; Kawasaki, M.; Sekino, M.; Yamamura, H. Development of Reverse Osmosis Membrane Seawater Desalination in Japan. *Water Sci. Technol.* **2000**, *41* (10–11), 1–8. https://doi.org/10.2166/wst.2000.0594.
(29) Chen, S.; Zhao, P.; Xie, G.; Wei, Y.; Lyu, Y.; Zhang, Y.; Yan, T.; Zhang, T. A Floating Solar Still Inspired by Continuous Root Water Intake. *Desalination* **2021**, *512*, 115133. https://doi.org/10.1016/j.desal.2021.115133.
(30) Wang, P.; Chung, T.-S. Recent Advances in Membrane Distillation Processes: Membrane Development, Configuration Design and Application Exploring. *J. Membr. Sci.* **2015**, *474*, 39–56. https://doi.org/10.1016/j.memsci.2014.09.016.
(31) Callahan, S. *Adrift: Seventy-Six Days Lost at Sea*; Mariner Books: Boston, MA, 2002.
(32) Khayet, M. Membranes and Theoretical Modeling of Membrane Distillation: A Review. *Adv. Colloid Interface Sci.* **2011**, *164* (1–2), 56–88. https://doi.org/10.1016/j.cis.2010.09.005.
(33) Camacho, L.; Dumée, L.; Zhang, J.; Li, J.; Duke, M.; Gomez, J.; Gray, S. Advances in Membrane Distillation for Water Desalination and Purification Applications. *Water* **2013**, *5* (1), 94–196. https://doi.org/10.3390/w5010094.
(34) Drioli, E.; Ali, A.; Macedonio, F. Membrane Distillation: Recent Developments and Perspectives. *Desalination* **2015**, *356*, 56–84. https://doi.org/10.1016/j.desal.2014.10.028.
(35) Lawson, K. W.; Lloyd, D. R. Membrane Distillation. *J. Membr. Sci.* **2997**, *124*, 1–25.
(36) Schofield, R. W. Membrane Distillation. Doctor of Philosophy Thesis, Univeristy of New South Wales, Sydney, AU, 1989.
(37) Abu-Zeid, M. A. E.-R.; Zhang, Y.; Dong, H.; Zhang, L.; Chen, H.-L.; Hou, L. A Comprehensive Review of Vacuum Membrane Distillation Technique. *Desalination* **2015**, *356*, 1–14. https://doi.org/10.1016/j.desal.2014.10.033.
(38) Zhou, L.; Tan, Y.; Ji, D.; Zhu, B.; Zhang, P.; Xu, J.; Gan, Q.; Yu, Z.; Zhu, J. Self-Assembly of Highly Efficient, Broadband Plasmonic Absorbers for Solar Steam Generation. *Sci. Adv.* **2016**, *2* (4), e1501227. https://doi.org/10.1126/sciadv.1501227.
(39) Chiavazzo, E.; Morciano, M.; Viglino, F.; Fasano, M. Passive High-Yield Seawater Desalination at below One Sun by Modular and Low-Cost Distillation. *Nat. Sustain.* **2018**, *1*, 763–772.
(40) Morciano, M.; Fasano, M.; Bergamasco, L.; Albiero, A.; Lo Curzio, M.; Asinari, P.; Chiavazzo, E. Sustainable Freshwater Production Using Passive Membrane Distillation and Waste Heat Recovery from Portable Generator Sets. *Appl. Energy* **2020**, *258*, 114086. https://doi.org/10.1016/j.apenergy.2019.114086.
(41) Tanvir, R. U.; Sujon, S. A.; Yi, P. Passive Permeate-Side-Heated Solar Thermal Membrane Distillation: Extracting Potable Water from Seawater, Surface Water, and Municipal Wastewater at High Single-Stage Solar Efficiencies. *ACS EST Eng.* **2021**, *1* (4), 770–779. https://doi.org/10.1021/acsestengg.0c00260.

(42) Tong, T.; Elimelech, M. The Global Rise of Zero Liquid Discharge for Wastewater Management: Drivers, Technologies, and Future Directions. *Env. Sci Technol* **2016**, *50* (13), 6846–6855. https://doi.org/10.1021/acs.est.6b01000.

(43) Ruiz Salmón, I.; Luis, P. Membrane Crystallization via Membrane Distillation. *Chem. Eng. Process. - Process Intensif.* **2018**, *123*, 258–271. https://doi.org/10.1016/j.cep.2017.11.017.

(44) Imdakm, A. O.; Khayet, M.; Matsuura, T. A Monte Carlo Simulation Model for Vacuum Membrane Distillation Process. *J. Membr. Sci.* **2007**, *306* (1–2), 341–348. https://doi.org/10.1016/j.memsci.2007.09.021.

(45) Bandini, S.; Saavedra, A.; Sarti, G. C. Vacuum Membrane Distillation: Experiments and Modeling. *AIChE J.* **1997**, *43* (2), 398–408. https://doi.org/10.1002/aic.690430213.

(46) Khayet, M.; Matsuura, T. Pervaporation and Vacuum Membrane Distillation Processes: Modeling and Experiments. *AIChE J.* **2004**, *50* (8), 1697–1712. https://doi.org/10.1002/aic.10161.

(47) Chen, L.; Wu, B. Research Progress in Computational Fluid Dynamics Simulations of Membrane Distillation Processes: A Review. *Membranes* **2021**, *11* (7), 513. https://doi.org/10.3390/membranes11070513.

(48) Tang, N.; Zhang, H.; Wang, W. Computational Fluid Dynamics Numerical Simulation of Vacuum Membrane Distillation for Aqueous NaCl Solution. *Desalination* **2011**, *274* (1–3), 120–129. https://doi.org/10.1016/j.desal.2011.01.078.

(49) Upadhyaya, S.; Singh, K.; Chaurasia, S. P.; Dohare, R. K.; Agarwal, M. Mathematical and CFD Modeling of Vacuum Membrane Distillation for Desalination. *Desalination Water Treat.* **2016**, *57* (26), 11956–11971. https://doi.org/10.1080/19443994.2015.1048306.

(50) Zhang, Y.; Peng, Y.; Ji, S.; Wang, S. Numerical Simulation of 3D Hollow-Fiber Vacuum Membrane Distillation by Computational Fluid Dynamics. *Chem. Eng. Sci.* **2016**, *152*, 172–185. https://doi.org/10.1016/j.ces.2016.05.040.

(51) Zhang, J.; Li, J.-D.; Duke, M.; Hoang, M.; Xie, Z.; Groth, A.; Tun, C.; Gray, S. Modelling of Vacuum Membrane Distillation. *J. Membr. Sci.* **2013**, *434*, 1–9. https://doi.org/10.1016/j.memsci.2013.01.048.

(52) Lian, B.; Wang, Y.; Le-Clech, P.; Chen, V.; Leslie, G. A Numerical Approach to Module Design for Crossflow Vacuum Membrane Distillation Systems. *J. Membr. Sci.* **2016**, *510*, 489–496. https://doi.org/10.1016/j.memsci.2016.03.041.

(53) Omar, A.; Li, Q.; Nashed, A.; Guan, J.; Dai, P.; Taylor, R. A. Experimental and Numerical Investigation of a New Hollow Fiber-Based Multi-Effect Vacuum Membrane Distillation Design. *Desalination* **2021**, *501*, 114908. https://doi.org/10.1016/j.desal.2020.114908.

(54) Zrelli, A.; Chaouachi, B. MODELING AND SIMULATION OF A VACUUM MEMBRANE DISTILLATION PLANT COUPLED WITH SOLAR ENERGY AND USING HELICAL HOLLOW FIBERS. *Braz. J. Chem. Eng.* **2019**, *36* (3), 1119–1129. https://doi.org/10.1590/0104-6632.20190363s20180531.

(55) Chamani, H.; Matsuura, T.; Rana, D.; Lan, C. Q. Modeling of Pore Wetting in Vacuum Membrane Distillation. *J. Membr. Sci.* **2019**, *572*, 332–342. https://doi.org/10.1016/j.memsci.2018.11.018.

(56) Rezaei, M.; Warsinger, D. M.; Lienhard V, J. H.; Duke, M. C.; Matsuura, T.; Samhaber, W. M. Wetting Phenomena in Membrane Distillation: Mechanisms, Reversal, and Prevention. *Water Res.* **2018**, *139*, 329–352. https://doi.org/10.1016/j.watres.2018.03.058.

(57) Liu, J.; Wang, Q.; Shan, H.; Guo, H.; Li, B. Surface Hydrophobicity Based Heat and Mass Transfer Mechanism in Membrane Distillation. *J. Membr. Sci.* **2019**, *580*, 275–288. https://doi.org/10.1016/j.memsci.2019.01.057.

(58) Liu, J.; Li, X.; Zhang, W.; Li, B.; Liu, C. Superhydrophobic-Slip Surface Based Heat and Mass Transfer Mechanism in Vacuum Membrane Distillation. *J. Membr. Sci.* **2020**, *614*, 118505. https://doi.org/10.1016/j.memsci.2020.118505.

(59) Mittal, S.; Gupta, A.; Srivastava, S.; Jain, M. Artificial Neural Network Based Modeling of the Vacuum Membrane Distillation Process: Effects of Operating Parameters on Membrane Fouling. *Chem. Eng. Process. - Process Intensif.* **2021**, *164*, 108403. https://doi.org/10.1016/j.cep.2021.108403.

(60) Mohammadi Ghaleni, M.; Bavarian, M.; Nejati, S. Model-Guided Design of High-Performance Membrane Distillation Modules for Water Desalination. *J. Membr. Sci.* **2018**, *563*, 794–803. https://doi.org/10.1016/j.memsci.2018.06.054.

(61) Alklaibi, A. M.; Lior, N. Membrane-Distillation Desalination: Status and Potential. *Desalination* **2005**, *171* (2), 111–131. https://doi.org/10.1016/j.desal.2004.03.024.

(62) Alkhudhiri, A.; Darwish, N.; Hilal, N. Membrane Distillation: A Comprehensive Review. *Desalination* **2012**, *287*, 2–18. https://doi.org/10.1016/j.desal.2011.08.027.

(63) Wilkes, J. O. *Fluid Mechanics for Chemical Engineers with Microfluidics and CFD*, 2nd ed.; Pearson Education, INC: Upper Saddle River, NJ, USA, 2006.

(64) Bird, R. B.; Stewart, W. E.; Lightfoot, E. N. *Transport Phenomena*; John Wiley & Sons: Hoboken, NJ, USA, 1960.

(65) Pinho, S. P.; Macedo, E. A. Solubility of NaCl, NaBr, and KCl in Water, Methanol, Ethanol, and Their Mixed Solvents. *J. Chem. Eng. Data* **2005**, *50* (1), 29–32. https://doi.org/10.1021/je049922y.

(66) *Chemical Reaction Engineering Module User's Guide, COMSOL Multiphysics® v. 5.4*; COMSOL AB: Stockholm, Sweden, 2018.

(67) Millero, F. J.; Feistel, R.; Wright, D. G.; McDougall, T. J. The Composition of Standard Seawater and the Definition of the Reference-Composition Salinity Scale. *Deep Sea Res. Part Oceanogr. Res. Pap.* **2008**, *55* (1), 50–72. https://doi.org/10.1016/j.dsr.2007.10.001.

(68) Vitagliano, V.; Lyons, P. A. Diffusion Coefficients for Aqueous Solutions of Sodium Chloride and Barium Chloride. *J. Am. Chem. Soc.* **1956**, *78* (8), 1549–1552. https://doi.org/10.1021/ja01589a011.

(69) Welty, J.; Gregory, R.; David, F. *Fundamentals of Momentum, Heat, and Mass Transfer*, 6th ed.; Wiley: Hoboken, NJ, USA, 2015.

(70) Demirel, Y. *Nonequilibrium Thermodynamics*, 2nd ed.; Elsevier B.V.: Amterdam, NL, 2007.

(71) Smith, J. M.; Van Ness, H. C.; Abbot, M. M. *Introduction to Chemical Engineering Thermodynamics*, 7th ed.; McGraw-Hill: New York, NY, 2005.

(72) Minier-Matar, J.; Hussain, A.; Janson, A.; Benyahia, F.; Adham, S. Field Evaluation of Membrane Distillation Technologies for Desalination of Highly

Saline Brines. *Desalination* **2014**, *351*, 101–108. https://doi.org/10.1016/j.desal.2014.07.027.

(73) *Kirk-Othmer Encyclopedia of Chemical Technology*, 5th ed.; John Wiley & Sons: Hoboken, NJ, USA, 2004; Vol. 13.

(74) Holmgren, M. X Steam, Thermodynamic properties of water and steam. https://www.mathworks.com/matlabcentral/fileexchange/9817-x-steam-thermodynamic-properties-of-water-and-steam (accessed 2021 -04 -16).

(75) Nayar, K. G.; Sharqawy, M. H.; Banchik, L. D. Thermophysical Properties of Seawater: A Review and New Correlations That Include Pressure Dependence. *Desalination* **2016**, *390*, 1–24. https://doi.org/10.1016/j.desal.2016.02.024.

(76) Sharqawy, M. H.; Lienhard, J. H.; Zubair, S. M. Thermophysical Properties of Seawater: A Review of Existing Correlations and Data. *Desalination Water Treat.* **2010**, *16* (1–3), 354–380. https://doi.org/10.5004/dwt.2010.1079.

(77) Signorato, F.; Morciano, M.; Bergamasco, L.; Fasano, M.; Asinari, P. Exergy Analysis of Solar Desalination Systems Based on Passive Multi-Effect Membrane Distillation. *Energy Rep.* **2020**, *6*, 445–454. https://doi.org/10.1016/j.egyr.2020.02.005.

(78) Pal, R. Chemical Exergy of Ideal and Non-Ideal Gas Mixtures and Liquid Solutions with Applications. *Int. J. Mech. Eng. Educ.* **2019**, *47* (1), 44–72. https://doi.org/10.1177/0306419017749581.

(79) Lienhard, J. H.; Mistry, K. H.; Sharqawy, M. H.; Thiel, G. P. Thermodynamics, Exergy, and Energy Efficiency in Desalination Systems. In *Desalination Sustainability*; Elsevier, 2017; pp 127–206. https://doi.org/10.1016/B978-0-12-809791-5.00004-3.

(80) Leonard, M. D.; Michaelides, E. E.; Michaelides, D. N. Energy Storage Needs for the Substitution of Fossil Fuel Power Plants with Renewables. *Renew. Energy* **2020**, *145*, 951–962. https://doi.org/10.1016/j.renene.2019.06.066.

(81) Andrés-Mañas, J. A.; Roca, L.; Ruiz-Aguirre, A.; Acién, F. G.; Gil, J. D.; Zaragoza, G. Application of Solar Energy to Seawater Desalination in a Pilot System Based on Vacuum Multi-Effect Membrane Distillation. *Appl. Energy* **2020**, *258*, 114068. https://doi.org/10.1016/j.apenergy.2019.114068.

(82) Peters, M. S.; Timmerhaus, K. D.; West, R. E. *Plant Design and Economics for Chemical Engineers*, 5th ed.; McGraw-Hill chemical engineering series; McGraw-Hill: New York, 2003.

(83) Wang, Y.; Xu, Z.; Lior, N.; Zeng, H. An Experimental Study of Solar Thermal Vacuum Membrane Distillation Desalination. *Desalination Water Treat.* **2014**, 1–11. https://doi.org/10.1080/19443994.2014.927187.

(84) El Kadi, K.; Janajreh, I.; Hashaikeh, R. Numerical Simulation and Evaluation of Spacer-Filled Direct Contact Membrane Distillation Module. *Appl. Water Sci.* **2020**, *10* (7), 174. https://doi.org/10.1007/s13201-020-01261-9.

(85) Chang, Y. S.; Ooi, B. S.; Ahmad, A. L.; Leo, C. P.; Low, S. C. Vacuum Membrane Distillation for Desalination: Scaling Phenomena of Brackish Water at Elevated Temperature. *Sep. Purif. Technol.* **2021**, *254*, 117572. https://doi.org/10.1016/j.seppur.2020.117572.

(86) Tijing, L. D.; Woo, Y. C.; Choi, J.-S.; Lee, S.; Kim, S.-H.; Shon, H. K. Fouling and Its Control in Membrane Distillation—A Review. *J. Membr. Sci.* **2015**, *475*, 215–244. https://doi.org/10.1016/j.memsci.2014.09.042.

(87) Alkhudhiri, A.; Hilal, N. *Membrane Distillation—Principles, Applications, Configurations, Design, and Implementation. In Emerging Technologies for Sustainable Desalination Handbook*; Gude, V. G., Ed.; Butterworth-Heinemann: Oxford, UK, 2008.

(88) Lalia, B. S.; Kochkodan, V.; Hashaikeh, R.; Hilal, N. A Review on Membrane Fabrication: Structure, Properties and Performance Relationship. *Desalination* **2013**, *326*, 77–95. https://doi.org/10.1016/j.desal.2013.06.016.

(89) Blumm, J.; Lindemann, A. Characterization of the Thermophysical Properties of Molten Plymers and Liquids Using the Flash Technique. *High Temp.-High Press.* **2003**, *35/36* (6), 627–632. https://doi.org/10.1068/htjr144.

(90) Warsinger, D. M.; Swaminathan, J.; Guillen-Burrieza, E.; Arafat, H. A.; Lienhard V, J. H. Scaling and Fouling in Membrane Distillation for Desalination Applications: A Review. *Desalination* **2015**, *356*, 294–313. https://doi.org/10.1016/j.desal.2014.06.031.

(91) Lou, Y.; Gogar, R.; Hao, P.; Lipscomb, G.; Amo, K.; Kniep, J. Simulation of Net Spacers in Membrane Modules for Carbon Dioxide Capture. *Sep. Sci. Technol. 52* (2), 168–185. https://doi.org/10.1080/01496395.2016.1220396.

(92) Phattaranawik, J.; Jiraratananon, R.; Fane, A. G. Heat Transport and Membrane Distillation Coefficients in Direct Contact Membrane Distillation. *J. Membr. Sci.* **2003**, *212* (1–2), 177–193. https://doi.org/10.1016/S0376-7388(02)00498-2.

(93) *CFD Module User's Guide, COMSOL Multiphysics® v. 5.4*; COMSOL AB: Stockholm, Sweden, 2018.

(94) Chou, J. C.-S. THERMODYNAMIC PROPERTIES OF AQUEOUS SODIUM CHLORIDE SOLUTIONS FROM 32 TO 350°F. 129.

(95) Kopp, G.; Lean, J. L. A New, Lower Value of Total Solar Irradiance: Evidence and Climate Significance: FRONTIER. *Geophys. Res. Lett.* **2011**, *38* (1), n/a-n/a. https://doi.org/10.1029/2010GL045777.

(96) Armstrong, L. E.; Johnson, E. C. Water Intake, Water Balance, and the Elusive Daily Water Requirement. *Nutrients* **2018**, *10* (12), 1928. https://doi.org/10.3390/nu10121928.

(97) U.S. Census Bureau QuickFacts: Lincoln city, Nebraska https://www.census.gov/quickfacts/lincolncitynebraska (accessed 2021 -06 -29).

(98) State's largest solar project planned east of Lincoln | Local Business News | journalstar.com https://journalstar.com/business/local/states-largest-solar-project-planned-east-of-lincoln/article_e9bdeb72-944e-5cda-96e4-3b022d54a0e1.html (accessed 2021 -07 -02).

(99) Population and Population Structure - Latest Data http://www.singstat.gov.sg/find-data/search-by-theme/population/population-and-population-structure/latest-data (accessed 2021 -06 -29).

(100) Burhan, M.; Shahzad, M. W.; Ybyraiymkul, D.; Oh, S. J.; Ghaffour, N.; Ng, K. C. Performance Investigation of MEMSYS Vacuum Membrane Distillation System in Single Effect and Multi-Effect Mode. *Sustain. Energy Technol. Assess.* **2019**, *34*, 9–15. https://doi.org/10.1016/j.seta.2019.04.003.

(101) Alquraish, M. M.; Mejbri, S.; Abuhasel, K. A.; Zhani, K. Experimental Investigation of a Pilot Solar-Assisted Permeate Gap Membrane Distillation. *Membranes* **2021**, *11* (5), 336. https://doi.org/10.3390/membranes11050336.
(102) El-Zanati, E.; El-Zanati, M.; Khedr, M.; Farg, E.; Taha, E. Development of Vacuum Multi-Effect Membrane Distillation System of Pilot-Scale for Water Desalination. *DESALINATION WATER Treat.* **2021**, *217*, 22–30. https://doi.org/10.5004/dwt.2021.26820.
(103) Najib, A.; Orfi, J.; Alansary, H.; Ali, E. Assessing the Impact of Operating Conditions on the Energy and Exergy Efficiency for Multi-Effect Vacuum Membrane Distillation Systems. *Water* **2021**, *13* (11), 1500. https://doi.org/10.3390/w13111500.
(104) El Fil, B.; Kini, G.; Garimella, S. A Review of Dropwise Condensation: Theory, Modeling, Experiments, and Applications. *Int. J. Heat Mass Transf.* **2020**, *160*, 120172. https://doi.org/10.1016/j.ijheatmasstransfer.2020.120172.
(105) Van Gerven, T.; Stankiewicz, A. Structure, Energy, Synergy, Time—The Fundamentals of Process Intensification. *Ind. Eng. Chem. Res.* **2009**, *48* (5), 2465–2474. https://doi.org/10.1021/ie801501y.
(106) Qu, J.; Guan, F.; Lv, Y.; Wang, Y. Experimental Study on the Heat Transport Capability of Micro-Grooved Oscillating Heat Pipe. *Case Stud. Therm. Eng.* **2021**, *26*, 101210. https://doi.org/10.1016/j.csite.2021.101210.

APPENDIX

Table A-1: Modelling Parameters as Defined in COMSOL Multiphysics®

R_i	.35 [mm]	Inner Radius
delta_m	.3 [mm]	Membrane Thickness
R_a	0.35	fiber spacing ratio
L_m	.05 [m]	length
u_p	1 [m/s]	feed inlet velocity
P_amb	1 [atm]	ambient pressure
P_ref	0 [atm]	reference pressure
T_f	343 [K]	Feed Temperature
k_pol	0.6 [W/(m*K)]	Thermal Conductivity of Polymer
rho_pol	1780	Density of the Polymer
Cp_pol	1120 [J/(kg*K)]	Heat Capacity of Polymer
k_perm	1E-15 [m^2]	Permeability of Membrane
Psatconst	exp((AA-(BB/(T_f/1[K]+CC)))) [Pa]	Saturation Pressure at Constant Temperature
AA	23.352	Antoine's Constant A
BB	3984.85	Antoine's Constant B
CC	-39.724	Antoine's Constant C
P_out	5 [kPa]	Outlet Pressure
rho_steam	P_out*M_w/R_const/T_f	Density of Steam
M_w	18.01 [g/mol]	Molar Mass of Water
H_vap	40 [kJ/mol]	Heat of Vaporization
mu_steam	.011*10^(-3) [Pa*s]	Viscosity of Steam
T_p	293.25 [K]	Permeate Temperature
Cp_steam	1.996 [kJ/kg/K]	Heat Capacity of Steam
eps_mem	0.5	porosity of the membrane
M_a	28.97 [g/mol]	Molar Mass of Air
tau_mem	2	Membrane Tortuosity
d_pore	.4 [um]	Mean pore diameter
M_s	58.44 [g/mol]	Molar Mass of Salt

Table A-2: Variables as Defined in COMSOL Multiphysics®

Psatfinal	a_w*exp((AA-(BB/(T/1[K]+CC))))[Pa]	Saturation Pressure of Steam
D_kn	(4/3)*d_pore*M_u	Knudsen diffusion coefficient
D_m_mem	((b_mem)*(1.895*10^-5))[(m*kg)/(s^3)]/P_out	Molecular Diffusion Coefficient Membrane
D_t	(e_t)*(1/(((1-y_vap)/D_m_mem)+(1/D_kn)))	Total Diffusion Coefficient
M_u	sqrt((R_const*T2)/(2*3.14*M_w))	Mean Molecular Velocity
b_mem	(((T2)/1[K])^2.072)	Molecular Diffusion Coefficient Temperature Component Membrane
D_m_l	((b_l)*(1.895*10^-5))[(m*kg)/(s^3)]/P_out	Molecular Diffusion Coefficient Lumen
b_l	(((T3)/1[K])^2.072)	Molecular Diffusion Coefficient Temperature Component Membrane
y_vap	1-eps	Mole Fraction Water Vapor
C_perm_v	C_1_v+C_2_v	Combined Knudsen-Poiseuille diffusion coefficient
C_1_v	8*(d_pore/2)*(eps_mem)*((1/(2*pi*R_const*M_w*T_f))^(1/2))/(3*delta_m*tau_mem)	Knudsen Diffusion Coefficient
C_2_v	((d_pore/2)^2)*eps_mem*(P_m_v)/(delta_m*tau_mem*8*mu_steam*R_const*T_f)	Variable Poiseuille Diffusion Coefficient

P_m_v	(Psatfinal+P_out)/2	Average Membrane Pressure
N_mem_v	C_perm_v*(Psatfinal-P_out)*M_w	Variable Membrane Permeate Flux
a_w_v	1-0.5*tcs2.x_salt-10*tcs2.x_salt^2	Variable Activity Coefficient
a_w_const	1-0.5*.1-10*.1^2	Constant Activity Coefficient
a_w	if(salt>=.265, a_w_const,a_w_v)	Conditional Activity Coefficient

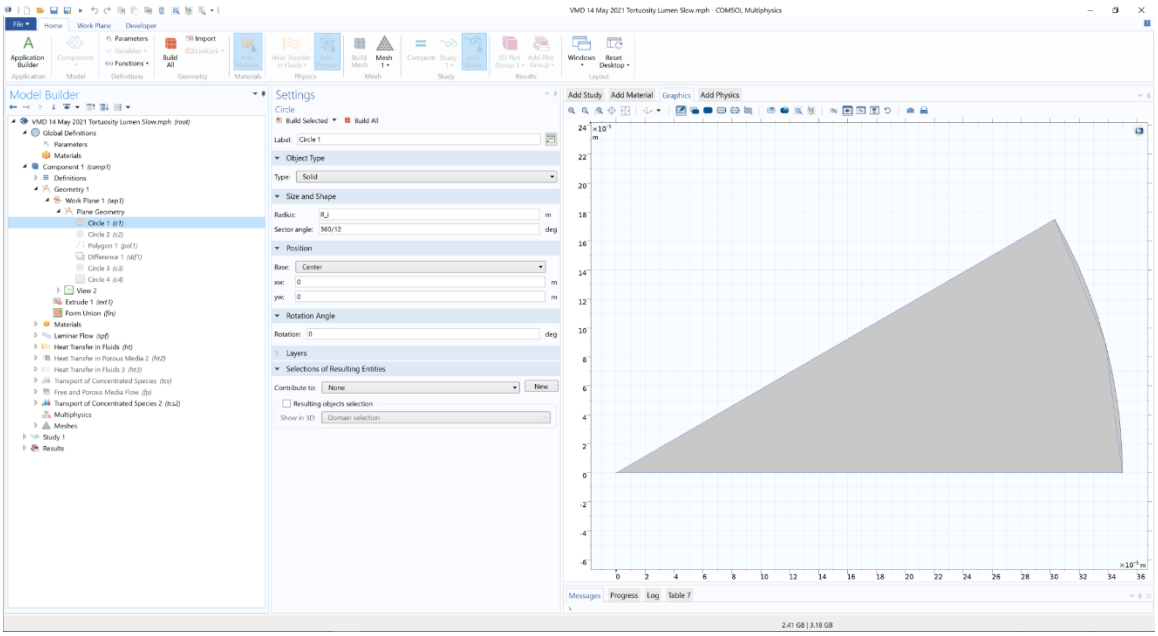

Figure A-1: Snapshot of the COMSOL® Model Showing Geometry

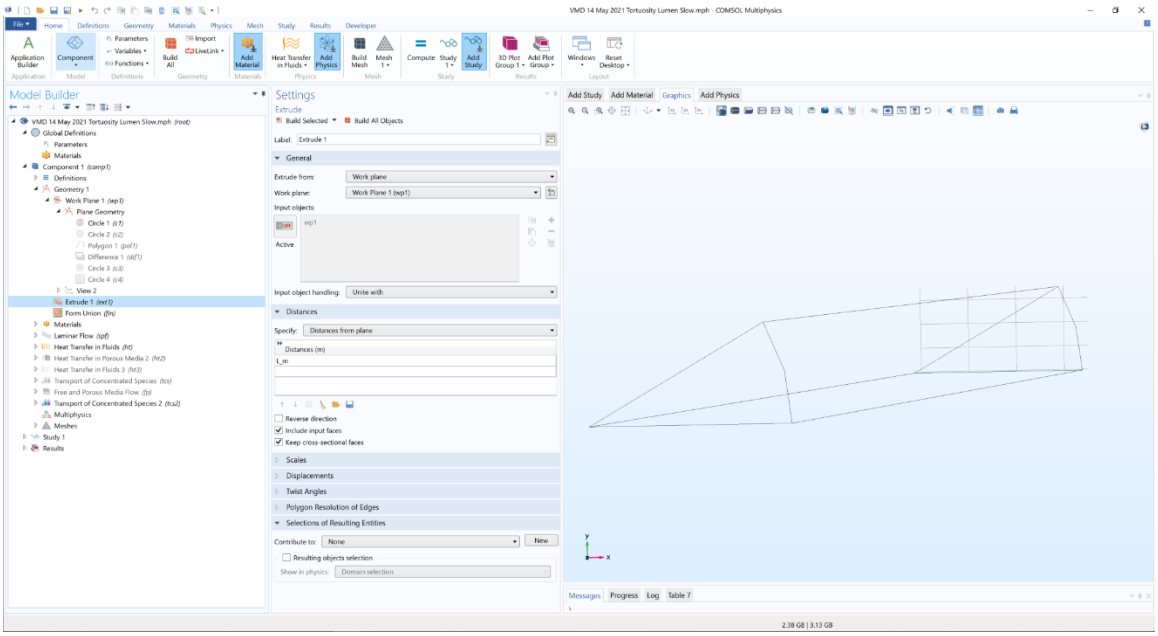

Figure A-2: Snapshot of the COMSOL® Model Showing Geometry

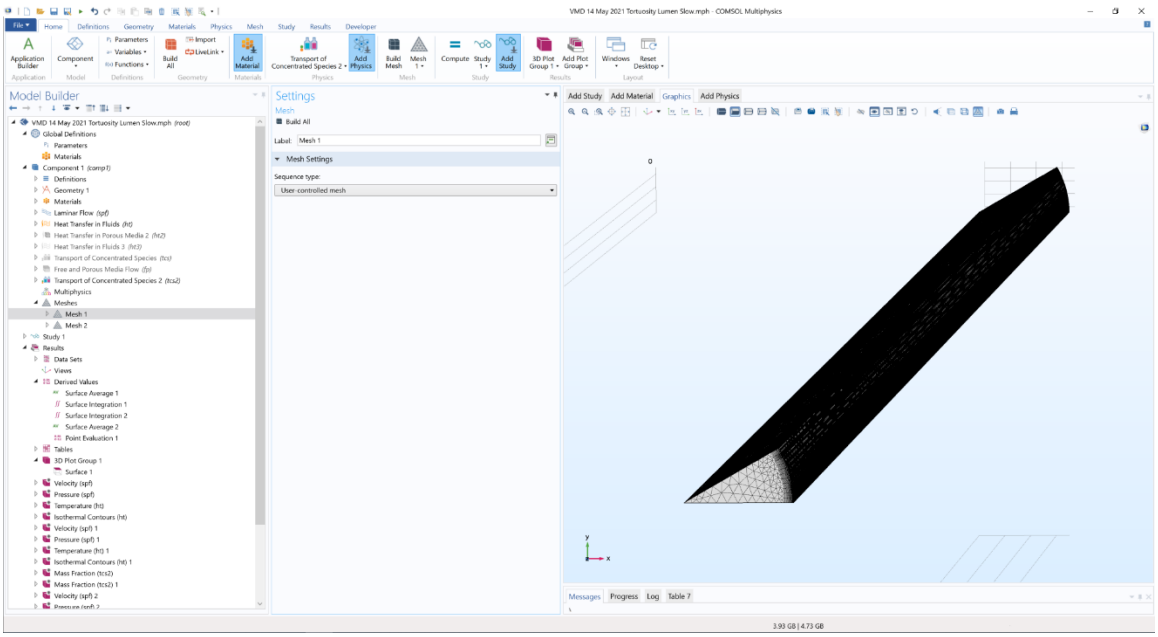

Figure A-3: Overall meshing scheme

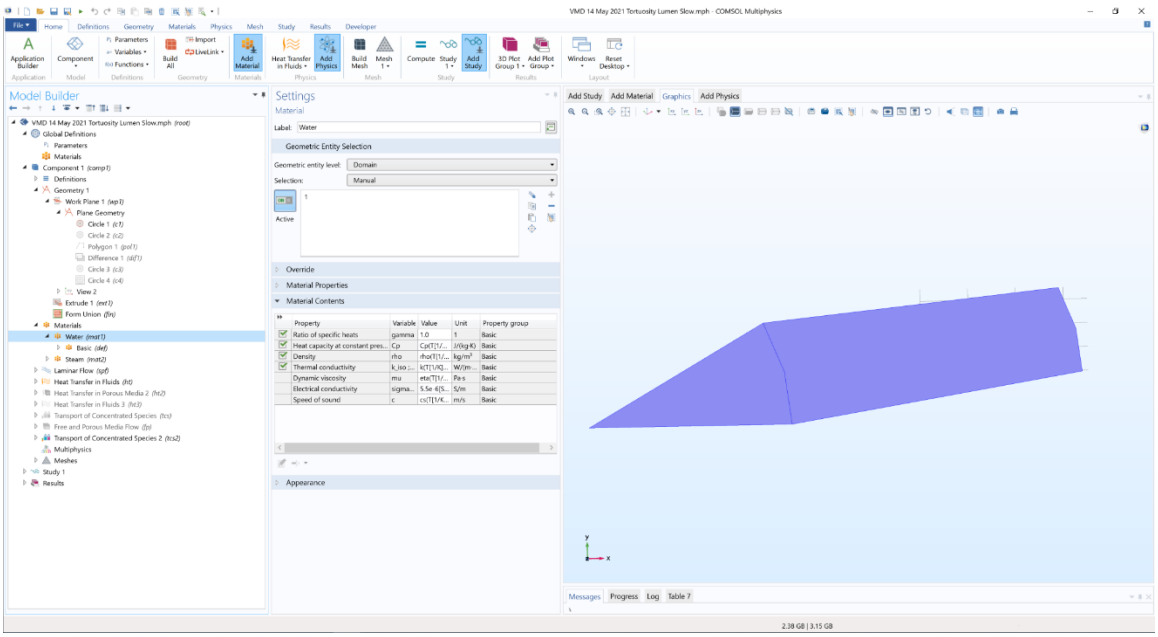

Figure A-4: Materials Definition

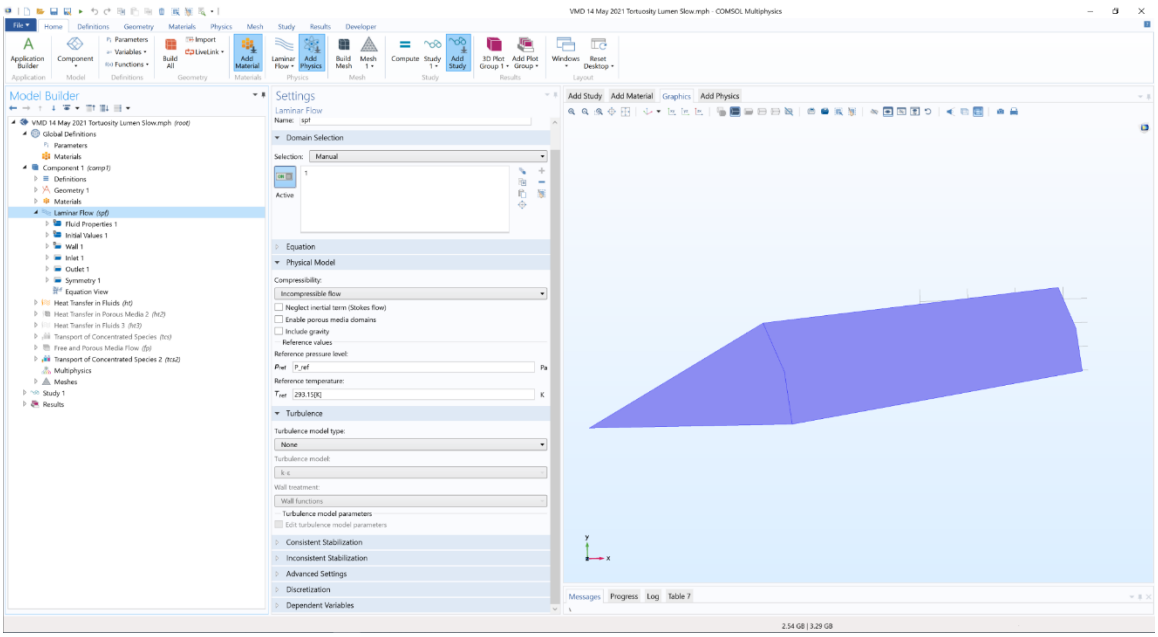

Figure A-5: Laminar Flow Domain

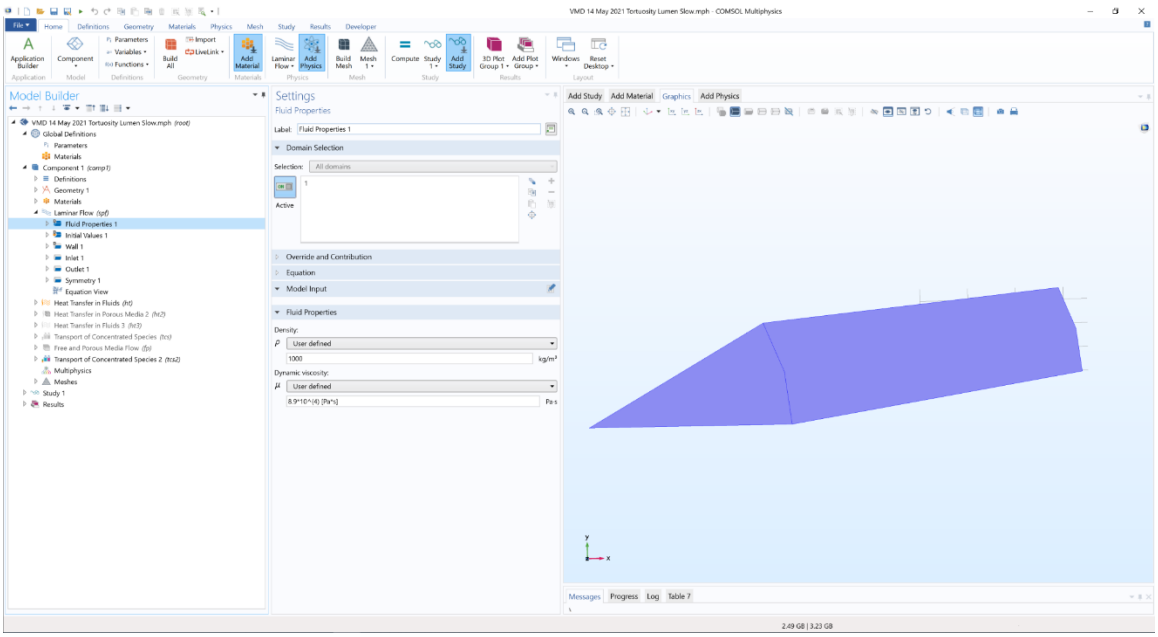

Figure A-6: Laminar Fluid Properties

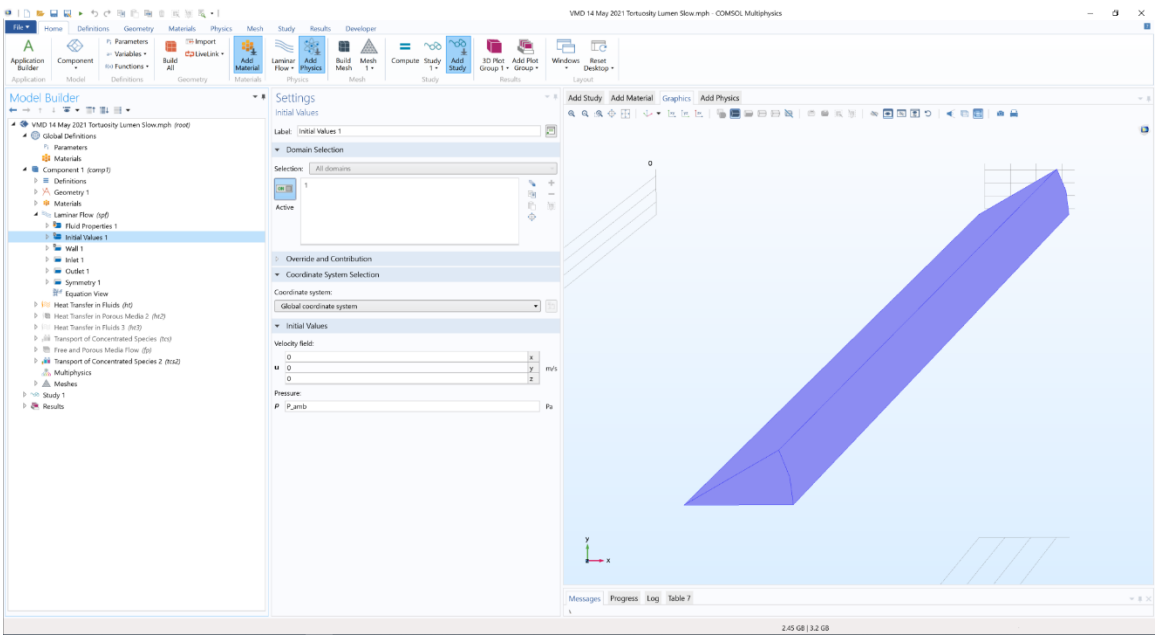

Figure A-7: Laminar Flow Initial Values

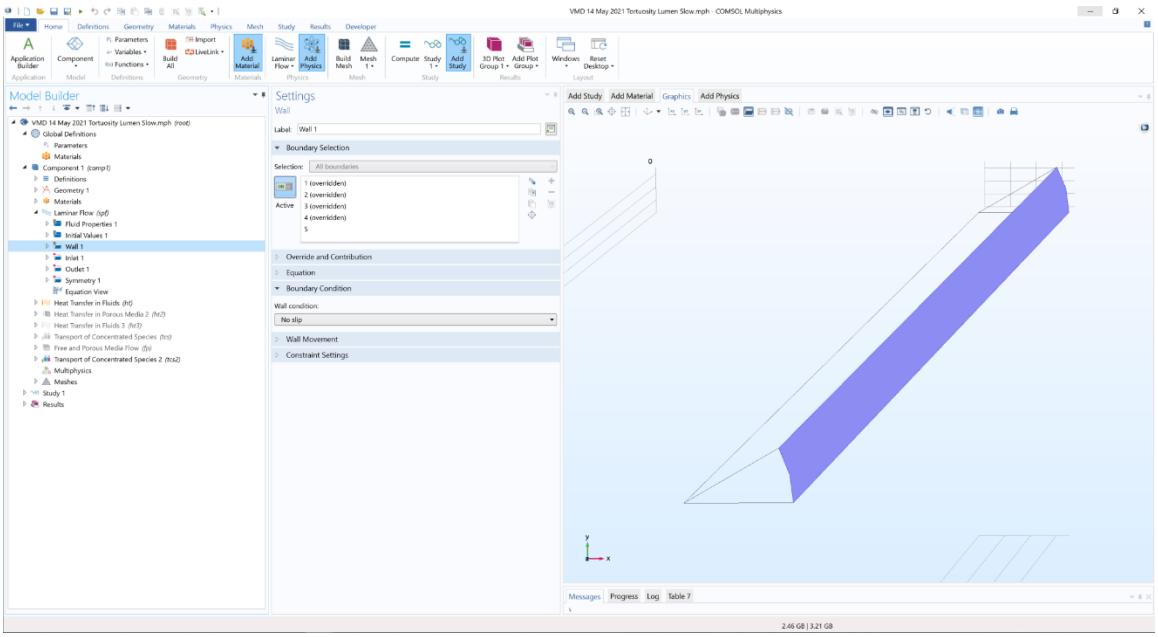

Figure A-8: Laminar Flow Wall

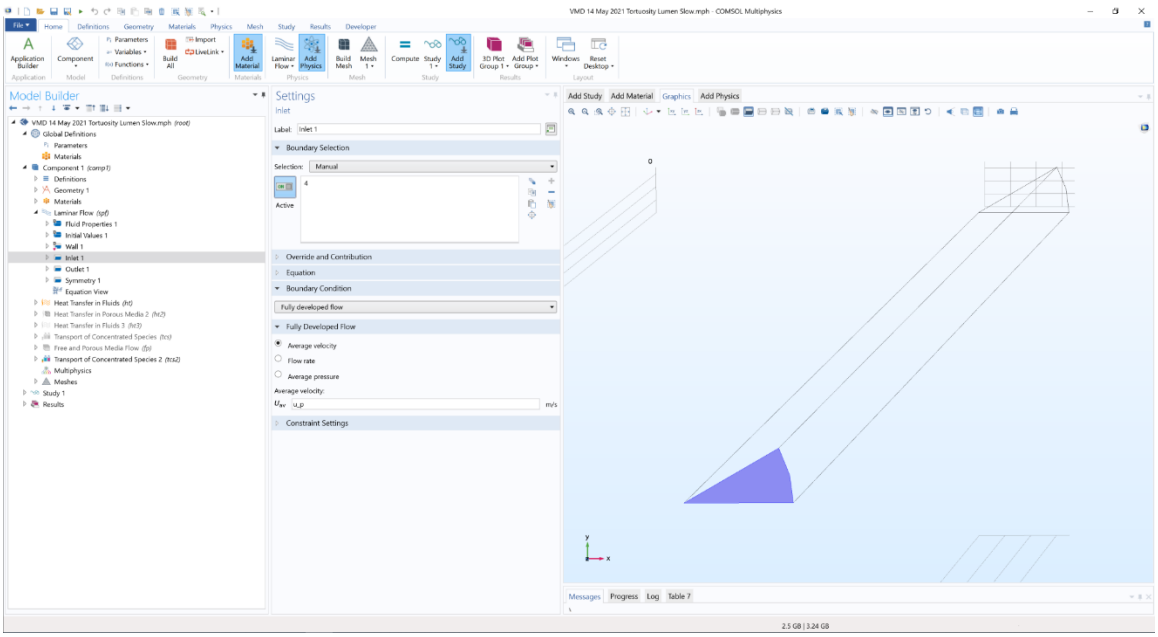

Figure A-9: Laminar Flow Inlet Velocity

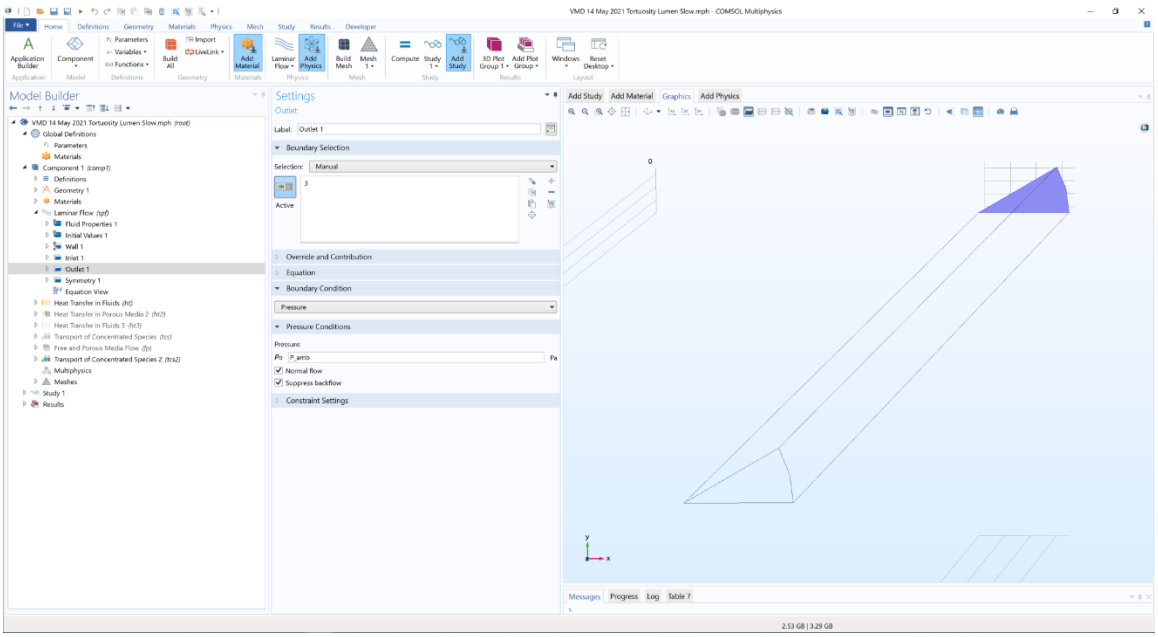

Figure A-10: Laminar Flow Outlet Pressure

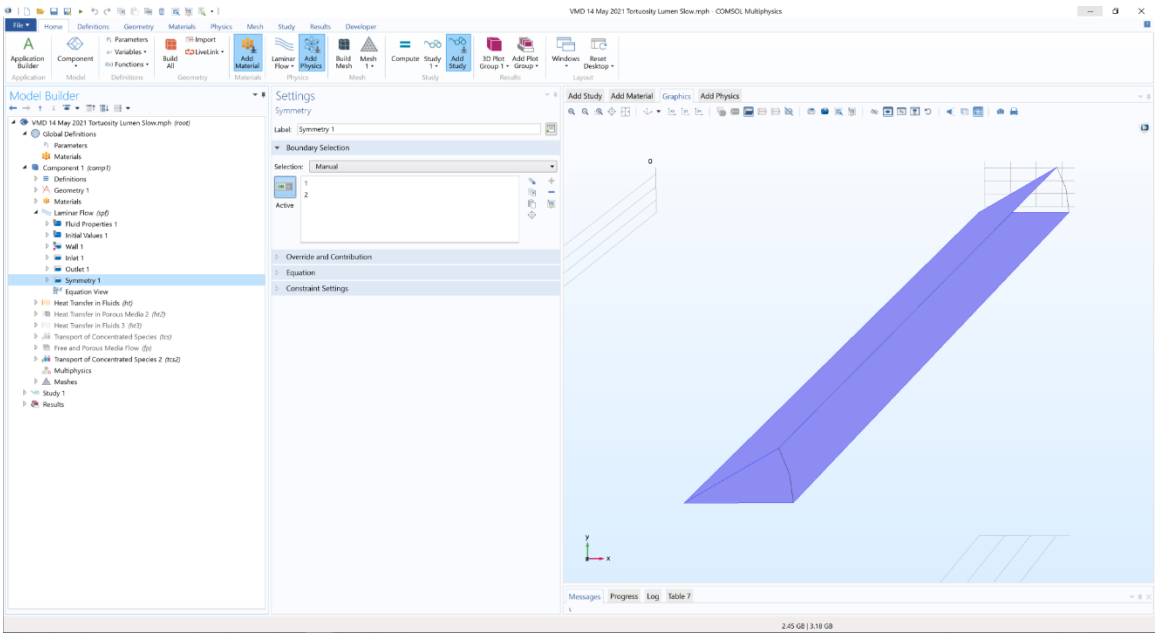

Figure A-11: Laminar Flow Planes of Symmetry

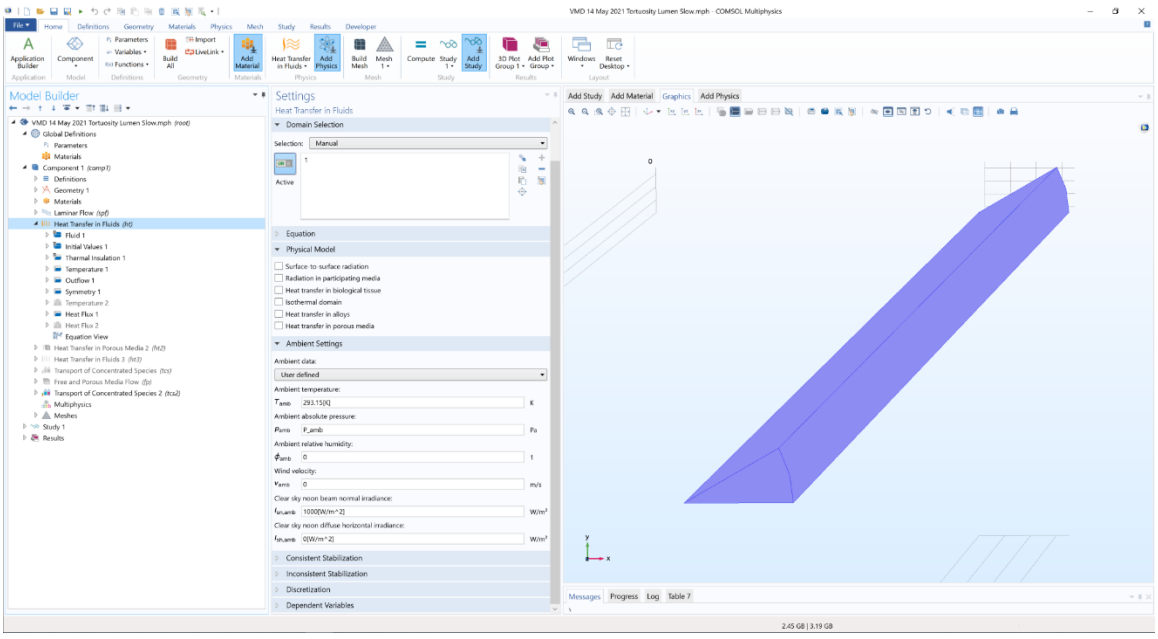

Figure A-12: Heat Transfer Domain

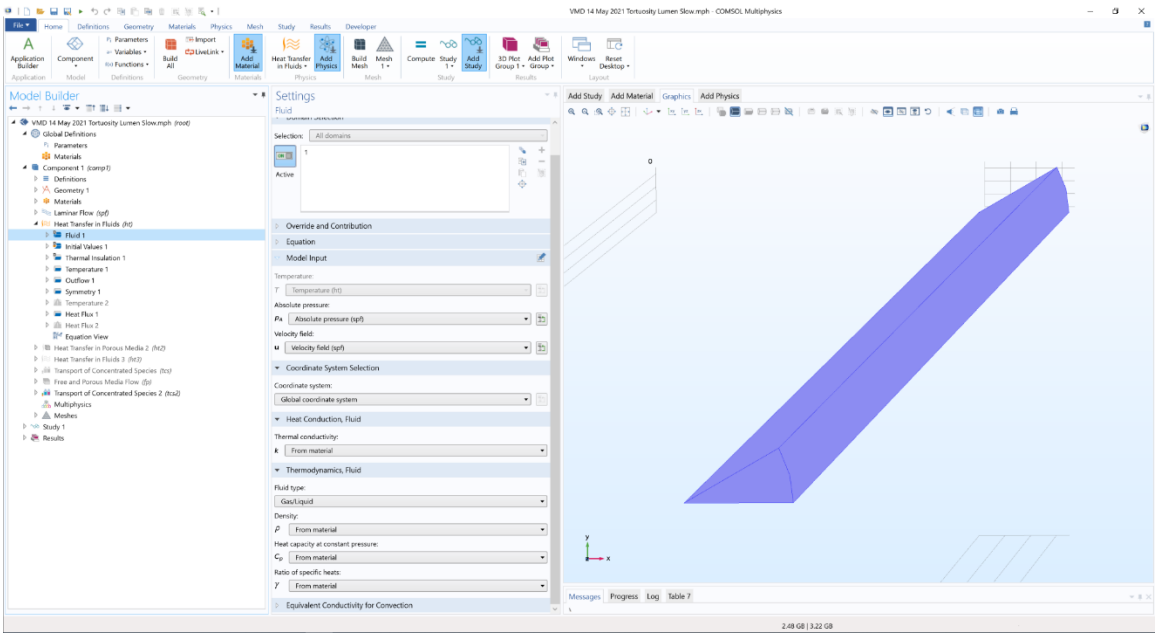

Figure A-13: Heat Transfer Fluid

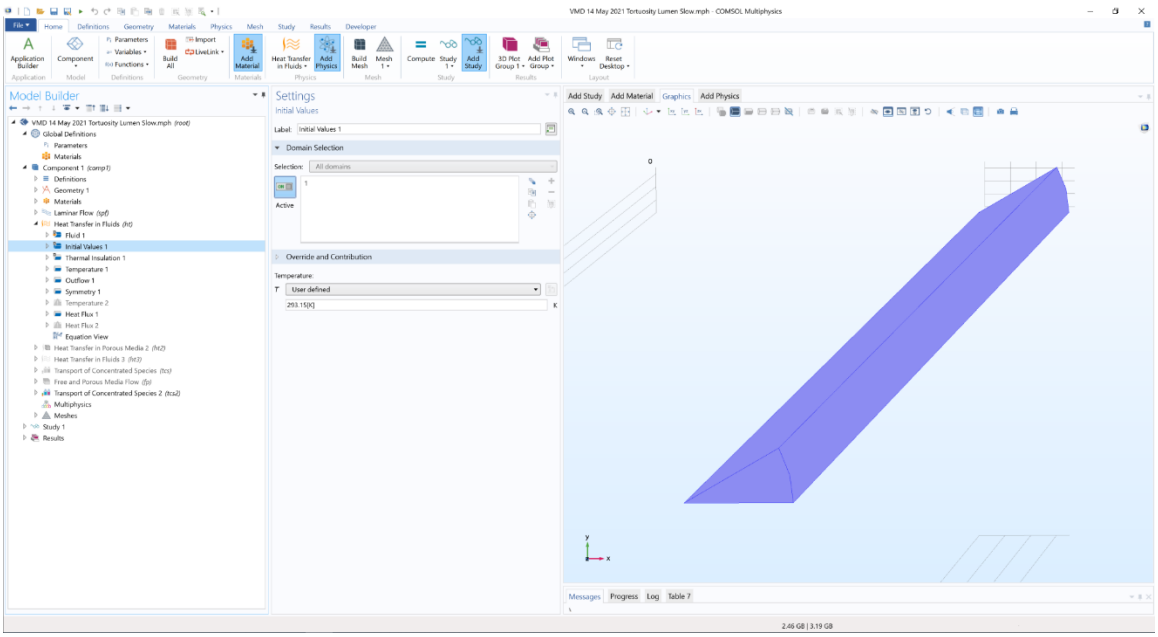

Figure A-14: Heat Transfer Initial Values

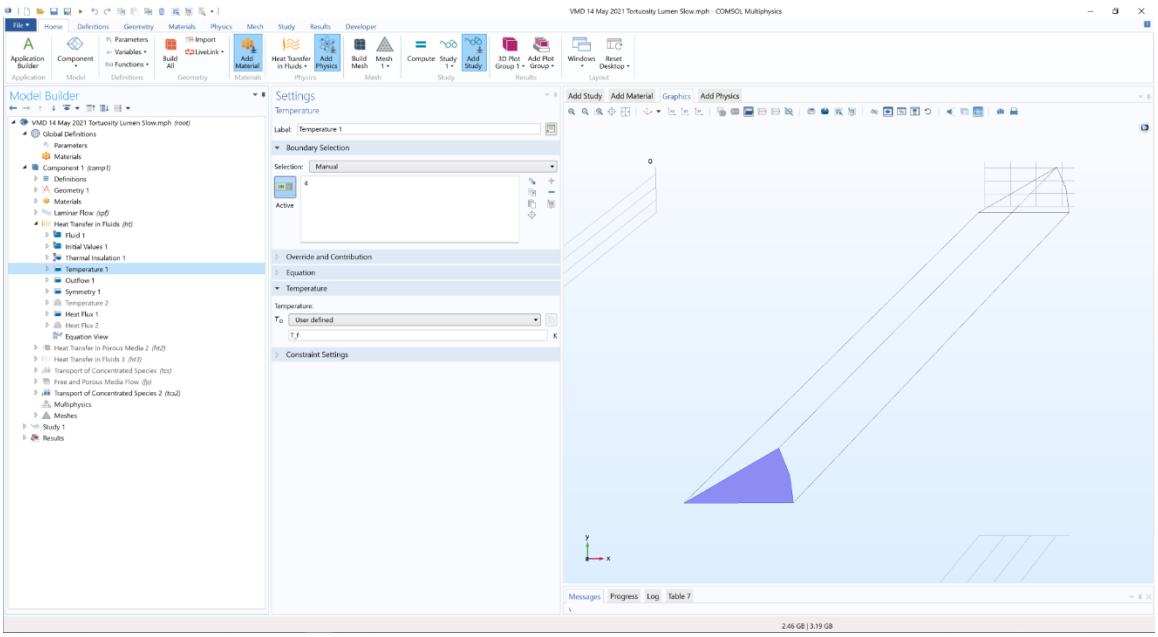

Figure A-15: Heat Transfer Inlet Temperature

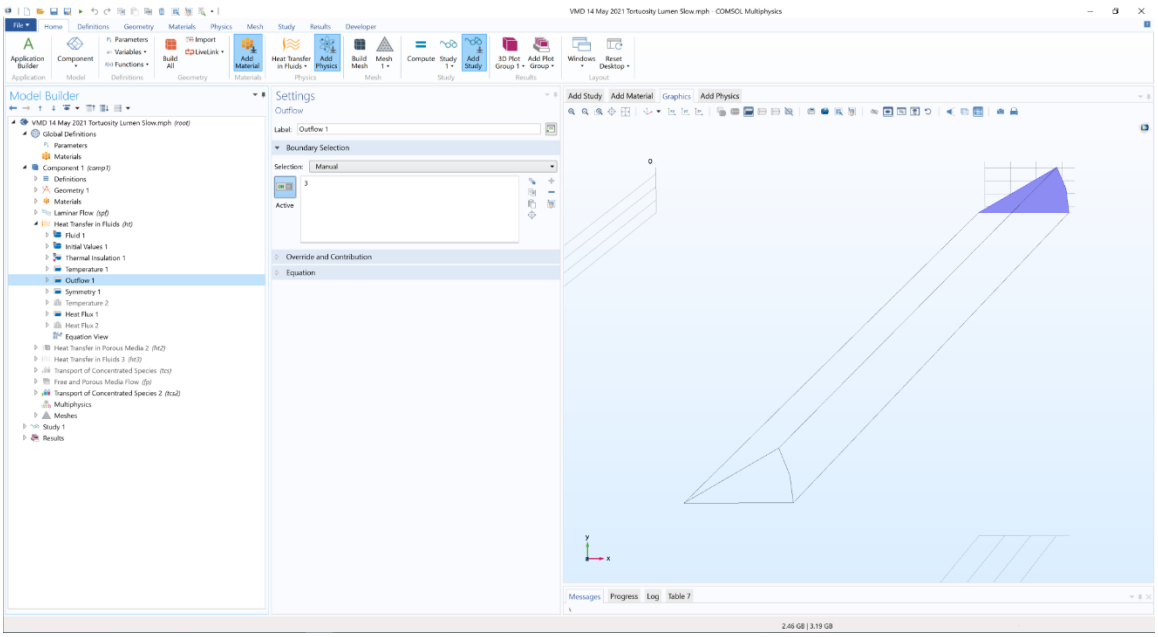

Figure A-16: Heat Transfer Outflow

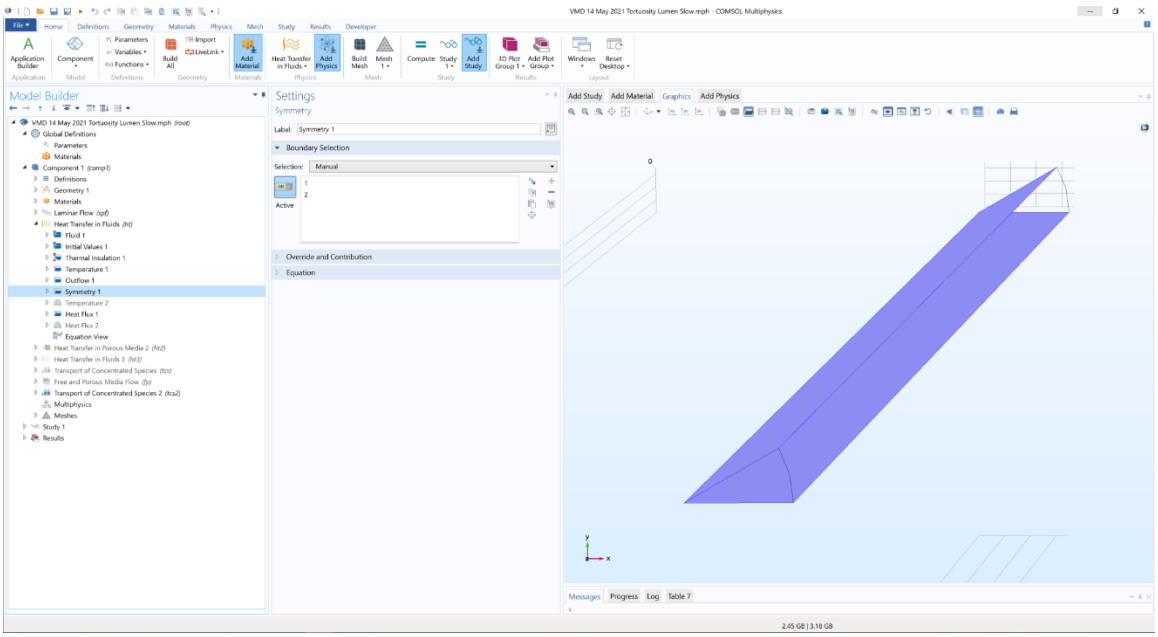

Figure A-17: Heat Transfer Planes of Symmetry

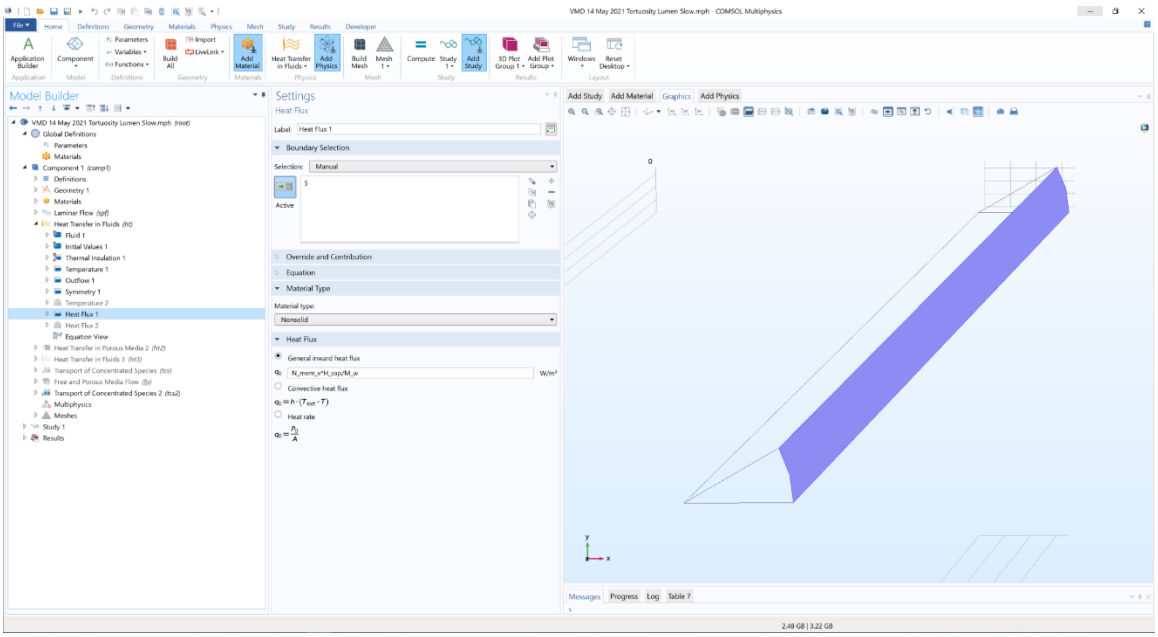

Figure A-18: Heat Transfer Heat Flux

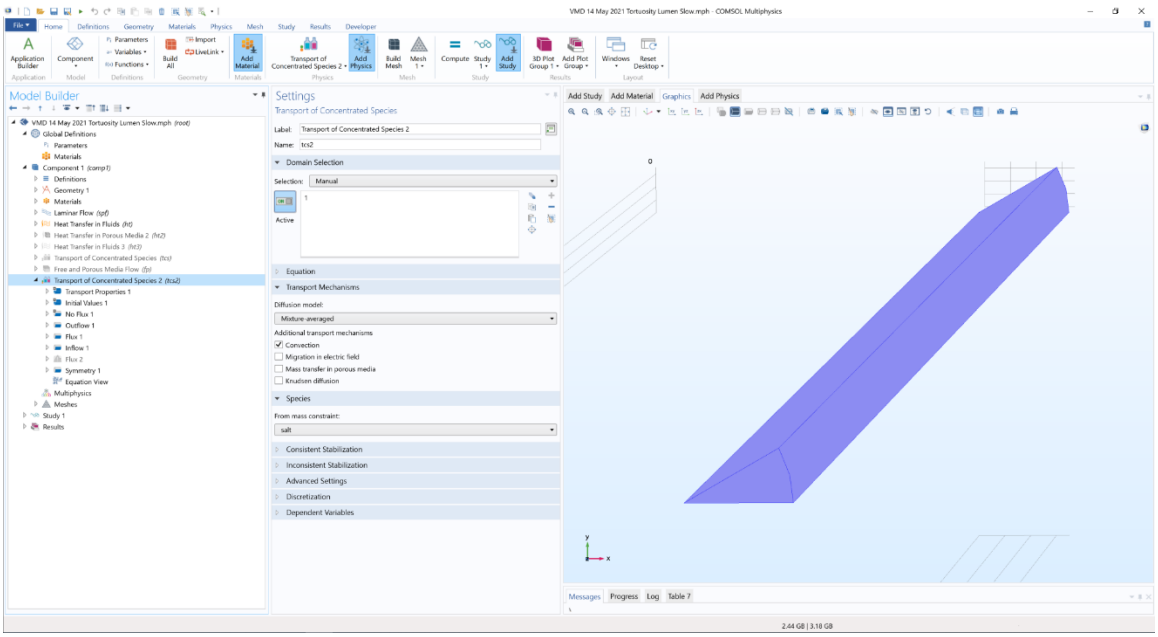

Figure A-19: Mass Transfer Domain

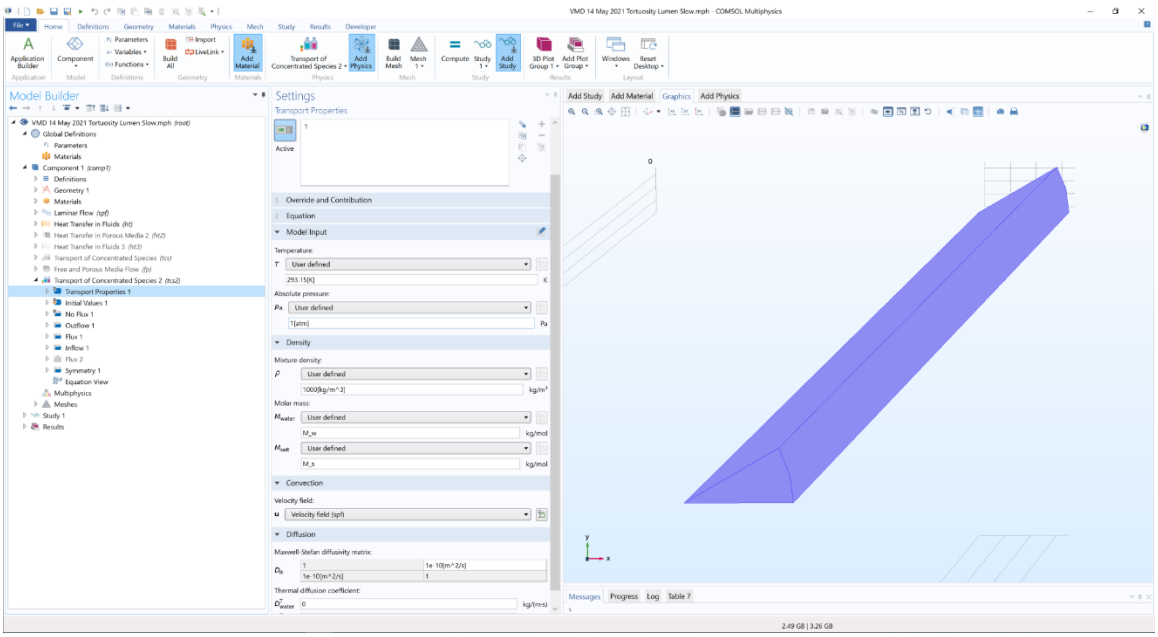

Figure A-20: Mass Transfer Transport Properties

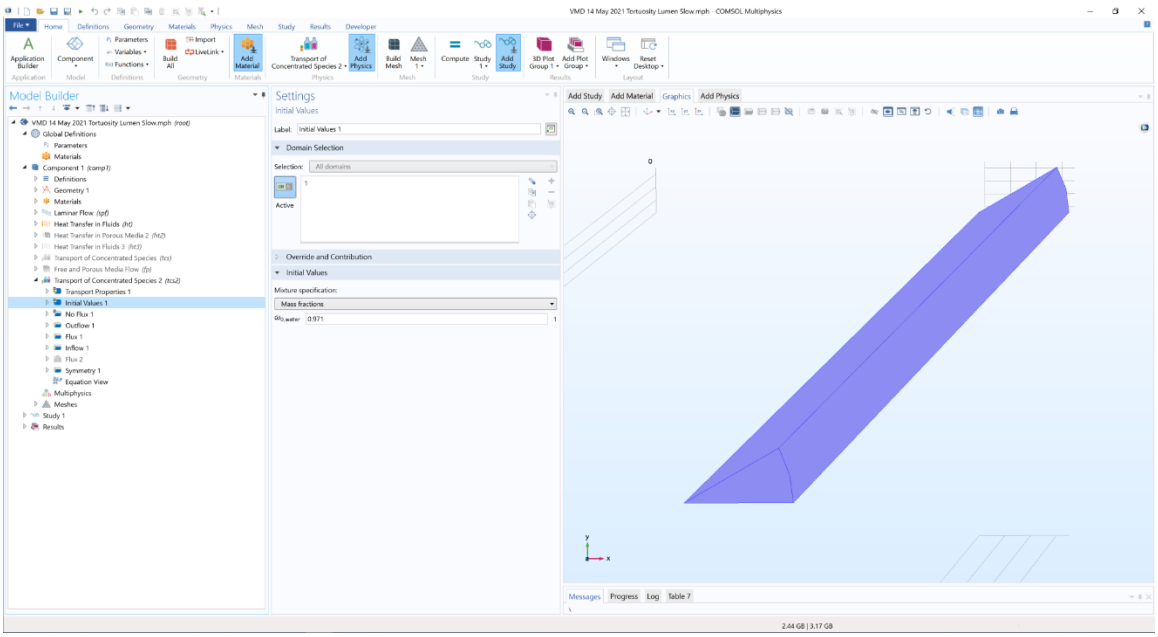

Figure A-21: Mass Transfer Initial Values

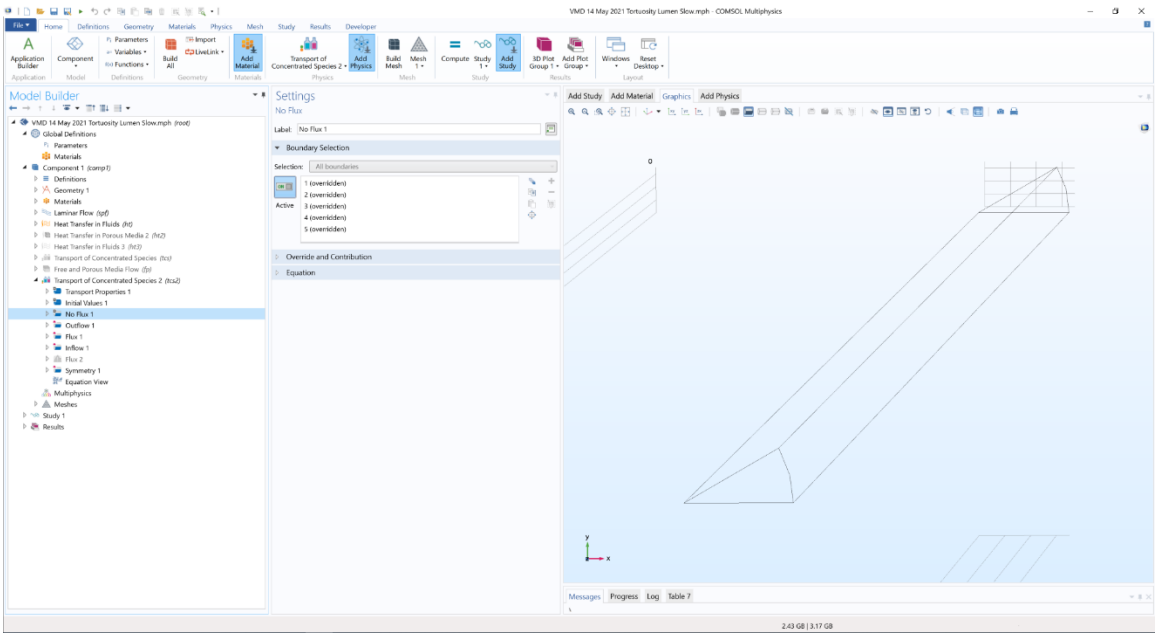

Figure A-22: Mass Transfer No Flux

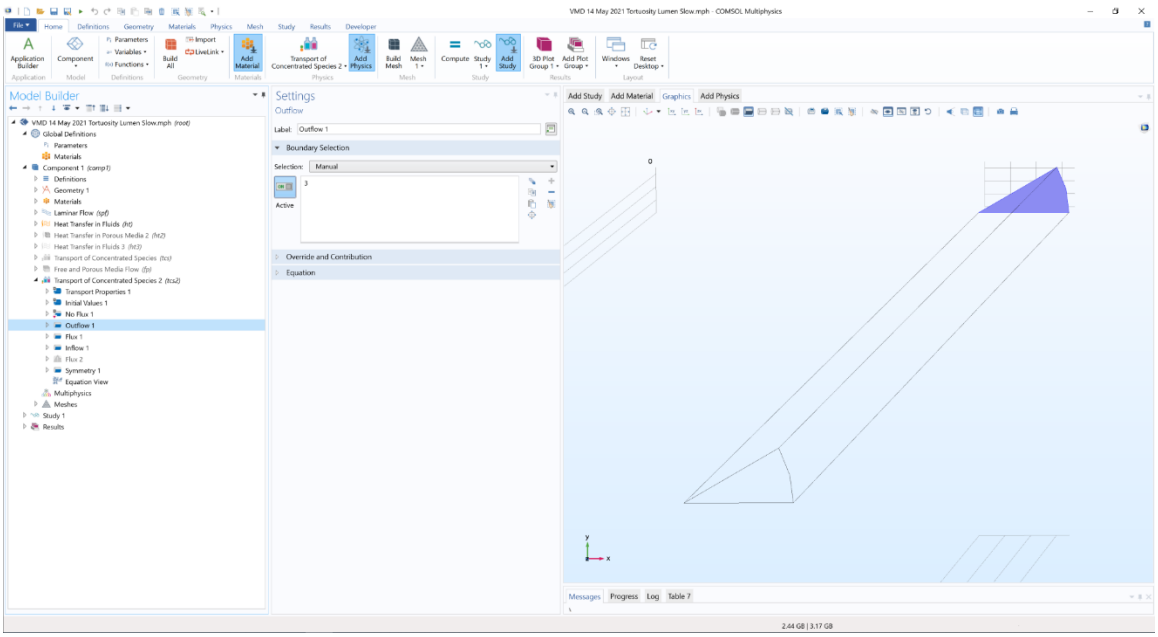

Figure A-23: Mass Transfer Outflow

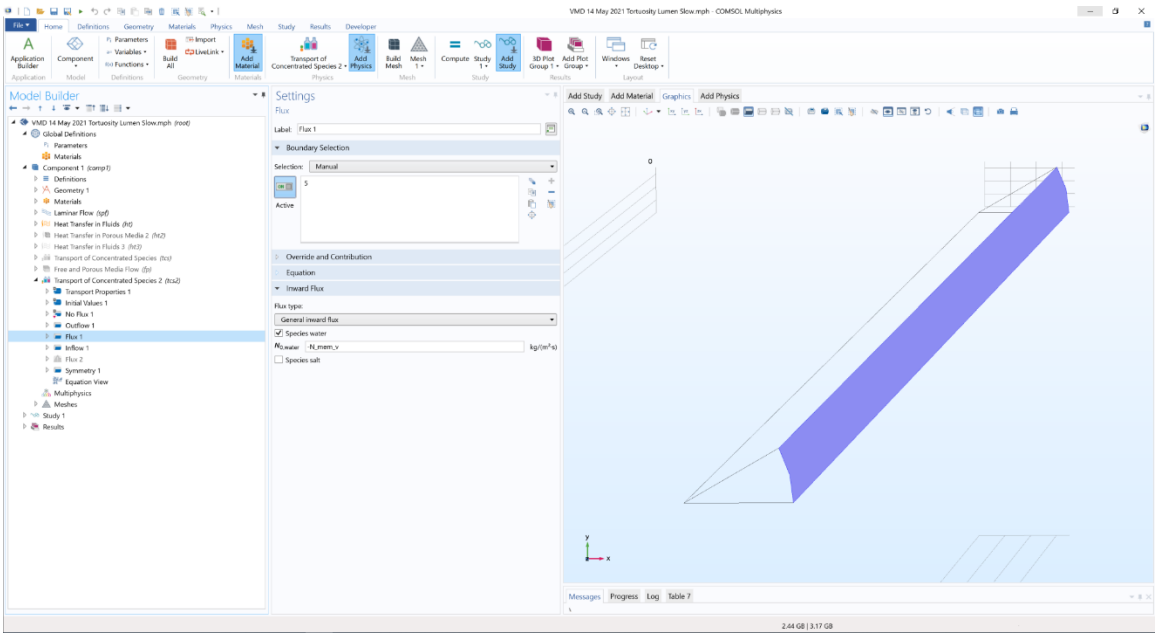

Figure A-24: Mass Transfer Flux

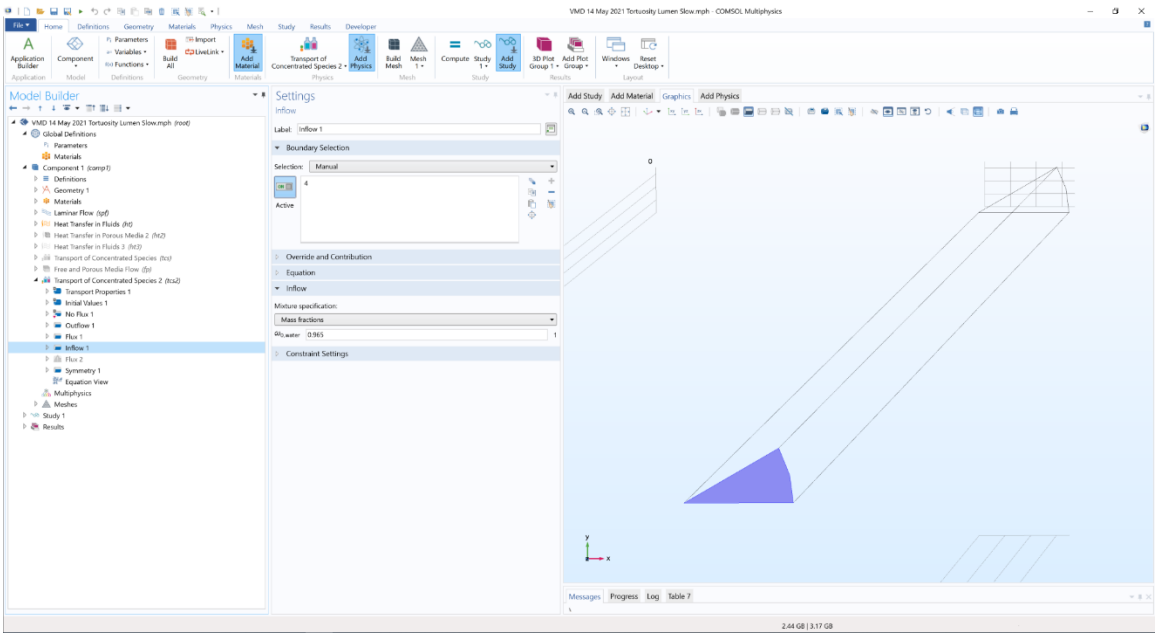

Figure A-25: Mass Transfer Inlet Concentration

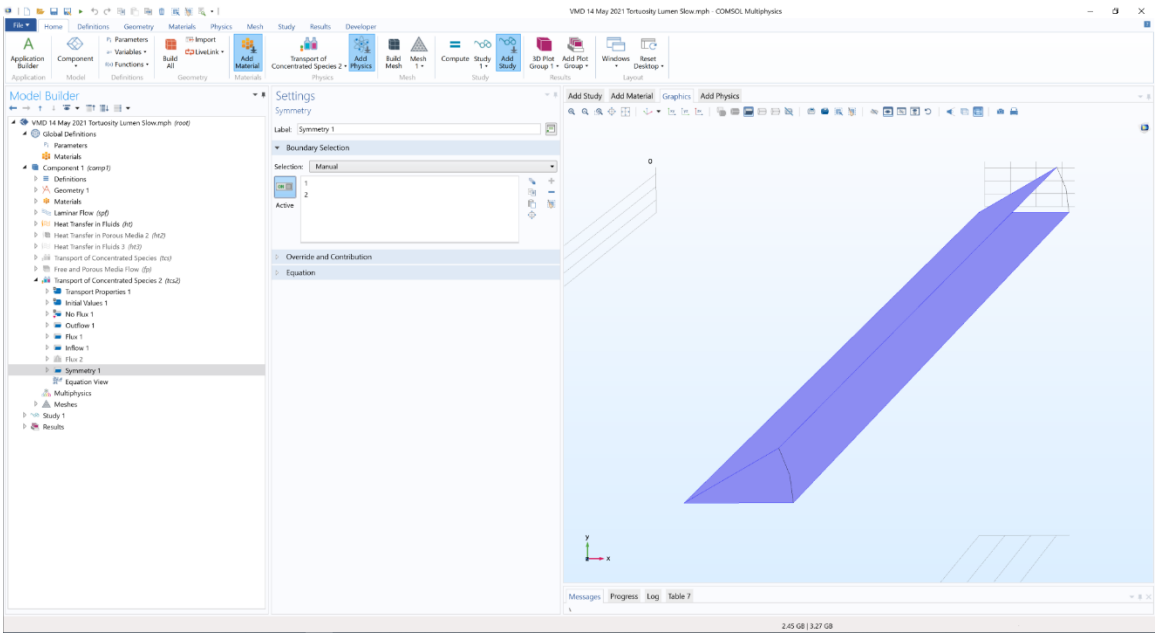

Figure A-26: Mass Transfer Planes of Symmetry

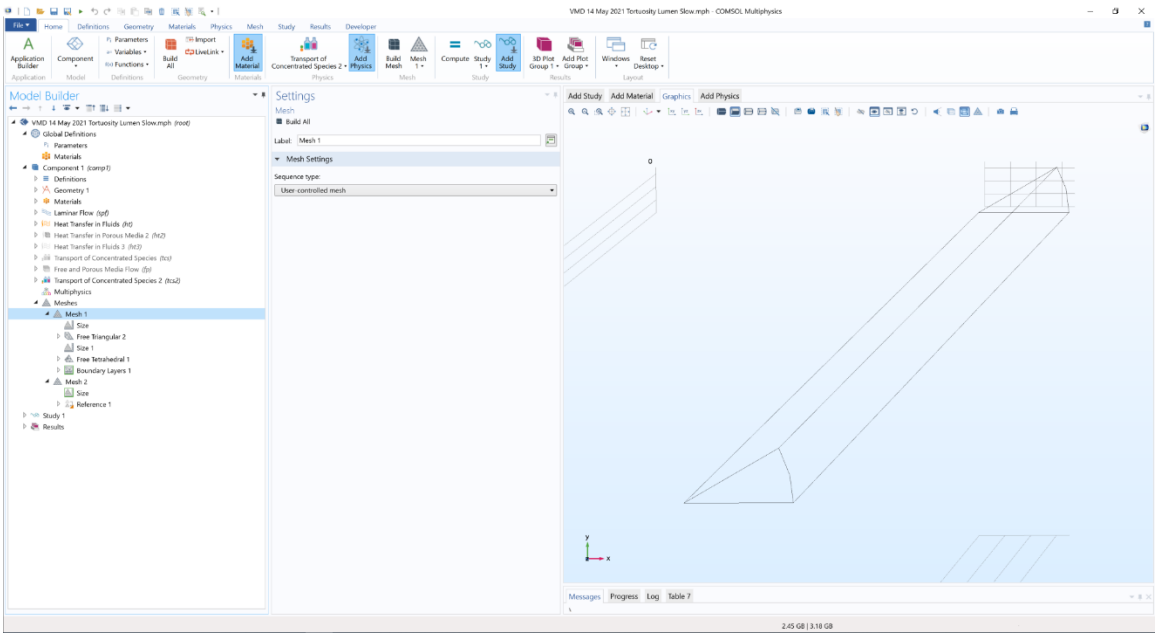

Figure A-27: Mesh Definition

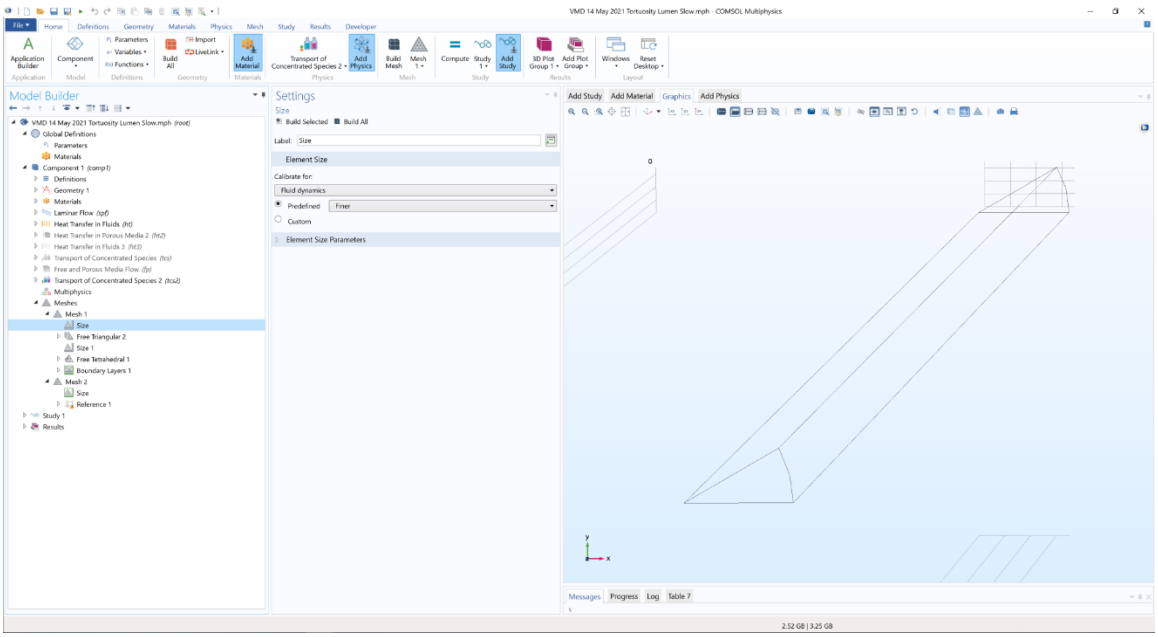

Figure A-28: Mesh Definition

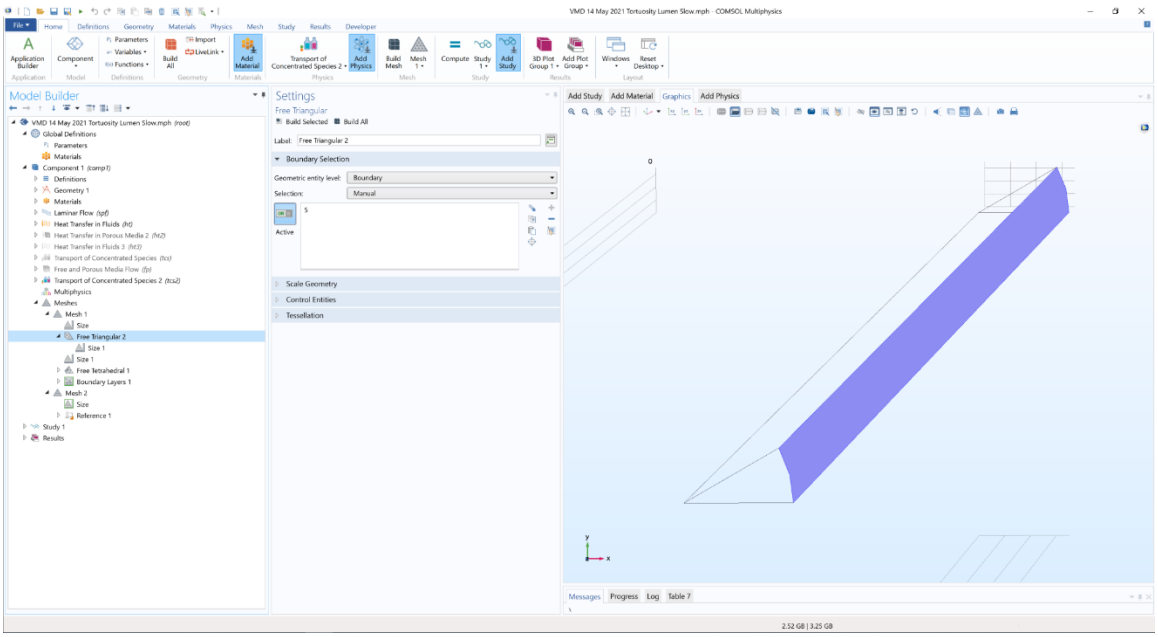

Figure A-29: Mesh Definition

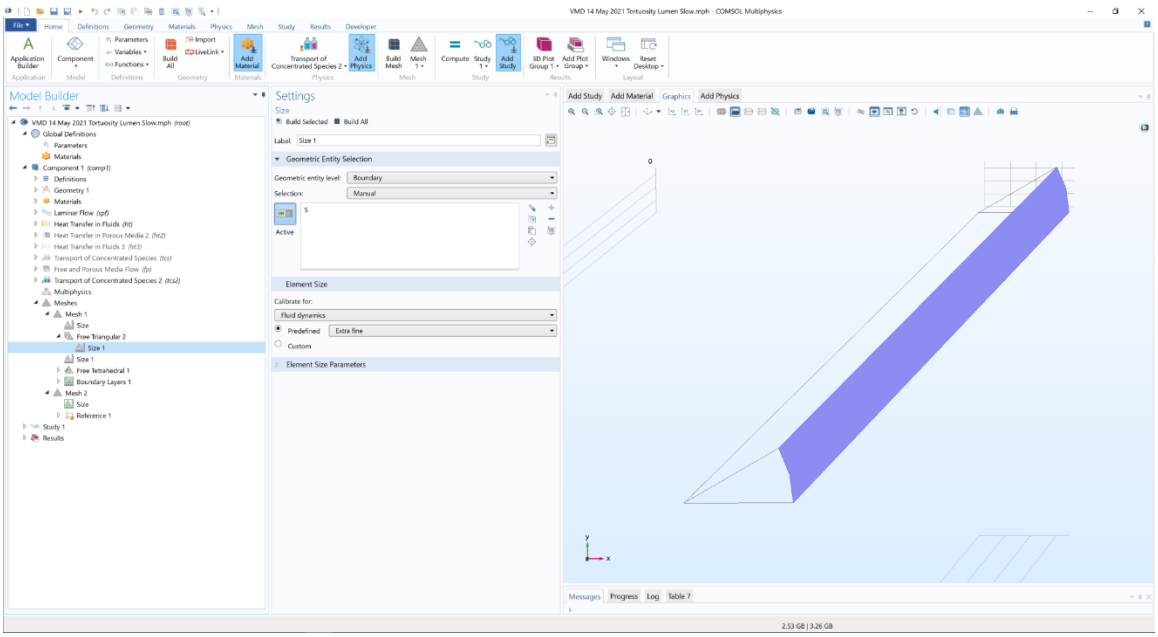

Figure A-30: Mesh Definition

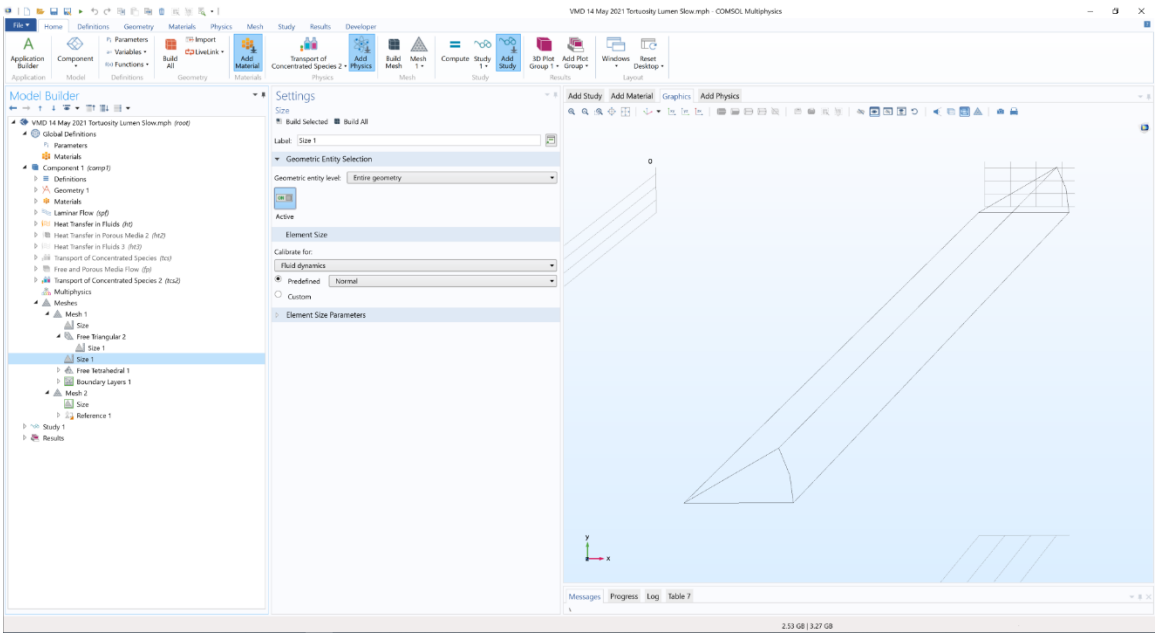

Figure A-31: Mesh Definition

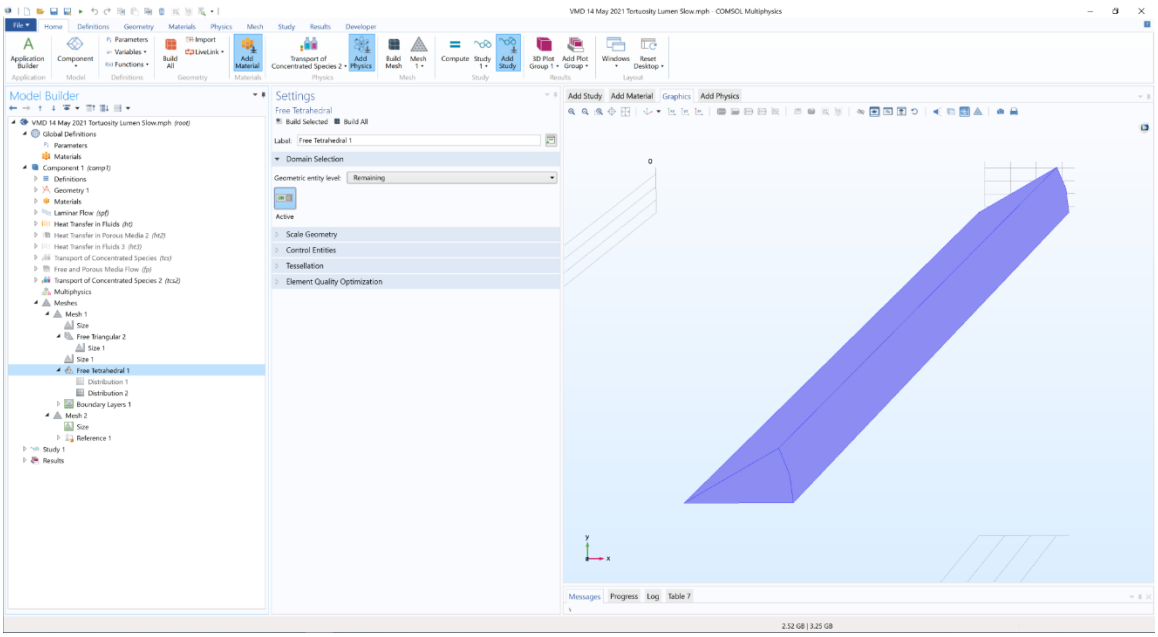

Figure A-32: Mesh Definition

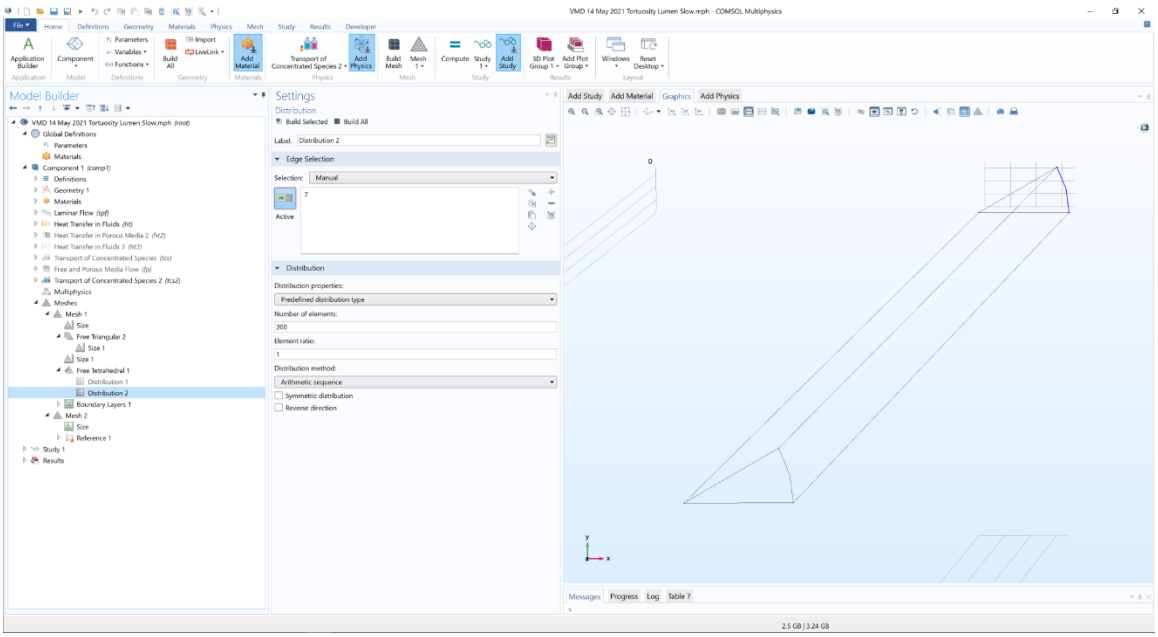

Figure A-33: Mesh Definition

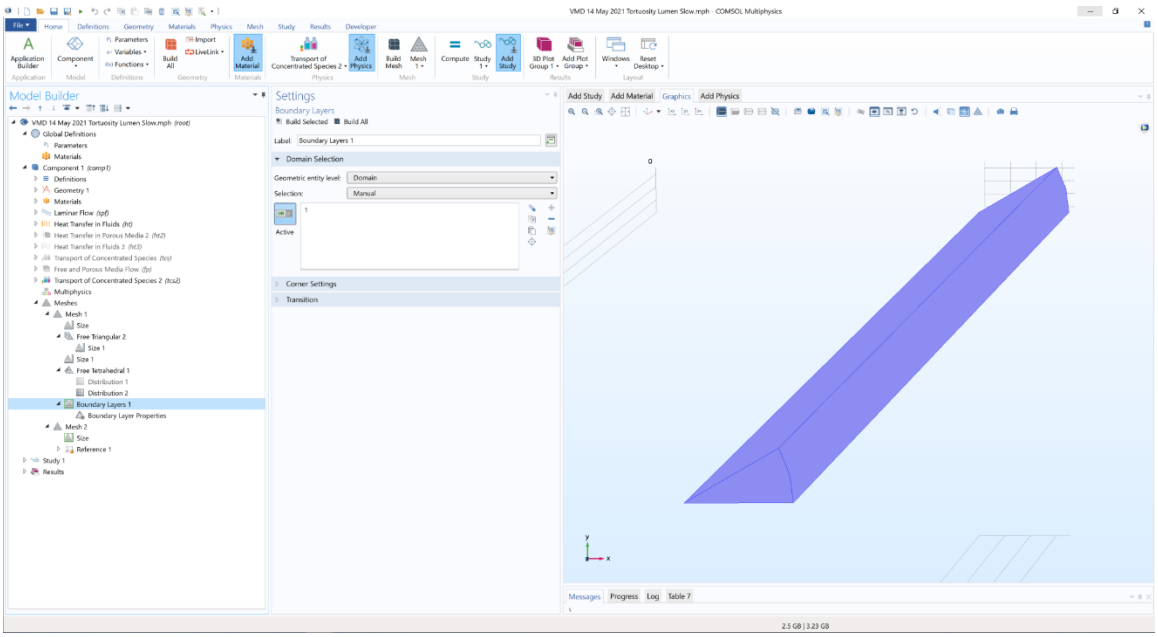

Figure A-34: Mesh Definition

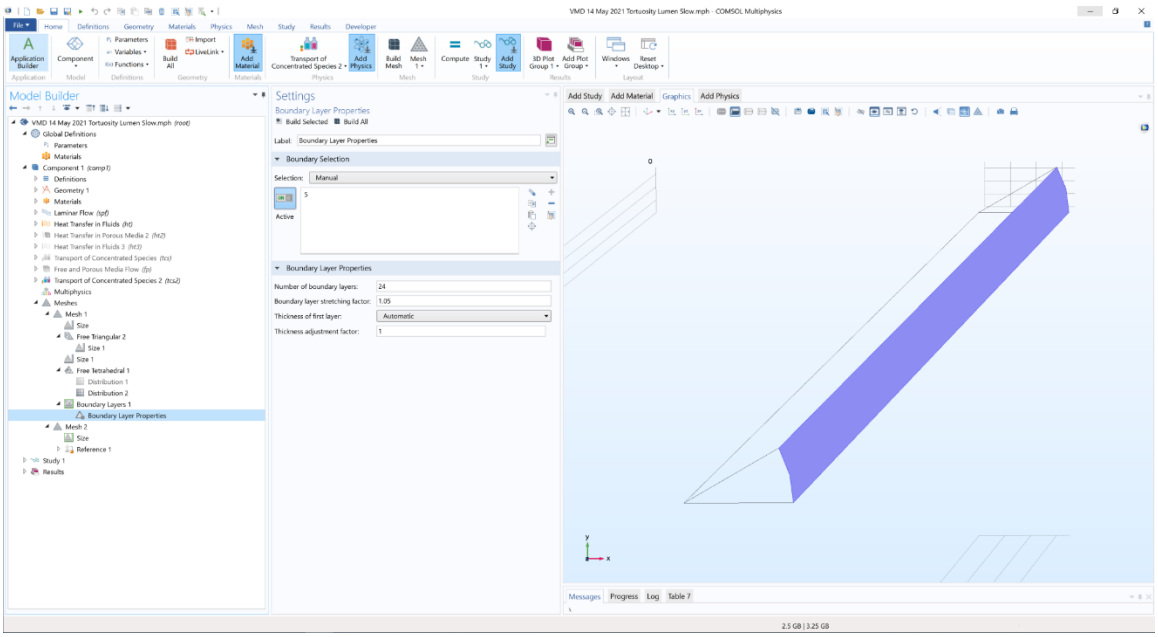

Figure A-35: Mesh Definition